# การสังเคราะห์ท่อนาโนคาร์บอนชนิดผนังหลายชั้นโดยการตกสะสมไอเชิงเคมีแบบฟลูอิไดซ์เบดบนโคบอลต์/อะลูมินา

นายสมโภช ภู่พีระสุพงษ์

วิทยานิพนธ์นี้เป็นส่วนหนึ่งของการศึกษาตามหลักสูตรปริญญาวิทยาศาสตรดุษฎีบัณฑิต
สาขาวิชาเคมีเทคนิค ภาควิชาเคมีเทคนิค
คณะวิทยาศาสตร์ จุฬาลงกรณ์มหาวิทยาลัย
ปีการศึกษา 2554

# SYNTHESIS OF MULTI-WALLED CARBON NANOTUBES BY FLUIDIZED-BED CHEMICAL VAPOR DEPOSITION OVER $Co/Al_2O_3$

Mr. SOMPOCH POOPERASUPONG

A Dissertation Submitted in Partial Fulfillment of the Requirements
for the Degree of Doctor of Philosophy Program in Chemical Technology
Department of Chemical Technology
Faculty of Science
Chulalongkorn University
Academic Year 2011

| | |
|---|---|
| Thesis Title | SYNTHESIS OF MULTI-WALLED CARBON NANOTUBES BY FLUIDIZED-BED CHEMICAL VAPOR DEPOSITION OVER $Co/Al_2O_3$ |
| By | Mr. Sompoch Pooperasupong |
| Field of Study | Chemical Technology |
| Thesis Advisor | Professor Somsak Damronglerd, Dr. Ing. |
| Thesis Co-advisor | Professor Brigitte Caussat-Bonnans, Dr. de L'INPT. |

Accepted by the Faculty of Science, Chulalongkorn University in Partial Fulfillment of the Requirements for the Doctoral Degree

……. Dean of the Faculty of Science
(Professor Supot Hannongbua, Dr. rer. nat.)

THESIS COMMITTEE

……..Chairman
(Kunakorn Poochinda, Ph.D.)

……..Thesis Advisor
(Professor Somsak Damronglerd, Dr. Ing.)

……..Thesis Co-advisor
(Professor Brigitte Caussat-Bonnans, Dr. de L'INPT.)

……..Examiner
(Associate Professor Nuttaya Pongstabodee, Ph.D.)

……..Examiner
(Associate Professor Tawatchai Charinpanitkul, D.Eng.)

……..External Examiner
(Sumate Charoenchaidet, Ph.D.)

สมโภช ภู่พีระสุพงษ์ : การสังเคราะห์ท่อนาโนคาร์บอนชนิดผนังหลายชั้นโดยการตกสะสมไอเชิงเคมีแบบฟลูอิไดซ์เบดบนโคบอลต์/อะลูมินา. (SYNTHESIS OF MULTI-WALLED CARBON NANOTUBES BY FLUIDIZED-BED CHEMICAL VAPOR DEPOSITION OVER $Co/Al_2O_3$) อ. ที่ปรึกษาวิทยานิพนธ์หลัก: ศ. ดร. สมศักดิ์ ดำรงค์เลิศ, Dr. Ing., อ. ที่ปรึกษาวิทยานิพนธ์ร่วม: Prof. Brigitte Caussat-Bonnans, Dr. de L'INPT., 138 หน้า.

ท่อนาโนคาร์บอนชนิดผนังหลายชั้นถูกสังเคราะห์โดยการตกสะสมไอเชิงเคมีเชิงเร่งของเอทิลีนบนโคบอลต์บนตัวรองรับอะลูมินาในฟลูอิไดซ์เบด ผลของอุณหภูมิและสัดส่วนโมลเอทิลีนในการก่อโครงร่างและคุณภาพของท่อนาโนคาร์บอนได้ถูกศึกษา ผลการวิเคราะห์เชิงปริมาณบ่งชี้ว่าอุณหภูมิในการทำปฏิกิริยามีความสำคัญมากต่อร้อยละการเปลี่ยนของคาร์บอนของแข็งและการเลือกเกิดของท่อนาโนคาร์บอนชนิดผนังหลายชั้น โดยคาร์บอนอสัณฐานและเส้นใยนาโนคาร์บอนเกิดเป็นผลิตภัณฑ์หลัก ณ อุณหภูมิในการทำปฏิกิริยา 550 องศาเซลเซียส

สัดส่วนโมลเอทิลีนมีอิทธิพลต่อการผลิตท่อนาโนคาร์บอนชนิดผนังหลายชั้นเช่นกัน ณ ภาวะสัดส่วนโมลเอทิลีน 0.63 พบการปรากฏของคาร์บอนอสัณฐานเป็นผลิตภัณฑ์หลักและเป็นเหตุให้เกิดการสูญเสียความว่องไวของตัวเร่งปฏิกิริยา ผลิตภาพของท่อนาโนคาร์บอนชนิดผนังหลายชั้นมีค่าสูงสุดเท่ากับ 0.45 กรัมต่อกรัมของตัวเร่งปฏิกิริยา ณ อุณหภูมิในการทำปฏิกิริยา 600 องศาเซลเซียส สัดส่วนโมลเอทิลีน 0.5 น้ำหนักตัวเร่งปฏิกิริยา 20 กรัม และเวลาในการทำปฏิกิริยา 60 นาที

ผลการวิเคราะห์เชิงคุณภาพแสดงให้เห็นว่า การเพิ่มอุณหภูมิในการทำปฏิกิริยาทำให้เกิดท่อนาโนคาร์บอนที่มีโครงสร้างสมบูรณ์ยิ่งขึ้น เส้นผ่าศูนย์กลางของท่อนาโนคาร์บอนชนิดผนังหลายชั้นที่สังเคราะห์ได้มีค่าประมาณ 7 นาโนเมตรสำหรับทุกภาวะการทดลอง

ผลการวิเคราะห์แก๊สขาออกบ่งชี้ว่า อีเทนสามารถสลายตัวเป็นท่อนาโนคาร์บอนชนิดผนังหลายชั้น ณ อุณหภูมิในการทำปฏิกิริยา 650 องศาเซลเซียสขึ้นไป ในขณะที่มีเทนไม่ทำปฏิกิริยาในช่วงอุณหภูมิที่ศึกษา พารามิเตอร์จลนศาสตร์ ได้แก่ สัมประสิทธิ์เอ็กซ์โพเนนเชียลและพลังงานก่อกัมมันต์มีค่าเท่ากับ 3.21 กรัมต่อกรัมตัวเร่งปฏิกิริยาต่อนาที และ 65.3 กิโลจูลต่อโมล ตามลำดับ ทั้งนี้พลังงานก่อกัมมันต์ในการก่อโครงร่างของท่อนาโนคาร์บอนชนิดผนังหลายชั้นมีค่าใกล้เคียงกับพลังงานก่อกัมมันต์ของการแพร่ของคาร์บอนในโคบอลต์เหลว

ภาควิชา เคมีเทคนิค ลายมือชื่อนิสิต .....

สาขาวิชา เคมีเทคนิค ลายมือชื่อ อ.ที่ปรึกษาวิทยานิพนธ์หลัก .....

ปีการศึกษา 2554 ลายมือชื่อ อ.ที่ปรึกษาวิทยานิพนธ์ร่วม .....

# # 4773841223 : MAJOR CHEMICAL TECHNOLOGY
KEYWORDS : MULTI-WALLED CARBON NANOTUBES / CHEMICAL VAPOR DEPOSITION / FLUIDIZED-BED / COBALT CATALYST

SOMPOCH POOPERASUPONG : SYNTHESIS OF MULTI-WALLED CARBON NANOTUBES BY FLUIDIZED-BED CHEMICAL VAPOR DEPOSITION OVER $Co/Al_2O_3$. ADVISOR : PROF. SOMSAK DAMRONGLERD, Dr. Ing., CO-ADVISOR : PROF. BRIGITTE CAUSSAT-BONNANS, Dr. de L'INPT., 138 pp.

Multi-walled carbon nanotubes (MWNTs) were successfully synthesized by catalytic chemical vapor deposition of ethylene over cobalt supported alumina in fluidized-bed. The effects of temperature and ethylene molar fraction on MWNTs formation and MWNTs quality were studied. Quantitative analysis results indicated that reaction temperature is crucial for solid carbon conversion and MWNTs selectivity. Amorphous carbon and carbon nanofibers (CNFs) were obtained as main products at reaction temperature of 550 $^{o}$C.

Ethylene molar fraction also affected MWNTs production. Ethylene molar fraction of 0.63 led to the presence of amorphous carbon as a main product and caused the catalyst deactivation. MWNTs productivity reached the highest value of 0.45 $g_C/g_{cata}$ at temperature of 600 $^{o}$C, ethylene molar fraction of 0.50, weight of catalyst 20 g and 60 minutes of duration.

In terms of quality, increasing reaction temperature resulted in the better graphitized MWNTs. The average diameters of synthesized MWNTs was approximately 7 nm for all conditions tested.

The analysis of effluent gas indicated that ethane could decompose to form MWNTs at the temperature above 650 $^{o}$C whereas methane did not react over the temperature range tested. The kinetic parameters namely pre-exponential coefficient and activation energy of MWNTs synthesis were found to be 13.21 $g_C/g_{cata}$/min and 65.3 kJ/mol, respectively. The activation energy of MWNTs formation matches well with that of carbon diffusion in liquid cobalt.

Department : Chemical Technology Student's Signature .....
Field of Study : Chemical Technology Advisor's Signature .....
Academic Year : 2011 Co-advisor's Signature .....

# ACKNOWLEDGEMENTS

This dissertation would not have been accomplished without the considerable assistance of the following persons and organizations:

I would like to express my sincerest gratitude and appreciation to my advisors Prof. Dr. Somsak Damronglerd, and my co-advisors, Prof. Dr. Brigitte CAUSSAT-BONNANS, who greatly contributed to this dissertation, for their providing me with insights and guidance to recognize my mistakes, giving me an invaluable suggestion and constant encouragement. Especially, I would like to extend my appreciation to Assoc. Dr. Hugues VERGNES for his care while I staying in France. Furthermore, I would like to sincere appreciation to Dr. Kunakorn Poochinda, Assoc. Prof. Dr. Nuttaya Pongstabodee, Assoc. Prof. Dr. Tawatchai Charinpanitkul and Dr. Sumate Charoenchaidet for their participation on the thesis chairman and committees. Moreover, I would also like to sincere appreciation to Prof. Dr. Philippe KALCK and Prof. Dr. Philippe SERP for their commitment on the Diplôme de Recherche Universitaire (DRU).

I would like to acknowledge the Royal Golden Jubilee Grant of Thailand Research Fund, Embassy of France in Thailand and Chulalongkorn University Graduate School for financial contribution to this research. I would also like to acknowledge LGC/ENSIACET-INPT, LCC/ENSIACET-INPT, Arkema Inc. and the Department of Chemical Technology, Faculty of Science, Chulalongkorn University for supplying valuable materials and equipment. In addition, I would like to acknowledge Mr. Michel MOLINIER for his technical assistance in the modification of FB-CVD reactor and Center of Excellence in Particle Technology, the Department of Chemical Engineering, Faculty of Engineering, Chulalongkorn University, especially to Mr. Sakhon Ratchahat for Raman spectroscopic analysis.

I would like to give my special thanks to the officers, my colleagues' friends in Chulalongkorn University and ENSIACET-INPT and my family for their eternal support, love and encouragement.

Finally, I would like to give a heartfelt thanks to Miss Supaporn Khangkham who is always beside me and lightens adversity by dividing and sharing it. Without her, this thesis could certainly never have become a reality.

# CONTENTS

Page

Page

# LIST OF TABLES

TABLE Page

# LIST OF FIGURES

FIGURE Page

FIGURE Page

FIGURE Page

# CHAPTER I

# INTRODUCTION

## 1.1 Rationale

After the last two decades of their first discovery as a by-product on the cathode of an arc-discharge reactor during fullerene production by Sumio Iijima, carbon nanotubes (CNTs) have been anticipated to be "materials for the future" owing to their excellent mechanical, electrical, thermal and magnetic properties which allow these nanostructure materials to be applied for various applications such as, catalysis, hydrogen storage media, polymer additives, microelectronic devices, chemical sensors, drug delivery systems and so on. (Phillipe et al., 2007; Paradise et al., 2007). Nowadays, they already become one of the major issues which are driving scientific knowledge and innovation. Among the several techniques that have been developed to produce CNTs, chemical vapor deposition shows the greatest potential to industrialize due to its simplicity, considerable low operating cost and high MWNTs productivity. This method is often conducted with the presence of catalyst, known as catalytic chemical vapor deposition (CCVD), in which a hydrocarbon precursor is catalytically decomposed over an active metal. Moreover, fluidization has been applied with CCVD process to enable the continuous producing bulk quantities of CNTs, known as fluidized bed catalytic chemical vapor deposition (FB-CCVD). The important advantages of FB-CCVD reactors are excellent heat/mass transfer, owing to the large contact areas of bed, that keep the process at the uniform temperature and reactant

concentration (Corrias et al., 2003; Escobar et al., 2007; McCaldin et al., 2006; Morançais et al., 2007; Venegoni et al., 2002; Wang et al., 2002; Yu et al., 2003). Among various types of carbon precursors used for MWNTs synthesis, ethylene which has been used as a reactant in general chemical industry is one of the most interesting carbon sources since its moderate thermal stability allows this specie to be readily decomposed at low temperature with controllable rate (Corrias et al., 2005; Morançais et al., 2007; Phillipe et al., 2009). In order to synthesis CNTs in a massive scale, the effect of process parameters on CNTs formation, their physical properties as well as kinetic parameter should be clarified. The understanding of them is very important to design, manipulate, optimize and industrialize the process.

## 1.2 Purpose of this study

To study the synthesis of multi-walled carbon nanotubes (MWNTs) over cobalt supported on alumina powders at relatively low temperature by fluidized-bed catalytic chemical vapor deposition (FB-CVD) method which offers a feasibility of economical large scale production of high-quality MWNTs.

### Objectives

1. To synthesize multi-walled carbon nanotubes using ethylene as carbon precursor.
2. To investigate the influence of operating parameters on the synthesis of multi-walled carbon nanotubes by fluidized-bed chemical vapor deposition.

3. To study physical properties of synthesized carbon nanotubes.

## 1.3 Scope of the dissertation

1. Development of a system for fluidized-bed chemical vapor deposition process to synthesize MWNTs by using ethylene as carbon precursor.

2. Catalyst characterization

- Physical Properties
- Chemical Properties

3. MWNTs synthesis

- The effect of temperature on MWNTs synthesis
- The effect of $C_2H_4$ molar fraction on MWNTs synthesis

4. MWNTs characterization.

- Physical Properties

5. Conclusion and writing thesis

## 1.4 Anticipated benefits

1. To produce multi-walled carbon nanotubes.
2. To obtain the optimization of the operating conditions for the synthesis of multi-walled carbon nanotubes.

## 1.5 Format of the dissertation

The dissertation was formatted in a chapter form. Background, purpose and scope of this research work were presented in Chapter I. Theoretical information and

literature review were mentioned in Chapter II. Material used in this work and methodology, accompany MWNTs synthesis, catalyst and MWNTs characterization, were described in Chapter III. In this research involved three main parts: fluidized-bed catalytic chemical vapor deposition process to synthesize MWNTs was revealed in Chapter IV, qualitative characterization of MWNTs was evaluated in Chapter V and kinetic evaluation of MWNTs synthesis was studied in Chapter VI. Finally, conclusions were introduced in Chapter VII.

# CHAPTER II

# THEORY AND LITERATURE REVIEWS

In this chapter a short overview over the current knowledge which is important for the understanding of the subjects that are addressed in this work will be presented. First, a short overview of CNTs will be given in section 2.1 touching their history, structure, properties and application respectively. Further the present state of work regarding the CNTs synthesis will be shown in section 2.2 with major importance on chemical vapor deposition as main method used in this work. Common techniques used for characterization of carbon nanotubes will then be presented in section 2.3. Finally, literature reviews will be enumerated in section 2.4

## 2.1. Carbon nanotubes

### 2.1.1 Introduction

The basic crystalline forms of elemental carbon have been a well-known material for a long time. They have been used extensively across history in the forms of diamond, graphite and amorphous carbon. Over the last twenty years, some new carbon atom arrangements have been discovered. In 1985, Kroto reported the discovery of the C60 molecule, also known as buckyball (Kroto et al., 1985). This

new form paved the way for a completely new class of carbon molecules: the fullerenes. A wide variety of atom arrangements is made possible by the range of configurations of the electronic states of carbon atoms. The most common of these structures are shown in Figure 2.1.

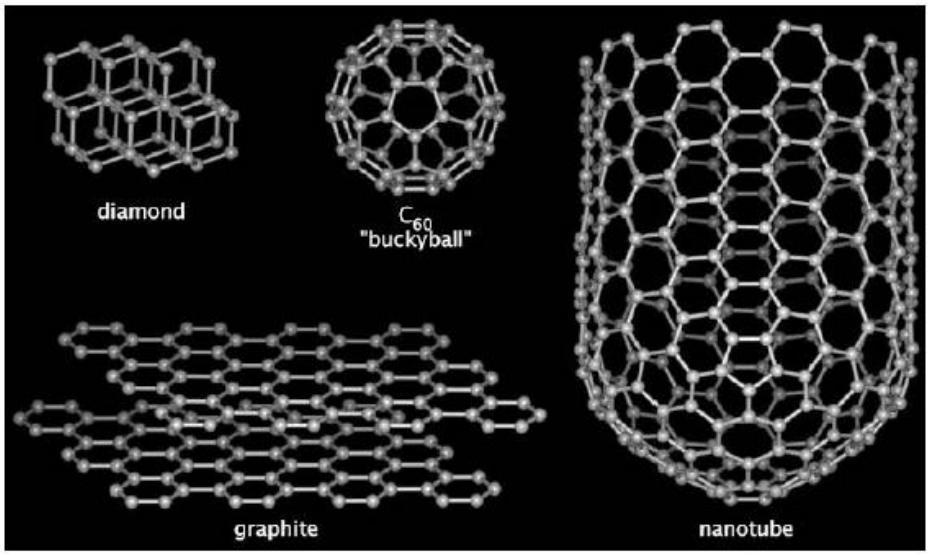


**Figure 2.1** Schematic of different types of carbon structure (Saito et al., 1998)

One of the fullerene structure is the carbon nanotubes, whose first transmission electron microscopy (TEM) images are believed to have published in the Journal of Physical Chemistry of Russia in 1952 (Radushkevich et al., 1952) but without clear distinction of the walls due to the inadequate performance of TEM as given in Figure 2.2 (left) (reprinted by Monthioux and Kuznetsov, 2006). However, as claimed by Monthioux and Kuznetsov, the referred Russian article was not well known and cited due to its difficult accessibility. It was not until 1991, the first clear TEM image of CNTs was represented by Iijima in a famous "NATURE" journal (Iijima, 1991) as given in Figure 2.2 (right). After the publication of Iijima's report,

the research of this nanomaterial has thenceforth exploded to become one of the major issues which are driving scientific knowledge and innovation. The name "carbon nanotubes" is derived from their size which is only a few nanometers wide. By definition, carbon nanotube is a cylinder of rolled up graphene (graphite sheet), which is capped with a half fullerene molecule at the end.

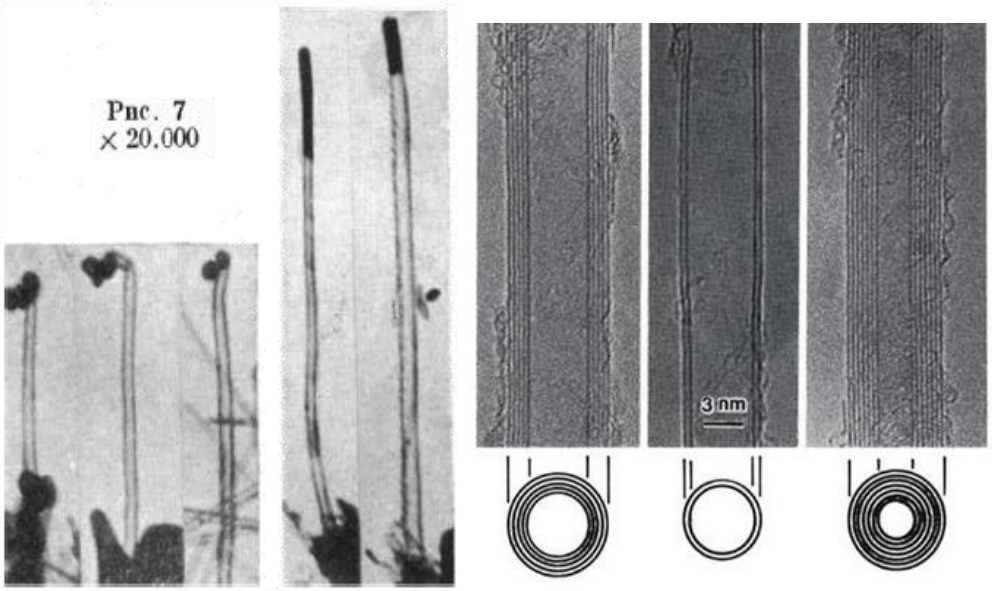


**Figure 2.2** Examples of TEM images of carbon nanotubes; (left) as published by Radushkevich and Lukyanovich in 1952 (reprinted by Monthioux and Kuznetsov, 2006) and (right) as published by Iijima in 1991 (Iijima, 1991)

### 2.1.2 Types of carbon nanotubes

CNTs are classified according to the number of rolled up graphene which form concentric cylindrical carbon layered walls.

#### 2.1.2.1 Single-walled carbon nanotube (SWNT)

The structure of SWNT can be described by wrapping a one-atom-thick layer of graphene into a seamless cylinder. Most of SWNT have a typical diameter of about 1.4 nm, which is similar to a buckyball (C60), with a tube length that can be many thousands of times larger.

#### 2.1.2.2 Multi-walled carbon nanotubes (MWNTs)

MWNTs consist of several tubes which are packed concentrically in each other. A special kind of those MWNTs is the double-walled carbon nanotubes (DWNTs) which are built of exactly two tubes. The interlayer distance is close to the distance between graphene layers in graphite, about 0.34 nm.

### 2.1.3 Atomic Structure of CNTs

The structure of CNTs can be classified as achiral or chiral. The first type can be defined as a nanotube whose mirror image has the same structure as the original. There are two cases of achiral nanotubes: armchair and zigzag, which correspond to the shape of their cross-sectional ring. Nanotubes whose mirror image is different to the original are called chiral (Saito et al., 1998). Structure of armchair, zigzag and chiral CNTs are illustrated in Figure 2.3.

### 2.1.4 Chiral vector and chiral angle

In order to expound the chiral structure of CNTs, the chiral vector and chiral angle are assigned. As represented in Figure 2.4, a graphene sheet is wrapped into a nanotube following a way by which all of the points along the dash line AC coincide

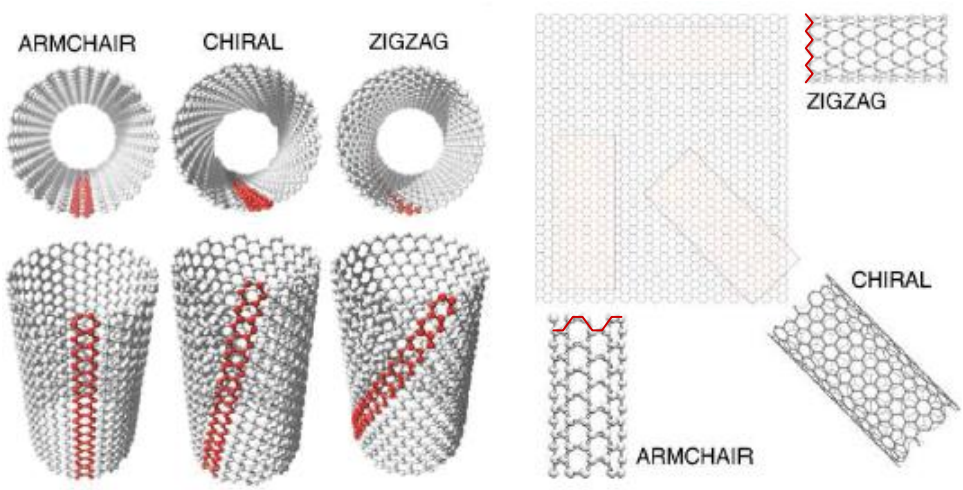


**Figure 2.3** Schematic illustrations of the structure of armchair, chiral and zigzag carbon nanotubes (left) and schematic diagram of nanotube formation by "rolling-up" a graphene sheet (right) (Kis, 2003)

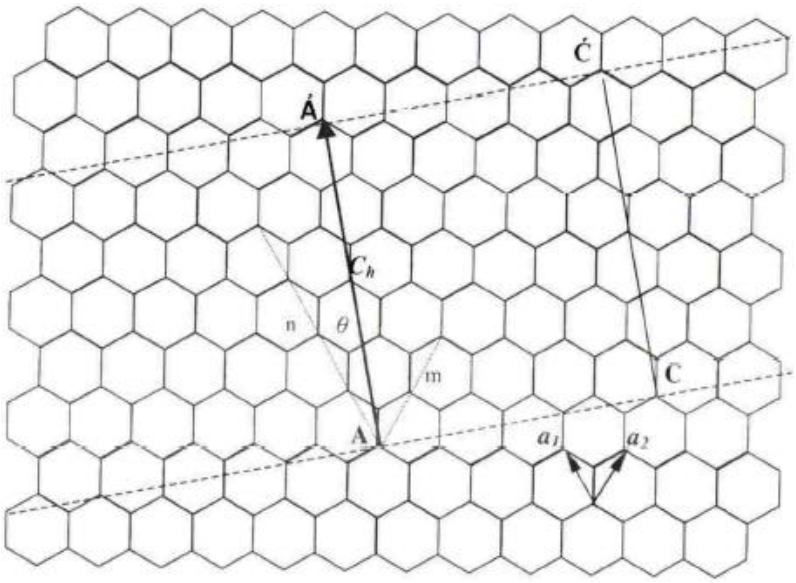


**Figure 2.4** Unrolled lattice of the (4,2) carbon nanotube (Liu, 2006)

with all the points along the dash line A'C' where dot A meets dot A' and dot C meets dot C'. The vectors $a_1$ and $a_2$ are real space unit vectors of the two-dimensional hexagonal lattice. Taking a C-C bond distance as $a_{c\text{-}c}$ (1.42 Å for $sp^2$-hybridized

carbon), the lengths of vectors $a_1$ and $a_2$ are $\sqrt{3}a_{c-c}$. Chiral vector ($C_h$), which is defined as the vector perpendicular to the axis of the resulting nanotube, can be written as :

$$C_h = na_1 + ma_2 \equiv (n,m), \text{ (n,m are integers, } 0 \leq m \leq n)$$

The circumference of nanotube, expressed as L, can be calculated from the chiral vector,

$$L = \sqrt{3}\, a_{c-c}\sqrt{n^2 + m^2 + nm}$$

The diameter of tube, expressed as $d_t$, can then be given as

$$d_t = \sqrt{3}\, a_{c-c}\sqrt{n^2 + m^2 + nm}\ /\pi$$

The chiral angle ($\theta$) is defined as the angle between the vectors $C_h$ and $a_1$. Based on the geometry of the nanotube and the definitions of the chiral parameters, the value of $\theta$ must be between 0° and 30°

$$\sin\theta = \frac{\sqrt{3}m}{2\sqrt{n^2 + m^2 + mn}}$$

Armchair, zigzag and chiral nanotubes have chiral vectors of (n, n), (n, 0) and (n, m) where n > m respectively. Their chiral angles are 30°, 0° and 0°< 0 <30° respectively.

2.1.5 Properties of CNTs

2.1.5.1 Mechanical property

CNTs are one of the strongest materials ever discovered. They exhibit stupendous mechanical properties in the axial direction owing to the entire $sp^2$ hybridization in their structure. As demonstrated in Table 2.1, the tensile strength

**Table 2.1** Mechanical and structural properties of various types of CNTs in comparison with some well-known materials (O'Connell, 2006)

| Property | SWNT | DWNT | MWNT | Carbon fibre | Steel | Kevlar |
|---|---|---|---|---|---|---|
| Young's modulus [Gpa] | 640 | | 1060 | 150 - 950 | 190 - 210 | 130 |
| Tensile strength [GPa] | | 23 - 63 | 63 | 4-7 | 0,5 - 2 | 3 - 4 |
| Density [g/cm3] | 1,3 – 1,5 | 1,5 | 1,8 - 2 | 1,7 – 2,2 | 7,75 – 8,1 | 1,44 |
| Diameter | ca . 1nm | ca. 5nm | ca. 20nm | 60 – 100nm | | 5 – 10 um |

of MWNTs was reported to be up to 63 GPa or even up to 150 GPa in a number of literatures (Yu, 2004; Demczyk et al., 2002). An elastic modulus in the order of 1,000 GPa, which is five times the value of stainless steel (about 200 GPa), was both obtained from theoretical predictions and various experimental observations (Yu, 2004). CNTs also show the flexibility, not because of any plastic deformation, but to their high strength and the unique capability of the hexagonal network to distort for relaxing stress. Mechanical properties of CNTs are highly associated with the sum of local defects which cause a local distortion of the graphite lattice structure. As reported by Salvetat (Salvetat et al., 1999), Young's modulus for MWNTs are dependent on the degree of order within the tube walls as demonstrated in Figure 2.5, where the Young's modulus decreases as the disorder increases. It should be noted that theoretical calculated results may vary with the type of calculation method. Moreover, experimental observations on mechanical properties of CNTs were reported with only moderate precision due to their nano-size that causes difficulties with precision of the experiments. In general, it was observed that elastic modulus of SWNT and MWNTs vary from 0.32 to 1.47 and 0.27 to 0.95 TPa, respectively.

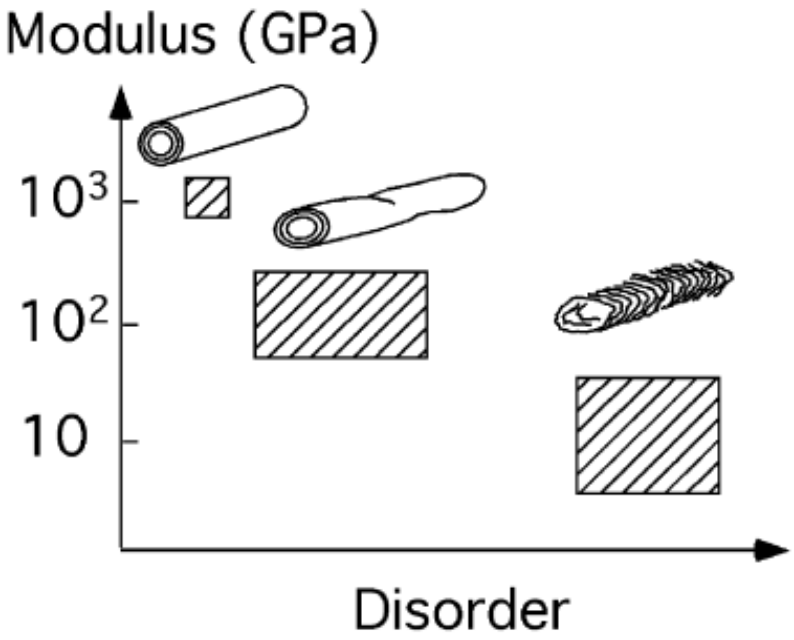


**Figure 2.5** Modulus vs. disorder in MWNTs (Salvetat et al., 1999)

2.1.5.2 Thermal property

Due to their large aspect ratio, carbon nanotubes are expected to have an unusually high thermal conductance along their axis due to an effect called "ballistic conduction" but are insulators in their radial direction. The room temperature thermal conductivity of SWNT has been predicted to be extremely high, exceeding even that of graphite or diamond (Hone et al., 1999). For a single (10,10) SWNT, the thermal conductivity was estimated to be 6,600 $W \cdot m^{-1} \cdot K^{-1}$, which exceeds the reported room temperature thermal conductivity of isotopically pure diamond by almost a factor of about 2 (Berber et al., 2000). Carbon nanotubes have estimated temperature stability up to 2,800 °C in vacuum and 750°C in air (Collins and Avouris, 2000). Table 2.2 summarizes thermal conductivity of CNTs and also of two good thermally conductive.

**Table 2.2** Thermal conductivity of different CNTs types and some well-known materials (O'Connell, 2006)

| | SWNT | MWNT | Carbon fibres | Silver | Copper |
|---|---|---|---|---|---|
| Thermal conductivity[W/mK] | 6600 (theor.) | 3000 (exp.) | 8 - 1100 | 429 | 401 |

2.1.5.3 Electrical property

Most material conductors can be classified as either metals or semiconductors. The electrical properties of a material depend on the separation between the valence band filled with electrons and the conduction band that is empty as shown in Figure 2.6.

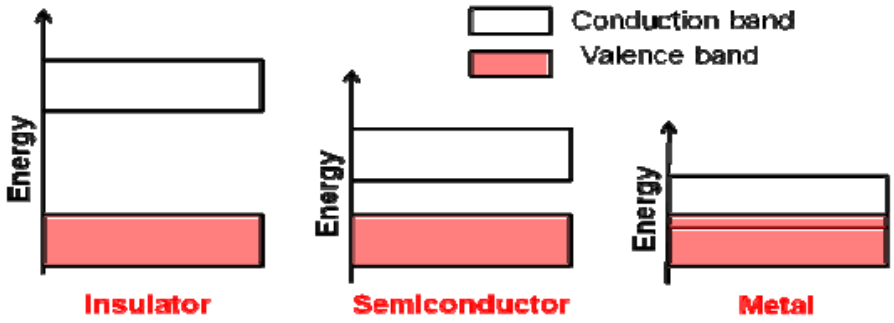


**Figure 2.6** Electrical properties of different materials (Cheng, 2010)

In metals, the two bands are overlapped thus many electrons can access the conduction band easily. In case of semiconductor, there is a band gap (less than 4 eV) field. Within graphene, there is a narrow path for a few electrons to a conduction state without any external boost, as shown in figure 2.7. Therefore, graphene is known to be a semimetal or zero-gap semiconductor (Collins and Avouris, 2000; Anantram and Leonard, 2006).

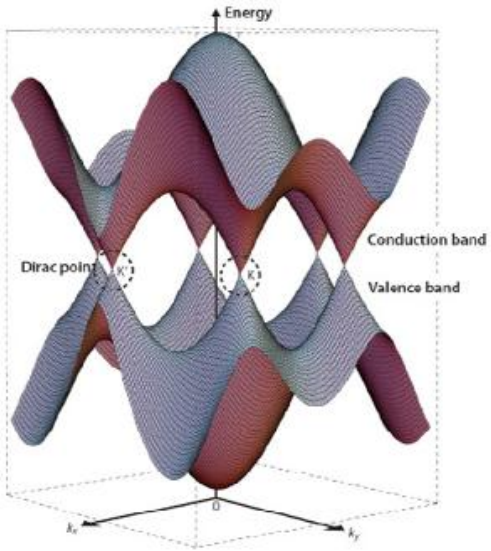


**Figure 2.7** Energy band structure in graphene (Ando, 2009)

Although SWNT is structurally similar to a graphene, they can be either metallic or semiconducting depending on the tube diameter and the chirality. This dual ability of CNTs to be both metallic and semiconducting depending only on their geometry is one of their most astonishing features. Studies have shown that for given chiral vector directions, the electrical properties of the SWNT can be predicted. If the difference of the vector integers, given by n–m = 3k (k is an integer), then the nanotube is metallic. Otherwise the electrical behavior of the tube will be semiconducting. The subsequent electrical behavior resulting from these integer combinations is shown in Figure 2.8. The chiral vector integer pairs that produce metallic SWNT are represented as hollow circles, while semiconducting SWNT producing pairs are shown as dark circles.

The 1-D structure of CNTs is associated with a specific type of band structure that can give rise to unusual electrical transport properties. Due to the 1-D nature of

their band structure, SWNT exhibit peaks or spikes in their density of state (DOS) diagrams as shown in Figure 2.9. The peaks in the DOS diagrams are called van Hove singularities, which are discontinuities in the density of states of a solid, and are representative of the energy levels where the electrons tend to exist in the orbitals.

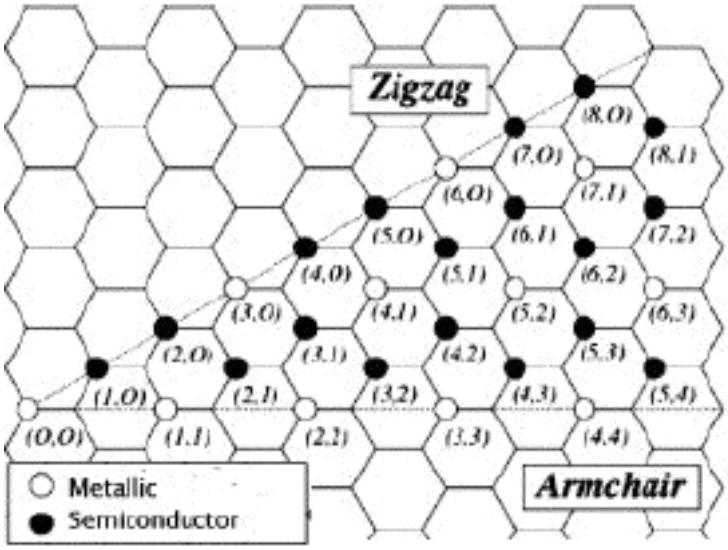


**Figure 2.8** Conductivity roadmap indicating the conductivity of SWNT produced with a chiral vector of given (n,m) integers (Belin and Epron, 2005)

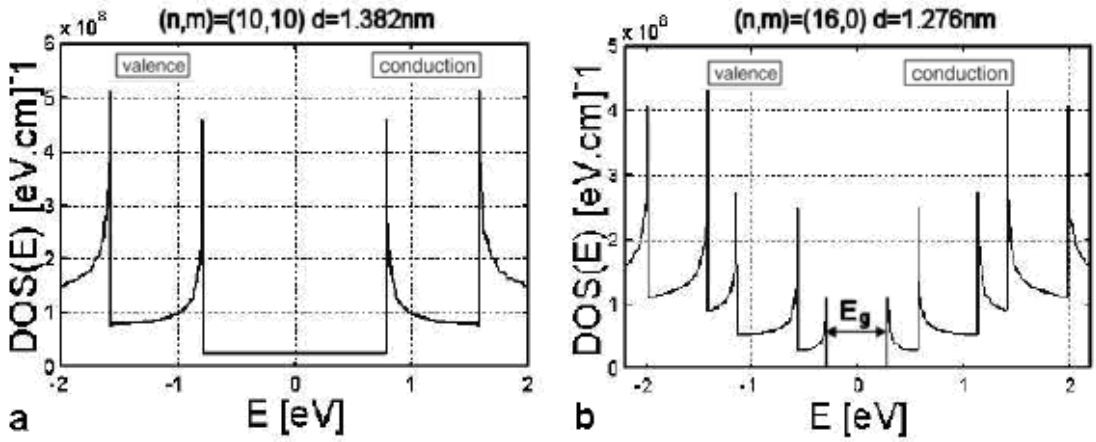


**Figure 2.9** Schematic diagram of electronic density of states for (a) metallic and (b) semiconducting SWNT (Yu and Brus, 2001)

One distinguishing difference between the semiconducting and the metallic DOS diagrams are that electrons can exist at zero energy. In the outer singularities of the semiconducting tube, there exists a need to transition between peaks, as opposed to the metallic tube where electrons can move more readily. The band gaps between the van Hove singularities seen in Figure 2.9 can be estimated using the theoretical prediction,

$$E = \frac{k a_{c-c} \gamma_o}{d}$$

In this relation, E is the transition energy, $a_{c-c}$ is the nearest-neighbor carbon-carbon distance, 0.142 nm, $\gamma_o$ is the nearest-neighbor carbon-carbon interaction energy, 2.9 eV (Brown et al., 2000), d is the SWNT diameter and k is an integer constant. The values of k can be 2, 4 and 8 for the 1st, 2nd and 3rd van Hove singularities in semiconducting tubes and 6 and 12 for the 1st and 2nd van Hove transitions in metallic tubes respectively (White and Mintmire, 1998). Because of statistical probability and restrictions on the relative diameters of the individual tubes, one of the shells, and thus the whole MWNTs are usually metallic tubes.

Electronic transport in metallic SWNT and MWNTs has been reported to be ballistic over long lengths, up to a few hundred nanometers, at room temperature and it is due to the nearly one-dimensional electronic structure of nanotubes. Ballistic transport implies there will be no energy dissipation in the conductor and heat dissipation will only occur at the contacts. This enables nanotubes to carry high currents with negligible heating (Avouris, 2002; Wang et al., 2003). In theory, metallic nanotubes can carry an electric current density of $4 \times 10^9$ A•cm$^{-2}$, which is more than 1,000 times greater than those of metals such as copper (Hong and Myung,

2007) where for copper interconnects current densities are limited by electromigration. Table 2.3 gives an example of electrical properties of CNTs.

**Table 2.3** Electrical properties of carbon nanotubes (Teo et al., 2004)

| | | | |
|---|---|---|---|
| Typical resistivity of single and multiwall nanotube | $10^{-6}$ Ω m | Single wall nanotube bandgap—whose $n-m$ is divisible by 3 | 0 eV |
| Typical maximum current density | $10^{7}$–$10^{9}$ A cm$^{2}$ | whose $n-m$ is nondivisible by 3 | 0.4–0.7 eV |
| Quantized conductance, theoretical/measured | $(6.5\ k\Omega)^{-1}/(12.9\ k\Omega)^{-1}$ | Multiwall nanotube bandgap | ~0 eV |

2.1.6 Applications of carbon nanotubes

The remarkable properties of carbon nanotubes have attracted the attention of researchers. Their low density, high strength, electrical and thermal conductive properties bring up the possibility of novel structures with CNTs which possess extraordinary properties. The following are some of the most significant applications of CNTs:

- High performance nanocomposites
- Nanotube based field emitters
- Nanoelectronic devices
- Fuel cell applications
- Probes for Atomic Force Microscope and sensors
- Vessel for drug delivery
- Superconductors

Carbon nanotubes have been described as the ultimate carbon fiber ever made. Carbon fibers have a very high specific strength and are excellent load-bearing reinforcements in composites. They have been used as reinforcements for a range of

products from spacecraft, aircraft body to tennis racquets. Thus, CNTs whose strength is several times higher than carbon fibers seems to be excellent candidates to be used as reinforcements in composites. CNTs also are capable of sustaining large strains in tension without fracture. Therefore, CNTs when used in a structural polymer composite will increase the toughness of the composite by absorbing energy due to their highly flexible behavior. This has proved to be an important factor especially in CNTs-based ceramic composites. In comparison to carbon fibers, the low density of CNTs is a clear advantage in composites. In addition, CNTs also offer additional properties such as increased electrical conduction to the composites.

CNTs also hold a lot of promise in the field of vacuum electronics. Field emission is a phenomenon where electrons are emitted when materials are subjected to a sufficiently high electric field. Electron field emission materials have been extensively used in applications such as flat panel displays, electron guns in electron microscopes and microwave amplifiers (Castellano, 1992.). Carbon nanotubes have the right combination of properties such as structural integrity, nanometer size diameter, high electrical conductivity and chemical stability which are essential for good electron emitters. (Dresselhaus et al., 2001). SWNT generally has a better structural perfection than MWNTs and hence are better candidates for field emitters. Although nanotubes have some clear advantages, the application of nanotubes is limited by the factor that they have a low emission site density i.e. the number of functional emitters per unit area is too low for high resolution display applications.

The nanotubes with their extremely uniform dimensions, small size, flexibility, high conductivity and high mechanical strength are excellent candidates

for use as nanoprobes. These probes can be used in applications such as nano-lithography, high resolution imaging, drug delivery, nano-electrodes, field emitters and sensors. CNTs have been used for imaging at the end of a scanning probe microscope (Dai et al., 1996). Since MWNTs tips are conducting, they can be used in AFM, STM and other scanning probe instruments like electrostatic force microscope. CNTs tips have a distinct advantage of being small in size. Hence, it can be used to image small variations which are impossible using the larger probes like silicon or other metal tips. Also, as the nanotubes have high elasticity, the tips do not crash on contact with the substrates. An impact on contact will lead to the buckling of the nanotube which is generally reversible. However, the main challenge faced in this application is attaching the individual nanotubes to the conventional tips of scanning probe microscopes. In addition, it has also been found that nanotubes can be used for surface manipulation. It has been shown that if a pair of nanotubes can be positioned appropriately on an AFM tip, they can be used as tweezers to pick up and release nano-scale structures on surfaces. Research has also shown that electrical resistivity of SWNT changes on exposure to certain gases. The change in resistance can be used to detect the presence of these gases so that the nanotube can be used as a sensor.

## 2.2 Carbon nanotubes synthesis

Since carbon nanotubes have so many excellent properties and potential applications, it is highly desirable to have large quantities of pure carbon nanotubes. The production of carbon nanotubes with a high order of purity and uniformity has been still interesting subject of interest for the researchers. Nanotubes come in

different types and vary significantly depending on the synthesis procedures. The manufacturing of the carbon nanotubes mainly include arc discharge, laser ablation and chemical vapor deposition (CVD).

2.2.1 Arc-discharge

The principle of this method is the generation of an electric arc between two closely spaced graphite electrodes (<1 mm apart). The schematic diagram of typical CNTs production apparatus is shown in Figure 2.10. After evacuating the chamber with a vacuum pump, an appropriate ambient inert gas is introduced at low pressure. Once the pressure is stabilized, a DC arc voltage (50 to 120 A, ~30 V) is applied.

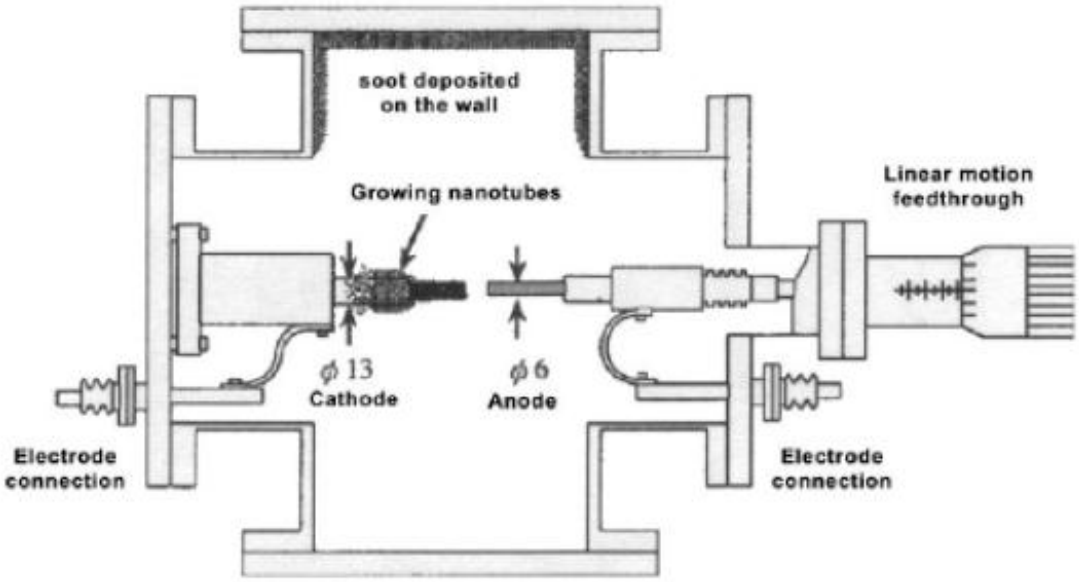


**Figure 2.10** Schematic diagram of arc-discharge setup (Saito et al., 1996)

A high-temperature plasma (>3000 ºC) is created between the two graphite rods. The carbon contained in the anodic (negative) electrode sublimes because of the high temperatures caused by the discharge and condenses rapidly as a hard cylindrical

deposit on the cathodic rod (Ando et al. 2004). This method can produce both SWNT and MWNTs. Large-scale synthesis of MWNTs by arc-discharge has been achieved under inert atmosphere (Ebbesen and Ajayan, 1992; Colbert et al., 1994). When a graphite rod containing metal catalyst (Fe, Co, etc.) is used as the anode with a pure graphite cathode, single-walled carbon nanotube (SWNT) is generated (Iijima and Ichihashi, 1993; Bethune et al., 1993). Compared to other methods, the arc-discharge produces CNTs with less defective. However, more by-products such as amorphous carbon, non-tubular fullerenes and also catalytic metal particles can be formed during the process. This process has scale up limitations since it needs to be stopped to remove the product from the chamber.

### 2.2.2 Laser ablation

The laser ablation technique for synthesizing carbon nanotubes was first reported in 1995 (Guo et al., 1995). The laser ablation apparatus is shown in Figure 2.11.

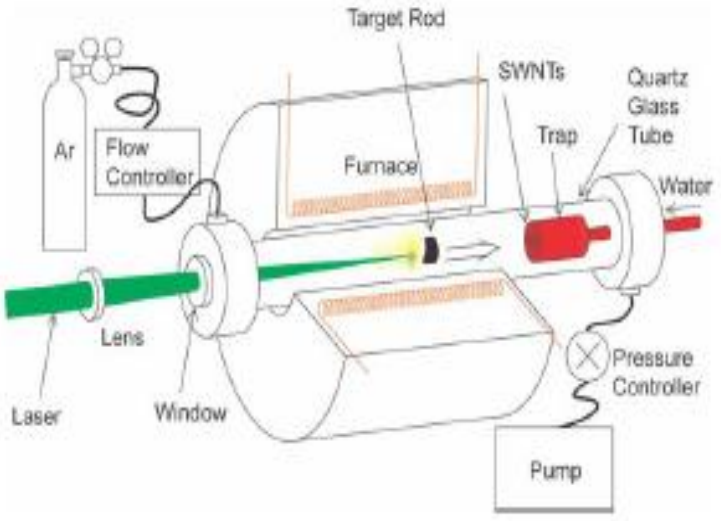


**Figure 2.11** Schematic diagram of laser ablation setup (Ando et al., 2004)

In laser ablation, a laser is employed to vaporize a graphite target held in a controlled environment oven. The carrier gas used can be argon or helium, and the oven temperature is approximately 1,200°C (Thostenson et al., 2001). The condensed material, which has a significant amount of CNTs and nanoparticles, is collected on a cool target (water cooled Cu collector). CNTs produced by laser ablation are purer (up to about 90 % purity) than those produced in the arc discharge process. This process has been known as tool for mass production of SWNT in case a target of graphite containing metal catalyst is used. The SWNT produced by this technique are normally bundles with narrower diameter distribution, normally 1.0 to 1.8 nm with an average of 1.4 nm. Unfortunately, the laser technique is not economically advantageous because the process requires high-purity graphite rods, the laser powers required are high (in some cases two laser beams are required), and the amount of CNTs that can be produced per day is not as high as the arc discharge method (Guo et al., 1995).

### 2.2.3 Chemical vapor deposition (CVD)

The two methods mentioned above lack the ability to be scaled-up. Another disadvantage of the two methods is that the synthesis temperatures are too high and therefore they consume huge energy and are not easy to be properly controlled. Chemical vapor deposition (CVD), the method which had been universally used to deposit metals on Si substrates in the semiconductor industry (Harper, 2002), was adopted to overcome some of the problems with the laser-ablation and arc-discharge methods. Figure 2.12 shows a diagram of the setup used for CNTs growth by CVD. CVD works as follows: a substrate is placed in a reaction chamber with an inert gas and heated to an elevated temperature. Hydrocarbon gases are then introduced into the

hot reaction chamber at a specified flow rate, and come into contact with catalysts on the substrate surface. As reactants react with the catalysts, CNTs are grown on the substrate. CVD is operated at much lower temperature (usually less than 1,000 °C) and yields much more products than the two earlier methods. However, due to the low growth temperature, CNTs prepared by CVD have more defects. This problem is a main challenge for CVD in the attempt to produce large-quantity of defect-free CNTs. There are several different reported methods of CVD.

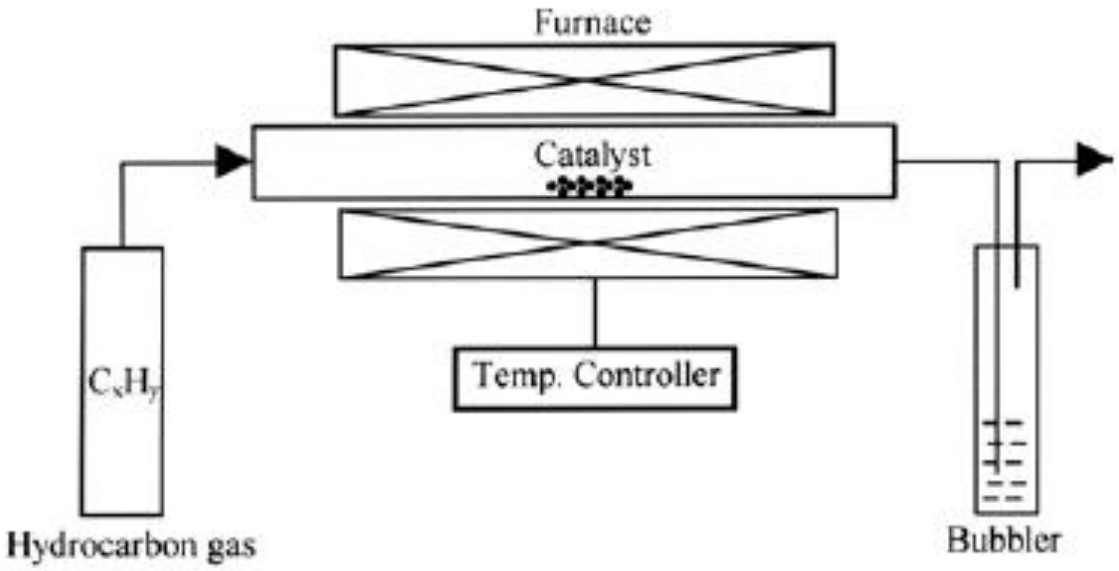


**Figure 2.12** Schematic diagram of CVD apparatus (Ando et al., 2004)

There are several different reported methods of CVD for example;

***Thermal CVD***: ln a thermal CVD (Huang et al., 2002; Li et al., 2002; Zhang et al., 2002), the catalyst is derived from a sublimable precursor or a precursor which has been pre-deposited onto the growth substrate and then carbon source is decomposed in a pyrolysis furnace, forming carbon nanotubes.

***Hot-filament CVD***: The key characteristic of a hot-filament CVD (Jiang et al., 2002; Mahan et al., 2002) is that, a tungsten filament, with big current flow, operating at a temperature around 1,000 ºC, is placed inside the reaction chamber in order to crack the carbon source into carbon species, and to heat the growth substrate (where growth temperature is lower than 700 ºC) which is set above the filament.

***Plasma-enhanced CVD***: In a plasma-enhanced CVD (Huang et al., 1998; Bower et al., 2000; Tu et al., 2002), the catalyst forms a thin layer on the top of the growth substrate beforehand. In a typical process, plasma enhances the process of dissociating the hydrocarbon into carbon species and therefore increases carbon supplies for the growth of CNTs. Compared with the two CVD methods mentioned above, plasma-enhanced CVD yields higher growth rate and better alignment. However, individual CNTs, which are grown by plasma CVD, contain more contents of defects in their sidewalls and are of poor quality because of the low growth temperature and the rapid growth rate.

2.2.3.1 Growth mechanism

CNTs growth mechanism has been debatable right from its discovery. Based on the reaction conditions and post-deposition product analyses, several groups have proposed several possibilities which are often contradicting. Therefore, no single CNTs growth mechanism is well established. Nevertheless, widely-accepted most-general mechanism can be outlined as follows. A hydrocarbon vapor when comes in contact with the hot metal nanoparticles, first decomposes into carbon and hydrogen

species; hydrogen desorbs away and carbon diffuses into the metal. After reaching the carbon-solubility limit in the metal at that temperature, as-dissolved carbon precipitates out and crystallizes in the form of a cylindrical network having no dangling bonds and hence energetically stable. Hydrocarbon decomposition (being an exothermic process) releases some heat to the metal's exposed zone, while carbon crystallization (being an endothermic process) absorbs some heat from the metal's precipitation zone. This precise thermal gradient inside the metal particle keeps the process on.

Now there are two general cases (Figure 2.13 a). When the catalyst-substrate interaction is weak (metal has an acute contact angle with the substrate), hydrocarbon decomposes on the top surface of the metal, carbon diffuses down through the metal, and CNTs precipitates out across the metal bottom, pushing the whole metal particle off the substrate (Figure 2.13 a(i)). As long as the metal's top is open for fresh hydrocarbon decomposition, the concentration gradient exists in the metal allowing carbon diffusion, and CNTs continues to grow longer and longer (Figure 2.13 a (ii)). Once the metal is fully covered with excess carbon, its catalytic activity ceases and the CNTs growth is stopped (Figure 2.13 a (iii)). This is known as "tip-growth model". In the other case, (Figure 2.13 b) when the catalyst-substrate interaction is strong (metal has an obtuse contact angle with the substrate), initial hydrocarbon decomposition and carbon diffusion take place similar to that in the tip-growth case, but the CNTs precipitation fails to push the metal particle up; so the precipitation is compelled to emerge out from the metal's apex (farthest from the substrate, having minimum interaction with the substrate). At first, carbon crystallizes out as a hemispherical dome (the most favorable closed-carbon network on a spherical nano-

particle) which then extends up in the form of seamless graphitic cylinder. Subsequent hydrocarbon decomposition takes place on the lower peripheral surface of the metal, and as-dissolved carbon diffuses upward. Thus CNTs grows up with the catalyst particle rooted on its base; hence, this is known as "base-growth model" (Kumar, 2011).

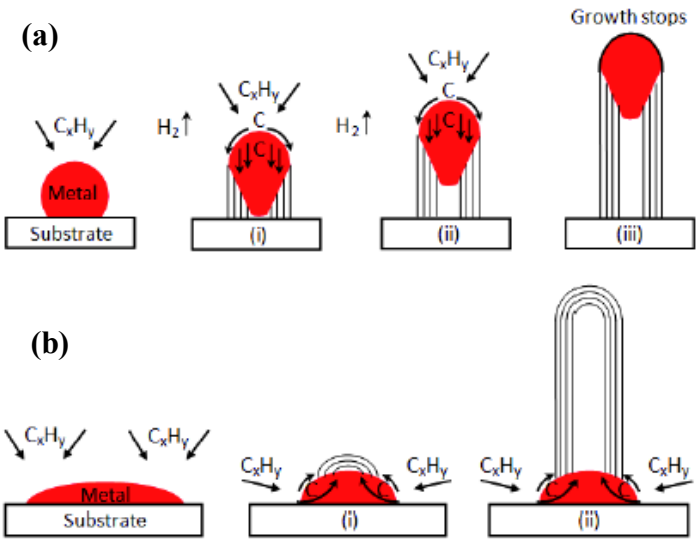


**Figure 2.13** Widely-accepted growth mechanisms for CNTs: (a) tip-growth model and (b) base growth model (Kumar, 2011)

2.2.3.2 Physical state of the catalyst

The first effort to observe the carbon filament growth process in-situ was made by Baker in 1972. By installing a gas-reaction cell in the TEM specimen chamber, they were able to perform carbon fiber growth in a temperature range of 600 °C to 1,200 °C at different gas pressures up to 225 torr (maximum), while the TEM column was maintained at sufficiently low temperature and pressure suitable for electron microscopy. For acetylene decomposition on nickel catalyst supported on silica and graphite supports at 600 °C, they clearly observed that the metal particles

changed it shape and moved up with a trail of carbon deposit (30–50 nm diameter). From the changing shape of the metal particle during fiber growth, they assumed that the catalyst was in liquid phase. The activation energy calculated for this growth was nearly same as the activation energy of carbon diffusion in liquid nickel; hence they suggested that carbon diffuses through the bulk metal and the fiber growth rate is diffusion controlled (Baker et al., 1972).

Similar tip-growth process was observed with Fe, Co and Cr catalysts (Baker et al., 1973). But in the case of acetylene decomposition on bimetallic (Pt-Fe) catalyst, the catalyst was observed to remain static on the substrate, while the carbon filament went on growing up. This led them to enunciate a base-growth model (Baker and Waite, 1975). It was explained that strong interaction between Pt-Fe and $SiO_2$ substrate kept the metal particle anchored to the substrate surface, and carbon precipitation occurred from the free upper face of the particle. Temperature and concentration gradients were thought to be the main driving forces for the continued growth dynamics. The filament growth was seen to be ceased when the particle was fully covered with the carbon cloud, but it could be reactivated by exposure to either hydrogen or oxygen at higher temperatures (Baker et al., 1972). Later, however, many scientists reported base-grown CNTs from Fe and Co catalysts on Si and $SiO_2$ substrates (Li et al., 1999; Bower et al., 2000). This indicates that the same set of hydrocarbon, catalyst and substrate may act differently in slightly different experimental conditions.

In 1984, Tibbetts explained why catalytically-grown carbon nanofibers were tubular. Because the surface free energy of the (0 0 2) basal plane of graphite is exceptionally low, the free energy required for a filament growth is minimum when graphite is in the form of a seamless cylinder circumfering the metal. And the inner core is hollow because inner cylindrical planes of small diameter would be highly strained, energetically unfavorable to form. He also explained the CNTs growth mechanism with a vapor-liquid-solid (VLS) model, originally formulated for Si, Ge whiskers and many other crystals (Tibbetts, 1984; Wagner and Ellis, 1965). Although this model is convincing and acceptable to a great extent, it is often doubted how Fe, Co, Ni etc. (normal melting point ~1500°C) could be in liquid state within 550 °C to 1,000 °C, the growth temperature of typical CNTs in CVD. Here it is important to note that the melting point of nanoparticles falls abruptly due to their high surface to volume ratio (Figure 2.14).

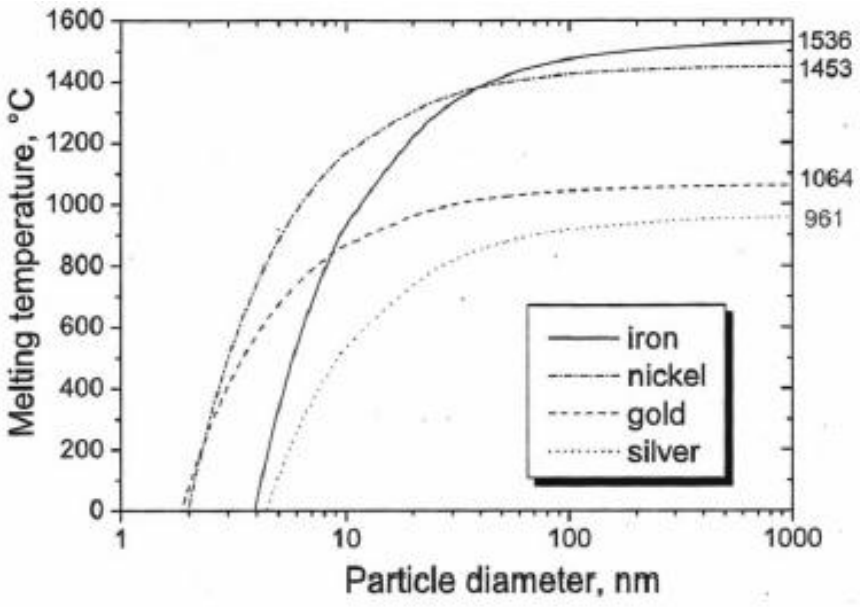


**Figure 2.14** Melting temperature of selected metals as a function of particle diameter. (Moisala et al., 2003)

For instance, 8 nm Fe and Au particle (or 4 nm Ni particle) can melt at about 800 °C. Typical CNTs growth temperature range is 700 °C to 900 °C, implying that in some cases the catalyst metal may be in liquid state, while in some cases it may be in solid state. Also, in any experiment, all particles are not strictly of the same size. So, it is still hard to say on the metal's state authoritatively. However, recalling that hydrocarbon decomposition on metal surface is an exothermic reaction, it is likely that the extra heat generated during hydrocarbon decomposition helps metal liquefaction. Hence the opinion of active catalyst being in liquid phase is somewhat acceptable, as reported by many scientists for CNTs growth (Ding et al., 2004; Harutyunyan et al., 2005).

2.2.3.3 Carbon Precursor

CVD growth of CNTs start with the gas phase carbon feedstock. Several different carbon containing compounds (Moisala et al., 2003) have been used as precursors, most common ones are: carbon monoxide (CO) (Zheng et al., 2002; Huang et al., 2004), Methane ($CH_4$) (Cassell et al., 1999), Ethylene ($C_2H_4$) (Hata et al., 2004), Acetylene ($C_2H_2$) (Patole et al., 2008), benzene ($C_6H_6$) (Yang et al., 2003), toluene ($C_7H_8$), Ethanol ($C_2H_5OH$) (Huang et al., 2006), and Methanol ($CH_3OH$). Each carbon precursor has an own decomposition temperature, thus resulting in a different nanotubes growth temperature. For example $CH_4$ is known to decompose at very high temperatures (> 900 $^oC$) over catalyst nanoparticles, whereas $C_2H_5OH$ starts self- decomposing at temperatures near 800 $^oC$. Although increased temperatures are required for higher rate of nanotubes growth, very high temperatures can initiate self-dissociation of gases which can cause catalyst poisoning. Apart from the temperature,

the dissociation rates of the precursor can also be controlled by the partial pressure of the species. For example, at high pressure CO dissociation rate increases, hence to achieve higher nanotubes yield, high pressure CO growth processes are used. A well-known example is the high pressure CO (HiPCO) process (Hafner et al., 1998). Similarly, low pressure growth has also been used to decrease catalyst poisoning to achieve ultra-long CNTs (Hata et al., 2004).

Another important parameter associated with the precursor is its feed rate. At very high temperatures where the precursor is near self-dissociation, the reaction rate gets limited by the precursor feed rate in the system. High feed rates can increase the rate of growth but just like high temperatures can also result in more of carbon soot formation and hence catalyst poisoning. Precursor feed rate is also coupled with the size of catalytic nanoparticles. For example in a study by Cheung (Cheung et al., 2002), it is shown that different carbon species can be produced with the same diameter catalyst nanoparticles using different carbon carrier gas flow rates. At higher flow rates, larger diameter nanoparticles will grow more since the smaller ones will quickly get poisoned and vice versa for lower flow rates (Chandra, 2009).

#### 2.2.3.4 Catalyst nanoparticle

Catalysts are transitional metal nanoparticles obtained through various sources, such as metal salts, evaporated metal films, etc. Two factors that define a catalyst particle are its size and composition. Nanoparticles of Fe, Co, Mo, Ni, Cu, Au, etc. (Moisala et al., 2003) have been tried as catalyst either in pure metallic form or as alloys. These transition metal nanoparticles have common advantages of high

carbon solubility, carbon diffusion rates and high melting temperatures. Various approaches are used to obtain the nanoparticles; some of the most common ones use metal salts (nitrates, sulfates and chlorides), where stable nanoparticles complexes are formed in a suitable solvent. Evaporated film of metal can also produce uniform nanoparticles upon controlled annealing treatments. Organic carriers have also been used in the formation of very small size nano clusters. Sizes of these particles are reported to be anywhere from 1 nm to 15 nm. There are strong indications of dependence of CNTs diameter on the catalyst particles size; hence narrowing the catalyst diameter can help in a controlled diameter nanotubes growth. Also of tremendous importance is the method used to apply the nanoparticles on the growth substrate, which affects their resultant morphology significantly (Chandra, 2009).

#### 2.2.3.5 Role of hydrogen in the synthesis of carbon nanotubes

Hydrogen has been found (Bladh et al., 2000; Nerushev et al., 2001) being able to efficiently promote the synthesis CNTs. It has been reported by Nerushev (Nerushev et al., 2001) that, in a thermal CVD reaction which was engaged 20 minutes after the hydrogen supply had been cut off, the suspensions of hydrogen result in thickening sidewalls of MWNTs and unwanted products of carbon fibers with diameters of more than 1 μm. The "sidewall thickening effect" can be attributed to either an increasing concentration of carbon species in the reaction chamber or an accelerated precipitation rate of carbon species. These observations are associated to the disproportionation reaction of hydrocarbon, for example, the decomposition of $C_xH_y$.

$$C_xH_y \rightarrow xC + (y/2)\ H_2$$

In a hydrogen-participated synthesis of CNTs, hydrogen shifts the reaction above to the left. Thus one of the roles which hydrogen plays in the synthesis of MWNTs might be limiting the release of carbon species from the hydrocarbon. A total cut-off of hydrogen results in a rapid rate of hydrocarbon dissociation, therefore much more dense supply of carbon species leads to the formation of unwanted product. Hydrogen also proposed another role as reducing the metal catalyst particles so that the catalytic activity of these catalysts is maintained in the synthesis of CNTs (Nerushev et al., 2001; Zhang et al., 2005).

#### 2.2.3.6 Temperature

The ideal temperature for CNTs growth depends on several factors, mainly carbon feedstock, catalyst, and the type of CNTs desired (single or multi walled). Carbon nanotubes are typically grown in a temperature range from 550 $^{o}$C to 1,000 $^{o}$C (Moisala et al., 2003). The temperature also plays an important role in the pre-growth treatment of the catalyst. Small catalytic nanoparticles readily oxidize under ambient conditions therefore, to bring them back to native state a controlled reduction step is required at moderate temperatures (Huang et al., 2003).

## 2.3 Characterization of carbon nanotubes

In order to comprehend their basic physical and chemical properties, the complete and correct characterization of CNTs is crucial. There are many techniques that are available to characterize CNTs for example Raman spectroscopy,

thermogravimetric analysis (TGA), X-ray diffraction (XRD) and electron microscopy (SEM, TEM). These techniques and the relevant information that can be obtained for CNTs are discussed in this chapter.

### 2.3.1 Raman Spectroscopy

A CNT consists of a graphene sheet rolled in a tube, vibrational modes of CNT are derived from those of graphene by applying boundary conditions along the circumference (Burghard, 2005). The first paper on Raman scattering in single wall carbon nanotubes was published in 1997 by Rao (Rao et al., 1997). A typical Raman spectrum is shown in Figure 2.15. Raman spectrum of CNTs can be divided into three main parts, the radial breathing mode (RBM), the disorder induces mode (D mode) and the high-energy mode (HEM). Each part is used to access different properties of carbon nanotubes.

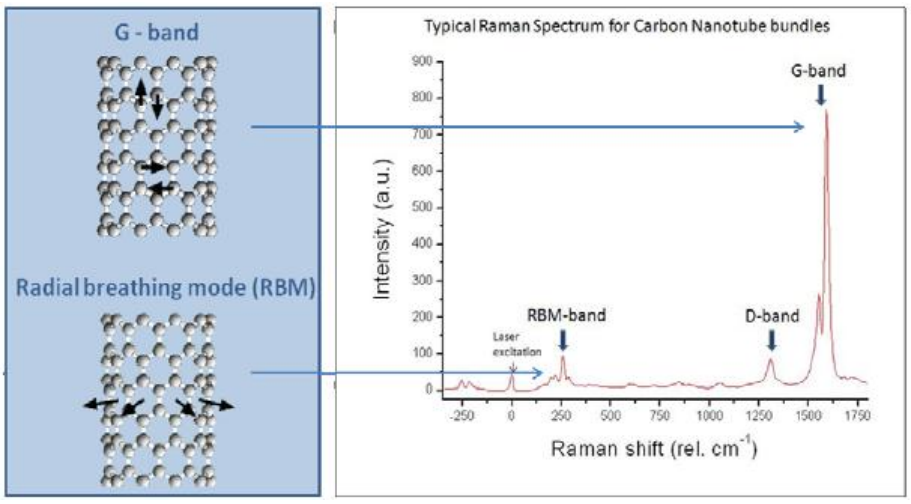


**Figure 2.15** Raman spectra showing the most characteristic feature of CNTs with corresponding atomic vibration (Müller, 2009)

There are two dominant Raman signatures of CNTs in these Raman spectra that distinguish a SWNT from other forms of carbon. First, the low-frequency feature, usually in the range 100 to 300 $cm^{-1}$, is arising from scattering by the radial breathing modes (RBM) which correspond to symmetric in-phase displacements of all the carbon atoms in the SWNT in the radial direction. Second, the double-peak structure (around 1,500 to 1,600 $cm^{-1}$) is associated with the axial (lower peak) and tangential (highest peak) vibrational modes and is related to the Raman-allowed feature appearing in Raman spectra for graphite, called as G band. Neither the RBM nor the multi-component G band features are observed in any other sp2 bonded carbon material. Typically, $sp^2$ bonded carbon materials show the characteristic single G band (Lorentzian shape) Raman peak at about 1,582 $cm^{-1}$. These two first-order Raman features (the RBM and the multi G band) are the spectral signatures of SWNT and have been used to characterize CNTs samples from their around the circumference of a tube is proportional to the nanotube diameter, it is expected that the frequency of the RBM mode ($\omega_{RBM}$) will depend on the inverse tube diameter, as observed experimentally (O'Connell, 2006; Dresselhaus et al., 2004; Brukh and Mitra, 2006). The RBM from MWNTs is only observed when they have very small diameter inner tube (below 3 nm). The G band in MWNTs is both small in intensity and smeared out due to the effect of diameter distribution within the individual MWNTs, and because of the variation between different tubes in an ensemble of MWNTs in typical experimental sample (Costa et al., 2008). The peak appears at the frequency between 1,330 $cm^{-1}$ and 1,360 $cm^{-1}$, called as D band, is known as the disordered or defect mode. The D band is present in all carbon allotropes, including $sp^2$ and $sp^3$ amorphous carbon. In CNTs, this band is activated from the $1^{st}$-order

scattering process of $sp^2$ carbons by the presence of in-plane substitutional hetero-atoms, vacancies, grain boundaries, or other defects. When observed in MWNTs the D band has been generally viewed as a defect in the tubes. The quality of a sample has often been evaluated using the D/G band intensities. For high-quality samples without defects and amorphous carbon, the D/G ratio is often less than 2 % (Müller, 2009).

### 2.3.2. Thermogravimetric Analysis

In case of the carbon nanotubes, TGA analysis is performed in an oxidative atmosphere (air or oxygen) with a linear temperature ramp. The maximum temperature is selected so that the specimen weight is stable at the end of the experiment, implying that all chemical reactions are completed (i.e., all of the carbon is burnt off leaving behind metal oxides). The weight change in an air atmosphere is a superposition of the weight loss due to oxidation of carbon into gaseous carbon dioxide and the weight gain due to oxidation of residual metal catalyst into solid oxides. The following information can be obtained from TGA.

***Residual mass ($M_{res}$)***: the ash content or the mass of residual metal oxide.

***Oxidation temperature ($T_o$)***: the temperature at the maximum in the weight loss rate ($dm/dT_{max}$).

***The weight loss onset temperature ($T_{onset}$)***: the temperature when oxidation just begins. Gradual onset is believed to be due to nanotubes being contaminated with amorphous carbon and other types of carbonaceous impurities that oxidize at temperatures (~400°C) lower than that of nanotubes. Weight loss due to carbon oxidation is often superimposed on the weight increase due to catalyst oxidation at low temperatures and in some cases this leads to an upward swing of the TGA curve

prior to the bulk of the weight loss. TGA measurement of "as-produced" nanotube material in air usually produces only one peak in the dm/dT curve, as raw nanotubes oxidize rapidly in an oxygen-rich environment. The oxidation temperature $T_o$ provides a measure of the thermal stability of nanotubes in air and it depends on a number of parameters like diameter of the tube (smaller diameter nanotubes are believed to oxidize at lower temperature due to a higher curvature strain), defects in nanotube walls (can lower the thermal stability), metal particles present in the nanotube specimens (amount of metal impurity in the sample influences the thermal stability). Thermal stability is a good measure of the overall quality of a given nanotube sample. Higher oxidation temperature is always associated with purer, less defective samples (Arepalli et al., 2004). Typical heating rates employed in TGA measurements of carbon nanotube specimens are in the 5 to 20 $°C•min^{-1}$ range (Ahmed, 2009).

### 2.3.3 X-ray diffraction

This characterization method is not sample destructive and is used to obtain some information on the interlayer spacing, the structural strain and the impurities. However, carbon nanotubes have multiple orientations compared to the X-ray incident beam. Diameters and chiralities distribution are also observed as well as various number of layers for MWNTs. This leads to a statistical characterization of carbon nanotubes. Due to their intrinsic nature, the main features of X-ray diffraction pattern of CNTs are close to those of graphite (Figure 2.16): (i) a graphite-like peak (0 0 2) is present and measurements of interlayer spacing can be obtained from its position using the Bragg law, (ii) a family of (h k 0) peaks due to the honeycomb

lattice of single grapheme sheet. Consequently, the X-ray diffraction profile is not useful to differentiate microstructural details between the CNTs and the graphite structure (Zhu et al., 2003) but can help to determinate the sample purity (catalyst, functional groups). Using the (0 0 2) peaks position, the interlayer spacing is often found to be larger than in highly ordered pyrolytic graphite (HOPG) and close to the value determined in turbostratic graphite (Lambin et al., 2002; Saito et al., 1993). The peak position shifted from 26.5° for graphite to ~26° in 2θ for SWNT. Moreover, the line shape of the (0 0 2) peaks is weakened and is broadened on its low diffraction angle part compared to graphite ones. The asymmetry is caused by the presence of different crystalline species. Indeed, at least two structures are generally present and are difficult to separate: the pure graphite particles consisting of a stack of graphene sheet, and the wrapped graphitic plane constituting a carbon nanotube.

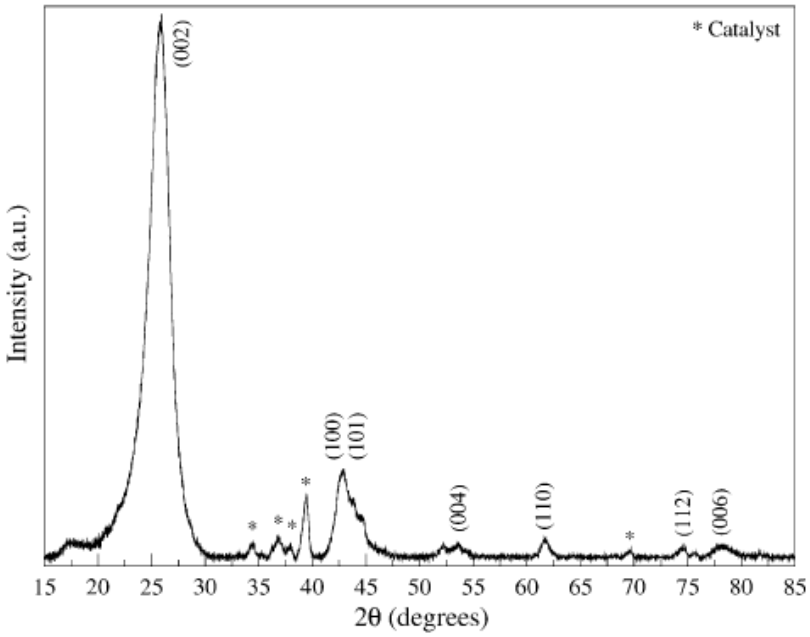


**Figure 2.16** XRD pattern of MWNTs synthesized by CVD using Co and Mo catalysts (Belin and Epron, 2005)

On the other hand, the decrease of the interlayer spacing with the increase of diameter of the shells (Kiang et al., 1998) and the inner diameter distribution (Lambin et al., 2002) modify also the shape of the (0 0 2) peaks. The intensity and width of the (0 0 2) peaks are related to the number of layers, to the variations of interlayer spacing, to the lattice distortions (Reznik et al., 1995; Burian et al., 1999) and to the carbon nanotubes orientation compared to the X-ray incident beam (Cao et al., 2001). The (h k 0) peaks present an asymmetric shape due to the curvature of the nanotubes (Lambin et al., 2002) and the (h k l) reflections only appear in X-ray diffraction patterns with a regular stacking of layers (as with flat graphitic layers in polygonized tubes and with residual carbon particles) (Liu and Cowley, 1994; Bernaerts et al., 1998). A mean diameter of CNTs can be calculated through the use of the Debye–Scherrer relation on the (0 0 2) peak. There is contributions from both the nanotubes and residual graphite in the (0 0 2) peak so the values are calculated from peak decomposition using pseudo-Voigt profiles.

### 2.3.4 Electronic microscopy

Electron Microscopes use a beam of highly energetic electrons to examine objects on a very fine scale. Electron microscopy techniques enable us to see and study carbon nanotubes structures in great detail. The instrument development was driven primarily by the well-known limitations of the light microscope. In electron microscopy a beam of energetic electrons is incident on the sample. As a result of interaction of this beam different types of electrons and radiations are emitted from the sample and the substrate which are detected and used to construct the image of the

sample. There are two well-known types of electron microscopes: scanning electron microscope (SEM) and transmission electron microscopes (TEM).

#### 2.3.4.1 Scanning Electron Microscopy

In order to observe nano size objects like CNTs, the use of an SEM is necessary to overcome the limited angular resolution of optical microscopes (Newbury and Williams, 2000). Both nanotubes powder samples as well as individual tubes on a bulk substrate (e.g., silicon wafer) can be observed by SEM. A fine electron probe is scanned across the sample surface while recording the current of the electrons emitted from the sample surface (called secondary electrons) due to interactions of incident high energy electron beam with the sample surface. The image is the intensity of the emitted electron current versus beam location at the sample. An image can be formed by the secondary electrons emitted from the sample surface as well as by the backscattered primary electrons.

#### 2.3.4.2 Transmission Electron Microscopy

Although SEM can be useful in imaging the tubular one-dimensional (1-D) structure of the MWNTs, there is another method of electron microscopy that can be much more helpful in the structural studies of carbon nanotubes. This method is transmission electron microscopy (TEM), and it is a powerful technique that is used to determine the number of walls in MWNTs (Meyyappan, 2005; Iijima, 1991) or image the isolated SWNT. It allows for the measurement of the tube diameters as well as investigation of structural defects in carbon nanotubes.

In order to characterize CNTs by TEM, an image analysis methodology was developed. Kiang (Kiang et al., 1998) studied the interlayer spacing of MWNTs by using high resolution TEM images. The interlayer spacing is found to range from 0.34 to 0.39 nm varying with nanotubes diameter (Figure 2.17 a–c). However, these values are greater than the graphite interplanar distance (0.335 nm) (Charlier et al., 1999).

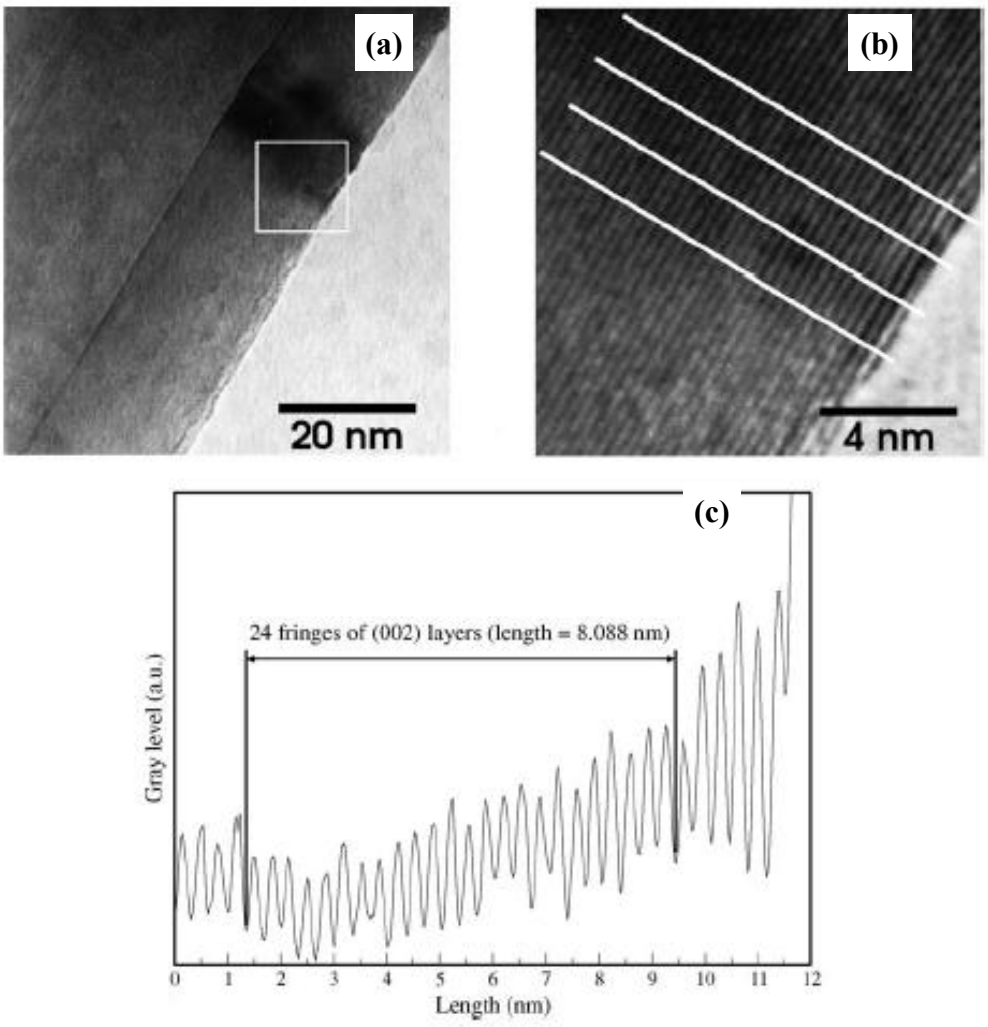


**Figure 2.17** (a) TEM image of MWNTs (diameter of about 65 nm), (b) enlargement of indicated area reveals contrasts of the walls and (c) mean profile of the intensity levels of the walls showing the fringes of the (0 0 2) layers used in the determination of the interlayer spacing along white lines (Belin and Epron, 2005).

This increase in interlayer spacing is probably due to the curvature of the graphene sheets which is modified by the tube radius. This curvature leads to an increase of the repulsive force and the size effect is more intense in the small diameter (below 10 nm). In MWNTs, dopant atoms or molecules could be introduced between adjacent nanotubes as already observed with intercalation compounds in graphite (Dresselhaus et al., 2001). This leads to an increase of the interlayer spacing too.

## 2.4 LITERATURE REVIEWS

### 2.4.1 Experimental comparison of catalysts for CNTs growth

The choice of catalyst is perhaps the most significant variable in CNTs synthesis, determining the rate of carbon deposition, yield, selectivity, and quality of products. Metal catalysts used for CNTs formation are most often transition metals, in particular iron, cobalt and nickel. Many papers available in the literature about growth of CNTs on iron, cobalt or nickel based catalysts report growth of MWNTs.

*Ivanov et al. (1994)* observed a better graphitization on cobalt than on iron, but on nickel, most of the filaments were amorphous. Straight and coiled carbon tubules were obtained with inner and outer diameter of 3–7 and 15–20 nm, respectively, and up to 300 μm in length.

*Fonseca et al. (1996)* summarized the results that iron was more active than cobalt. However, CNTs produced from cobalt showed the better quality in term of graphitization and structure.

*Hernadi et al. (2000)* tested iron and cobalt-based catalysts with different hydrocarbons on different supports and observed that iron presents the highest activity in the decomposition of different unsaturated compounds. Acetylenes, olefins and molecules that could be decomposed to generate olefins on heating in the presence of the catalyst were good carbon sources for nanotubes formation.

*Klinke et al. (2001)* tested iron, cobalt and nickel-based catalyst on silica for CNTs growth with acetylene. They compare the growth of the carbon nanostructures in the temperature range between 580 ºC and 1,000 ºC. With their experimental set-up, the catalyst solutions of cobalt and nickel were found to be less efficient than the one of iron. An optimal production of MWNTs was observed at temperatures between 650 ºC and 720 ºC with the iron solution as catalyst. Iron produced the highest density of carbon structures at any considered temperature as shown in Figure 2.18.

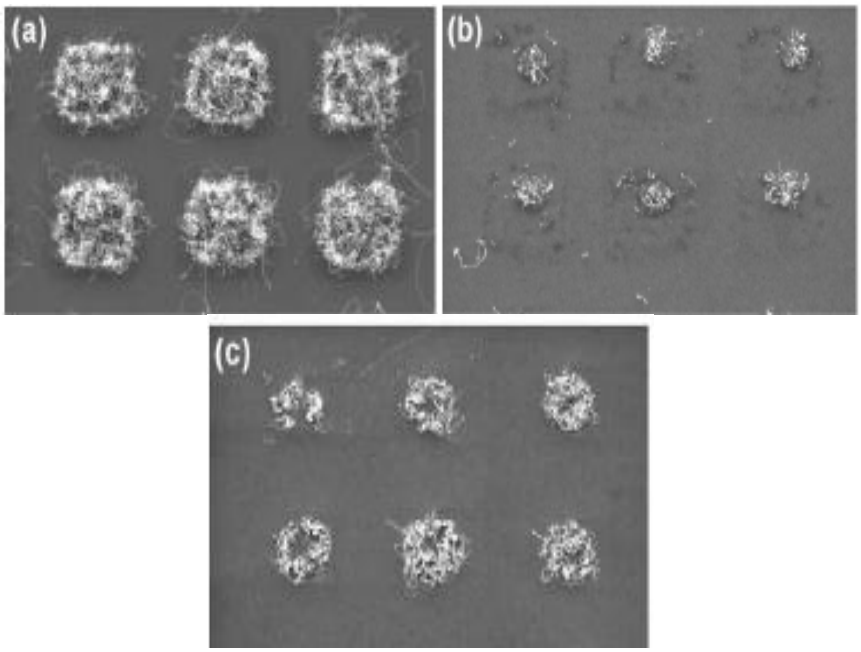


**Figure 2.18** SEM images demonstrating the effect of catalyst on MWNTs growth at 720 $^{o}$C using $Si/SiO_2$ as support; (a) Fe, (b) Ni and (c) Co (Klinke et al., 2001)

*Corrias et al. (2005)* studied on the effect of support on MWNTs synthesis over $CoFe_2O_4$ using ethylene as precursor. They emphasized that the support played an important role on MWNTs synthesis. In their work, MWNTs successfully synthesized over 10% w/w $CoFe_2O_4/Al_2O_3$ whereas unsupported $CoFe_2O_4$ produced mainly graphite crystals (GraC).

*Philippe et al. (2007)* summarized their experiment on the synthesis of CNTs and GNFs using ethylene in FB-CVD system. They observed that GNFs could be produced using $Ni/Al_2O_3$ catalyst while $Fe/Al_2O_3$ catalyst gave MWNTs as main product. They also reported the explosion of catalyst grains due to the growth of GNFs and MWNTs which could benefit the process due to the opening of internal pores.

*Yeoh et al. (2009)* investigated the synthesis of MWNTs over Co-Mo/MgO supported catalyst via CCVD of methane at flow rate of 300 $mL \bullet min^{-1}$ ($CH_4$:$N_2$ 150:150), 800 $^oC$ and 30 minutes of run duration. They reported that the Co-Mo co-catalyst (5:20:25 wt% Co:Mo:MgO) could produce MWNTs with a narrow size distribution (6.2 ± 0.5 nm). The selectivity of as-prepared MWNTs was higher than 90%, and 99% after purified.

*Zhao et al. (2010)* studied on MWNTs synthesis from acetylene by CCVD over Fe/zeolite NaX catalyst at 700 $^oC$, $C_2H_2$:$N_2$ 10:200 $mL \bullet min^{-1}$, 100 mg of catalyst and 60 minutes of run duration. They found that the $\alpha$-$Fe_2O_3$ catalyst produced MWNTs with quite small inner and outer diameters, 3.8-5.0 nm and 6.3-8.8 nm,

respectively, which were close to the diameters of catalyst particles. They also observed the formation of MWNTs via tip growth model.

*Zhao et al. (2011)* compared the activity of Ni-loaded and Ni-substituted MCM-41 on MWNTs synthesis by CCVD of ethanol. The results confirmed that both catalysts were active for MWNTs synthesis at 700 $^{o}$C. However, as extracted from TEM and Raman spectra, Ni-substituted MCM-41 provided more uniform tubes diameter and better quality MWNTs than Ni-loaded MCM-41.

*Sivakumar et al (2011)* studied on CNTs synthesis over Fe and Ni supported activated carbon by methane CVD. They found that $CH_4/N_2$ ratio of 1:2 could produce more amounts of CNTs than $CH_4/N_2$ ratio of 1:1. The highest $CH_4$ conversions could be achieved at 750 $^{o}$C (98% and 42% over Fe and Ni catalyst, respectively) while the highest MWNTs yield was obtained at 850 $^{o}$C. In terms of quality, TGA results showed that Ni catalyst provided MWNTs with higher thermal stability and larger outer diameter than those obtained from Fe catalyst.

*Yang et al. (2012)* studied on MWNTs synthesis over Cu supported Al powder catalyst by CCVD of ethanol at 500-650 $^{o}$C. They claimed that Cu catalyst could act as an active metal for MWNTs synthesis even it shows nearly zero carbon solubility. Nevertheless, amorphous carbon and carbon filaments could be obtained as by-products at process temperature of 700 $^{o}$C due to the sintering of Cu nanoparticles. They concluded that the interaction between Al support and Cu catalyst played an important role as it could decrease the free energy and improve the electron density of the catalyst.

2.4.2 Experimental comparison of growing parameters

The main parameters for CNTs growth in FB-CCVD are the hydrocarbon, catalyst, and growth conditions. General experience is that low-temperature CVD (600 to 900 ºC) yields MWNTs, whereas a higher temperature reaction favors SWNT growth, indicating that SWNT has a higher formation energy this may be due to its small diameter, which results in high curvature and high strain energy. This could explain why MWNTs are easier to grow from most hydrocarbons than SWNT, which can only be grown from selected hydrocarbons that have a reasonable stability in the high temperature range.

*Hernadi et al. (2001)* reported that common efficient precursors of MWNTs (e.g. acetylene, ethylene, etc.) were unstable at higher temperatures, lead to directly pyrolysis of hydrocarbon, resulting in the deposition of large amounts of non-tubular carbon compounds. Moreover, encapsulated metal particles could be found in the high temperature range.

*Venegoni et al. (2002)* studied on the growth of MWNTs over $Fe/SiO_2$ catalyst using ethylene as carbon source. They reported the formation of encapsulated particles at the temperature above 850 $^{o}$C. Moreover, the formation of encapsulated particles also occurred in case of high metal loading (5%w/w $Fe/SiO_2$). They concluded that the formation of encapsulated particles was possible due to the sintering of supported catalyst.

*Wang et al. (2004)* found that the kinetic of MWNTs formation is positive order dependent on reactant partial pressure. They also found that the average length of the carbon nanotubes grown at the pressure of 15 Torr was larger than that at the pressure of 30 Torr. But, it was difficult to grow the carbon nanotubes when the pressure is 5 Torr. These indicated that the pressure greatly influences on the growth of carbon nanotubes.

*Morançais et al. (2007)* summarized the results that the carbon yield increased when the total gas flow rate decreased due to increasing of residence time. In addition, they reported that increasing of total pressure led to gas diffusivity decrease so, MWNTs formation rate decreased.

*Pirard et al. (2007)* studied on the kinetic of MWNTs synthesis by the CCVD method, the catalyst used was an iron-cobalt catalyst. They found that hydrogen partial order was equal to zero, ethylene partial order was between 0 and 1 and increased from 600 ºC to 700 ºC. Activation energy was found to be 135 $kJ \cdot mol^{-1}$, adsorption enthalpy was -120 $kJ \cdot mol^{-1}$ and adsorption entropy is -130 $J \cdot mol^{-1} \cdot K^{-1}$.

*Zhu et al. (2007)* came to the same conclusion as Wang, the growth rate increased linearly with ethylene molar fraction, the reaction was first order with an activation energy of 201.2 $kJ \cdot mol^{-1}$.

*Philippe et al. (2009)* reported their experiment on kinetic of CNTs synthesis by FB-CVD over $Fe/Al_2O_3$ using ethylene as active gas. They detected gaseous components and reported that ethane could be decomposed and produced MWNTs at

temperature above 650 $^{o}$C whereas methane did not react in temperature range 550 $^{o}$C to 750 $^{o}$C. The apparent partial orders of reaction for ethylene, hydrogen, and iron were found to be 0.75, 0, and 0.28, respectively. They also found the discrepancy of activation energy which related to the change of rate determining step. They explained that during the first 10 minutes of reaction, nucleation was probably the dominant mechanism for MWNTs formation (Ea 29 kJ•mol$^{-1}$) after that, nucleation slowed down and growth probably became the main mechanism of MWNTs formation (Ea 120 kJ•mol$^{-1}$).

*Danafar et al. (2011)* investigated the effect of size of alumina support on the performance of FB-CVD process for CNTs synthesis. By using six different alumina particle sizes, the Fe/Co (2.5:2.5 wt%) supported on 10-20 μm alumina powder yield highest carbon deposition with almost 100% CNTs selectivity. They explained their results by the excellent heat and mass transfer which related to low diffusion resistivity, good fluidization behavior and high surface area of fine particles.

*Paul and Samdarshi (2011)* reported the possibility of CNTs synthesis from renewable source (coconut oil) over Fe catalyst by CVD. A reasonable yield of MWNTs with outer diameter of approximately 80-90 nm was obtained. However, Raman spectra revealed that the as-prepared MWNTs were not well graphitized and contained defects in there structure.

The synthesis conditions and results from several studies are summarized in Table 2.4.

**Table 2.4** Summary of parameters for MWNTs synthesis using CVD from selected literatures

| Reference | T( $^{o}$C) | H.C. (% mol) | $H_2$/H.C. | Duration (min) | Activity | Selectivity | Quality | Conclusion |
|---|---|---|---|---|---|---|---|---|
| Tran et al. (2007) | 700 | 30 | 0 | 15 | Good | High | Good | - |
| Bronikowski (2006) | 550-800 | 50-100 | 0-1.0 | 15 | - | - | | optimum T 725$^{o}$C, $H_2$/H.C. 0.25 |
| Ferlauto et al. (2006) | 700 | 0.7-2.3 | 14-50 | 30 | - | High | Good | ~65 $g_{MWNTs} \bullet g_{cat}^{-1}$ |
| McCaldin et al. (2006) | 500-700 | 5-100 | 0-19 | 120 | - | - | | optimum T 700 $^{o}$C, $H_2$/H.C. 4 (20% mol H.C.) |
| Ciambelli et al. (2005) | 600-700 | 10 | 0 | 10-60 | - | 70% | | optimum T 700 $^{o}$C, 60 min |
| Corrias et al. (2005) | 550-750 | 18 | 2.6 | N/A | - | Mainly MWNTs | | mainly GraC in case of substrate free |
| Kuo et al. (2005) | 750 | 1.7-7.5 | 1.3-2.6 | 15 | - | - | | 26.7 $\mu m \bullet min^{-1}$ $H_2$/H.C. 2.6 (7.5% mol H.C.) |
| Xu and Zhu (2004) | 650 | 9.8 | 9 | 40 | - | >95% | Good | - |
| Wang et al. (2002) | 500-700 | 83-100 | 0.05-0.1 | 30-60 | Good | 70-80% | | - |
| Hernadi et al. (2000) | 700-800 | 10 | 0 | 30 | Good | High | Good | T optimum 750 $^{o}$C |

# CHAPTER III

# EXPERIMENTAL

To study catalytic growth carbon nanotubes, FB-CVD experimental was established to allow the continuous analysis of gaseous streams containing the carbon source, permitted to perform carbon mass balance, to evaluate hydrocarbons conversion, the presence of by-products and catalysts performances. In this chapter, material and equipment used in this dissertation were descripted in part I and II, respectively. Experiment procedure consists three main parts; fluidized-bed chemical vapor deposition process to synthesize MWNTs, Catalyst and synthesized product characterization and kinetic evaluation of MWNTs synthesis by on-line analysis were described in part III.

## 3.1 Materials

### 3.1.1 Catalyst

The cobalt impregnated gamma-alumina catalyst used in this research was provided by LCC (Laboratoire de Chimie de Coordination/ENSIACET/INPT). It was calcinated at 450 °C for 6 hours by air at a flow rate of 400 standard $cm^3 \bullet min^{-1}$.

3.1.2 Gases

- Electronic grade (99.99%) $C_2H_4$ from Air Liquide
- Electronic grade (99.999%) $H_2$ from Air Liquide
- Electronic grade (99.999%) $N_2$ from Air Liquide

## 3.2 Equipment and apparatus set-up

3.2.1 Equipment

- Mass flow controller
- Ball valve (Stainless steel) from Swagelok
- Electric furnace
- Corrugated stainless steel packing media
- Gas distributor (double layers stainless steel grid : 40μm holes)
- Thermocouple
- Pressure sensor
- Bag filter
- Micro pump (LFS-113D Gilian)
- Gas chromatograph (GC Clarus 500Perkin Elmer)
- Control panel
- Personal computer
- Stainless steel FB-CVD reactor (Cylindrical zone : 5 cm inner diameter, 1 m height, Expansion zone : 10 cm inner diameter)

3.2.2 Apparatus set-up

The experimental set-up for MWNTs synthesis consists of three sections: feed section, reaction section and analysis section.

The feed section allows the feeding of the carbon source, $H_2$ and $N_2$ as the fluidizing gas. For each gas, a mass flow controller was used in order to control a flow rate. For the reaction section of FB-CVD reactor for MWNTs production is made of 304L stainless steel. It contains a cylindrical zone of 5 cm inner diameter, 1 m height and an expansion zone of 10 cm inner diameter to allow particles to drop back into the bed. All of the connections and valves are made of stainless steel from Swagelok. The gas distributor is a double layers stainless steel grid with 40 μm holes. A corrugated stainless steel packing media was added below the gas distributor to ensure the excellent uniformity of fluidizing gas temperature. The bed temperature was controlled by a temperature control system composed of electric furnaces, PID temperature controllers and two thermocouples located at the central axis of reactor, 5 cm and 40 cm above the distributor. A pressure sensor was also installed in order to measure the pressure drop across bed and total pressure in reactor. Fine particles or soot that could be generated as by-products during experiments were entrapped by a bag filter.

Finally, analysis section, a small portion of treated effluent was sampling via a micro pump (LFS-113D Gilian) and was examined by a gas chromatograph (GC Clarus 500 Perkin Elmer) every 10 minutes in order to investigate its composition. It should be noted that all data measured by the apparatus described above were

continually recorded by DASYLab software. The schematic of experimental setup is represented in Figure 3.1 respectively.

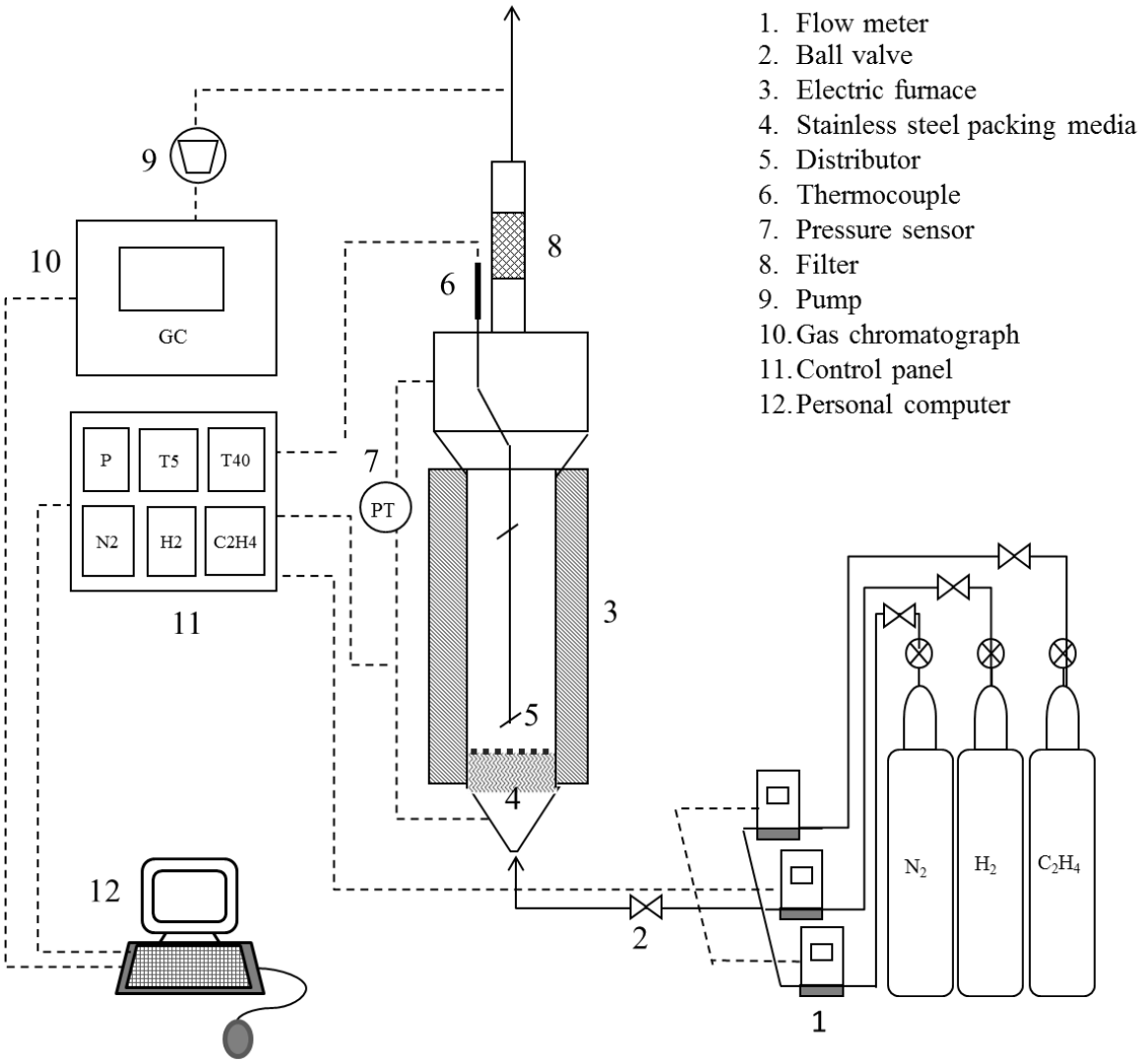


Figure 3.1 The schematic of the experimental setup

## 3.3 Experimental procedure

### 3.3.1 Carbon nanotubes synthesis

The experimental conditions were divided into two parts. The first part was the study of the effect of temperature on MWNTs synthesis. The second part was the study of the effect of ethylene molar fraction on MWNTs synthesis. Specific experimental condition for each part was described below

3.3.1.1 The effect of temperature on MWNTs synthesis

- Temperature in the range of 600 $^{o}$C to 700 $^{o}$C
- The amount of catalyst; 20 g and 60 g
- Flow rate of $C_2H_4$:$H_2$:$N_2$; 400:200:200 standard $cm^3 \bullet min^{-1}$
- Time on stream; 60 min
- Total pressure; 1 atm

3.3.1.2 The effect of $C_2H_4$ molar fraction on MWNTs synthesis

- Flow rate of $C_2H_4$:$H_2$:$N_2$;
  - 300:200:300 standard $cm^3 \bullet min^{-1}$
  - 400:200:200 standard $cm^3 \bullet min^{-1}$
  - 500:200:100 standard $cm^3 \bullet min^{-1}$
- Temperature; 600 $^{o}$C
- The amount of catalyst; 20 g
- Time on stream; 60 min
- Total pressure; 1 atm

Electronic grade ethylene, hydrogen and nitrogen (Air liquide) were fed into a reactor via mass flow controllers as fluidizing gas. In this study, the total volumetric

flow rate of fluidizing gas was fixed at 800 standard $cm^3 \bullet min^{-1}$, corresponding to the initial fluidization ratio $U/U_{mf}$ at 700 $^oC$ of about 8. Details of the general procedure which was applied to all experiments are as follows. Initially, a certain amount of calcined catalyst powders was loaded into the reactor. The bed was then concurrently fluidized and heated under flow of equimolar nitrogen and hydrogen. After reaching 450 $^oC$, the bed was maintained at this temperature for 1 hour for reduction of cobalt oxide. After that, the temperature was raised once again under flow of pure nitrogen until the desired reaction temperature was attained. As soon as the temperature was steady, the flow rate of nitrogen was decreased whereas ethylene and hydrogen were introduced simultaneously into the reactor at a pre-calculated flow rate. Finally, the bed was cooled down to ambient temperature under nitrogen atmosphere. After completion of the experiment, solid product was drained into a plastic bag and was characterized.

### 3.3.2 Catalyst and synthesized product characterization

#### 3.3.2.1 Characterization of catalyst

To evaluate physicochemical properties of catalyst, the analysis of the following method were done as summarized in Table 3.1.

- *The specific surface area of cobalt supported on alumina catalyst* was determined by Brunauer–Emmett–Teller (BET) equation with $N_2$ adsorption/ desorption at -196 °C (Micromeritics ASAP 2010).
- *Grain density '$\rho_g$' ($g \bullet cm^{-1}$)* was investigated using a water pycnometer, capacity of 50 $cm^3$, at 15 $^oC$.

- *Untapped bulk density '$\rho_b$' ($g \bullet cm^{-1}$)*, the bed appearance density measurement procedure of ASTM D6393-99 was followed using a Hosokawa PT-E powder tester.
- *Minimum fluidization velocity '$U_{mf}$' ($cm \bullet s^{-1}$)*, determined from the relation of decreasing gas velocity to bed pressure drop, was estimated in the previously mentioned reactor using air as fluidizing gas at ambient temperature and 700 $^{o}$C.
- *Volume weighted mean diameter of particle ($D_{[4,3]}$)*, the distribution of grain diameters was identified by a laser-granulometer (Malvern Mastersizer 2000) with dry dispersion unit (Scirocco).
- *The observation on catalyst morphology* was done using a scanning electron microscope (SEM, LEO 435) operating at 10 kV.
- *The crystalline structure of catalyst* was analyzed by X-ray diffraction (XRD) technique on a Bruker D8 Advance XRD system employing CuK$\alpha$ radiation ($\lambda$ = 1.5406 Å) with an X-ray power of 40 kV, 40 mA. The 2$\theta$ measurement started from 15$^{o}$ to 90$^{o}$ with steps of 0.0092$^{o}$ and a count time of 1 second. The particle diameters were calculated by the Debye–Scherrer equation at the X-ray line broadening of the (3 1 1) diffraction peak for $Co_3O_4$.
- *The content of cobalt on alumina powder* was measured using an inductively coupled plasma mass spectroscope (ICP-MS). The analysis was conducted by an independent analytical laboratory (Antellis) base on ISO 17294.

- *The reduction temperature of catalyst* was estimated by temperature-programmed reduction (TPR) technique using a chemisorption analyzer (Micromeritics AutoChem II 2920). The sample was pretreated in a u-shaped quartz reactor under an argon flow of 40 $cm^3$ •$min^{-1}$ at 500 °C for 1 hour and was then cooled to an ambient temperature. After that, the temperature was raised up to 900 °C at a rate of 10 °C $min^{-1}$ under a reductive atmosphere, 10%(v/v) hydrogen in argon, at a flow rate of 40 $cm^3$•$min^{-1}$. A thermal conductivity detector (TCD) was employed to determine an amount of $H_2$ uptake.

Table 3.1 Summary of catalyst characteristics and method of study

| Characteristic | Analytical technique/ Instrument |
|---|---|
| **Physical Properties** | |
| Surface area | Adsorption and desorption of $N_2$ |
| Particle size and size distribution | SEM, TEM, Laser-granulometry |
| Untapped bulk density | Powder tester (ASTM D6393-99) |
| Grain density | Water Pycnometry |
| Metal Containing | ICP-MS |
| Homogeneity Morphology/ structure, bulk | SEM, TEM |
| Morphology/structure, surface | XRD,SEM,TEM |
| **Chemical Properties** | |
| Surface reactivity, active site concentration | Chemisorptions/ Temperature program reduction (TPR) |

3.3.2.2 Characterization of synthesized product

For evaluating the effect of experimental parameters on MWNTs growing and their properties, the analysis of the following physical properties were done as summarized in Table 3.2.

- *Minimum fluidization velocity '$U_{mf}$' ($cm \bullet s^{-1}$)*, determined from the relation of decreasing gas velocity to bed pressure drop, was estimated in a glass column (5 cm ID, 1 m height) with a stainless steel sintered gas distributor and a water filled u-tube manometer using air as fluidizing gas at ambient temperature.
- *The percentage of carbon deposited in form of amorphous carbon and MWNTs* was considered by thermo-gravimetric analysis (TGA, Mettler 850e). The analysis was operated under a pure oxygen flow of 50 $ml \bullet min^{-1}$ between 30 $^{o}C$ to 1000 $^{o}C$ with a ramp rate of 10 $^{o}C \bullet min^{-1}$.
- *The observation on MWNTs' morphology* as well as the presence of any unwanted products was done using a scanning electron microscope (SEM, LEO 435) operating at 10 kV.
- *The nanoscopic observation of MWNTs* was performed using a transmission electron microscope (TEM, Philips CM-12) operating at 120 kV. Before the analysis, the samples were dispersed in ethanol by ultrasonic bath and then dropped on copper grids. The selected TEM pictures were analyzed by image processing program (ImageJ) to create histograms of MWNTs outer diameters.

- *The crystalline structure of as-prepared product* were analyzed by X-ray diffraction (XRD) technique on a Bruker D8 Advance XRD system employing CuKα radiation (λ = 1.5406 Å) with an X-ray power of 40 kV, 40 mA. The 2θ measurement started from $15^{o}$ to $90^{o}$ with steps of $0.0092^{o}$ and a count time of 1 second.
- *The quality of the as-prepared product*, in terms of the graphitic crystallinity was evaluate using a Fourier transform Raman Spectrometer (FT-Raman, Thermo Scientific DXR SmartRaman) with a 532 nm laser.

Table 3.2 Summary of synthesized product characteristics and method of study

| Characteristic | Analytical technique |
|---|---|
| Particle size and size distribution | SEM, TEM, Laser-granulometry |
| Untapped bulk density | Powder tester (ASTM D6393-99) |
| Grain density | Water Pycnometry |
| Morphology/structure/surface and crystallinity | XRD,SEM,TEM, FT-Raman |
| Thermal decomposition behavior | TG/DTA |

3.3.3 Kinetic evaluation of MWNTs synthesis by on-line analysis

Continuous analysis of gaseous streams, realized with gas chromatograph (GC Clarus 500 Perkin Elmer) every 10 minutes in order to investigate gaseous

component, permitted to perform carbon mass balance, to evaluate hydrocarbons conversion, the presence of gaseous by-products and catalysts performances.

In order to scrutinize the process efficiency, following parameters were investigated;

- *Reaction conversion 'R' (%)*, defined as the ratio between mass of ethylene converted to product and mass of ethylene input
- *Solid carbon conversion 'C' (%)*, defined as the ratio of mass of carbonaceous solid product to mass of carbon input
- *Selectivity 'S' (%)*, defined as the ratio of mass of MWNTs to mass of carbonaceous solid product, was directly deduced from TG-DTA result
- *Productivity* '$X_i$' ($g_C \bullet g_{Cata}^{-1}$), defined as the ratio between mass of carbon in form of product *i* and mass of catalyst

# CHAPTER IV

# QUANTITATIVE ANALYSIS ON MWNTS

In this Chapter, characteristic of catalyst and synthesized products were studied. There were three main parts in the investigation: part I: Catalyst characterization, part II: effect of temperature on MWNTs synthesis and part III: The effect of $C_2H_4$ molar fraction on MWNTs synthesis.

## 4.1 CATALYST CHARACTERIZATION

The XRD pattern for investigation of the crystalline phase of calcined $Co/Al_2O_3$ catalyst was given in Figure 4.1.

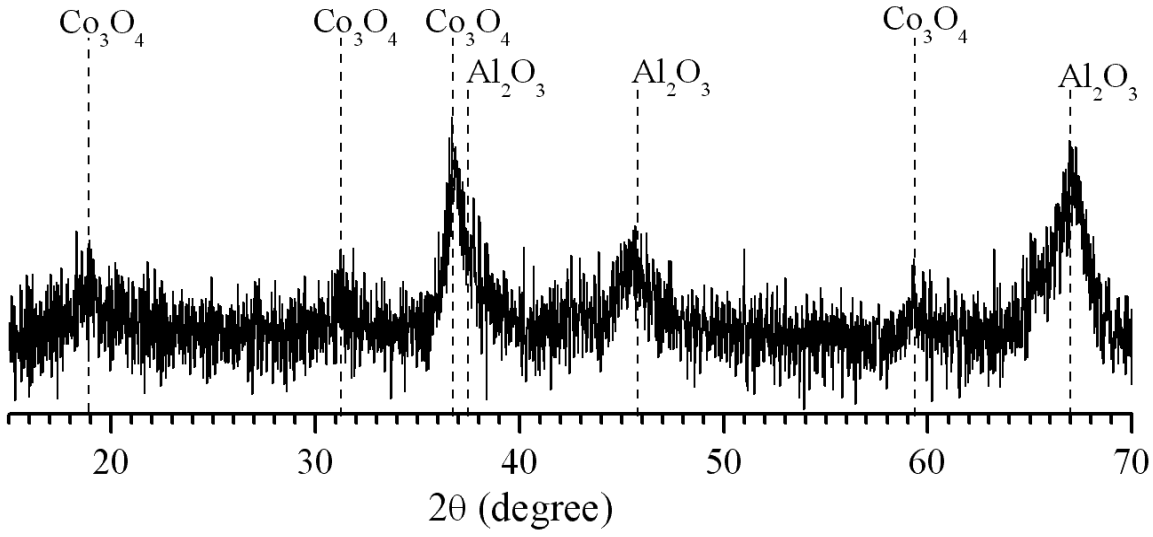


**Figure 4.1** XRD pattern of the fresh $Co/Al_2O_3$ (calcined at 450 $^oC$)

As seen in this Figure, the XRD spectra shows diffraction angles corresponding to 2 phases, namely cobalt (II,III) oxide ($Co_3O_4$) whose diffraction angles located at $2\theta = 19.0^o$ (1 1 1), $31.3^o$ (2 2 0), $36.8^o$ (3 1 1) and $59.4^o$ (5 1 1) and gamma-alumina ($\gamma$- $Al_2O_3$) whose diffraction angles located at $2\theta = 37.6^o$ (3 1 1), $45.9^o$ (4 0 0) and $67.0^o$ (4 4 0). It should be noted that in-situ reduction of catalyst were performed before MWNTs synthesis, therefore the real active phase for MWNTs growing was not $Co_3O_4$ but $Co^0$. However, the analysis of crystallite size of $Co^0$ is difficult since this specie is highly reactive and is readily oxidized when exposed to air even at ambient temperature, so in this work the analysis of crystallite size of $Co^0$ was indirectly done using the crystallite size of $Co_3O_4$. As proposed by Schanke (Schanke et al., 1995), the crystallite size (D) of $Co_3O_4$ can be converted to corresponding $Co^0$ size according to the relative molar volumes of metallic cobalt and $Co_3O_4$, as shown in equation 4.1.

$$D_{Co}{}^0 = 0.75 \times D_{Co_3O_4} \qquad (4.1)$$

The mean crystallite size of $Co_3O_4$ calculated from line broadening at half the maximum intensity (FWHM= $0.844^o$) and Bragg angle of (3 1 1) diffraction peak ($2\theta = 36.813^o$) using Debye-Scherrer equation was found to be 9.9 nm whilst the mean crystallite size of $Co^0$ estimated by equation 4.1 was approximately 7.4 nm.

The reduction property of the catalyst analyzed by $H_2$-TPR was represented in Figure 4.2. According to its Gaussian distribution, the reduction behavior of catalyst could be divided into two ranges; the first one, represented by a red dashed line, occurred in the temperature range of 330 $^o$C to 470 $^o$C with a highest $H_2$ consumption at 405 $^o$C and the second one, represented by a blue dashed line, occurred in the

temperature range of 300 $^{o}$C to 700 $^{o}$C with a highest $H_2$ consumption at 495 $^{o}$C. This result can be explained by two-steps reduction of $Co_3O_4$ to cobalt metal with CoO as an intermediate species, the first step corresponds to the reduction of $Co_3O_4$ to CoO whereas the second step corresponds to the reduction of CoO to $Co^0$ as shown in equation 4.2 and 4.3, respectively.

$$Co_3O_4 + H_2 \rightarrow 3CoO + H_2O \qquad (4.2)$$

$$3CoO + 3H_2 \rightarrow 3Co^0 + H_2O \qquad (4.3)$$

The stoichiometric $H_2$ consumption ratio of step 2 to step 1 is 3:1 which matches well with a ratio of area under peak 2 to peak 1 (2.73:1). The result of $H_2$-TPR did not show the existent of cobalt aluminate ($CoAl_2O_4$) which can be formed in case a high calcined temperature was used, this specie can be reduced at temperatures above 700 $^{o}$C (Karimi et al., 2010; Lee et al., 2009).

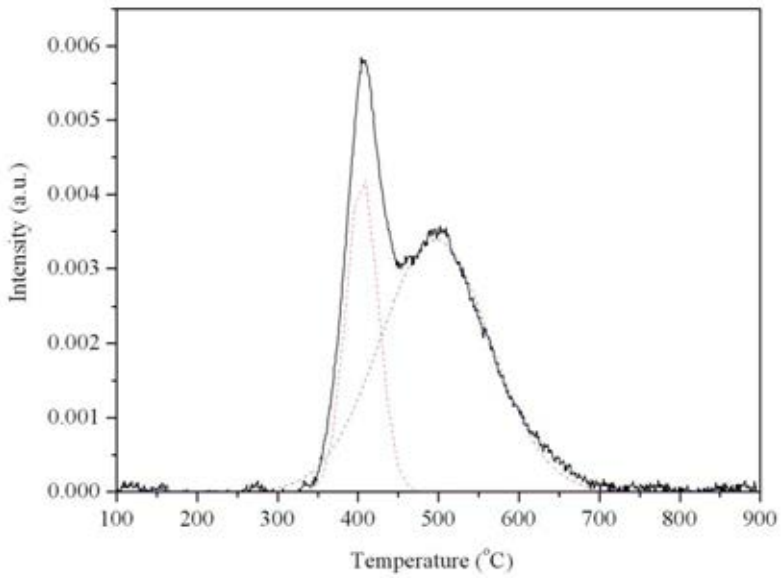


**Figure 4.2** $H_2$-TPR profile (solid line) and its Gaussian distribution (dashed line) of the fresh $Co/Al_2O_3$ (calcined at 450 $^{o}$C)

It is well known that the reduction of catalyst at high temperature lead to the sintering and loss of activity of catalyst, therefore the catalyst reduction should be done at moderate temperature. From $H_2$-TPR result, the temperature of 450 $^oC$ seemed to be sufficient to completely reduce the catalyst.

Size distribution of the fresh $Co/Al_2O_3$ particle measured by laser granulometry was demonstrated in Figure 4.3. It appeared to be nearly normal distribution with the volume weighted mean diameter ($D_{[4,3]}$) equal to 81 μm.

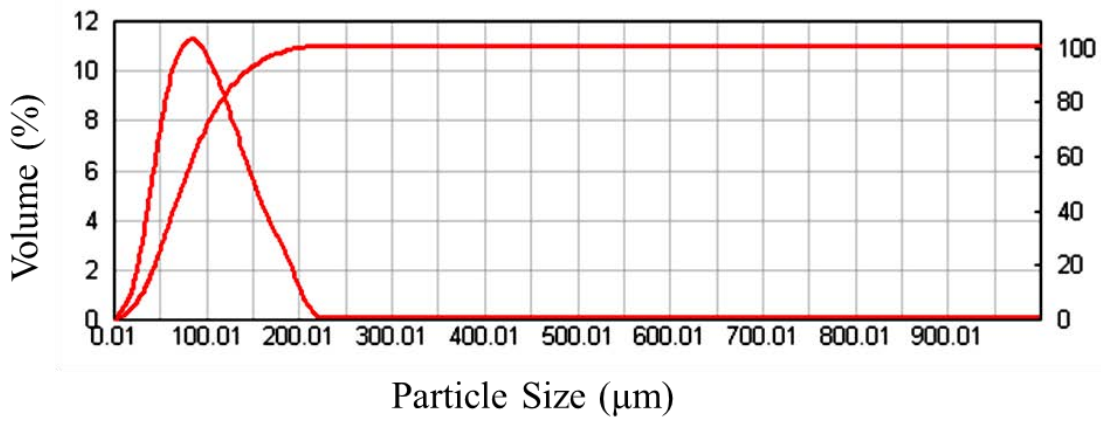


**Figure 4.3** Size distribution of the fresh $Co/Al_2O_3$ particle (calcined at 450 $^oC$)

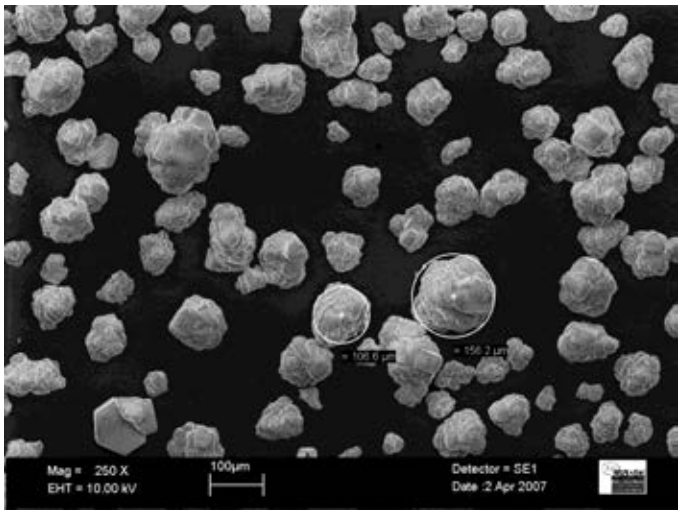


**Figure 4.4** SEM image of the fresh $Co/Al_2O_3$ (calcined at 450 $^oC$) (magnitude x250)

Figure 4.4 illustrates SEM image of the fresh $Co/Al_2O_3$. The catalyst shows a cluster of spherical alumina support. The size of catalyst estimated from SEM is quite similar to the value obtained from laser granulometer. EDX observations of selected site gives the elemental profile conform to XRD result as it contain Al, O and Co (Figure 4.5).

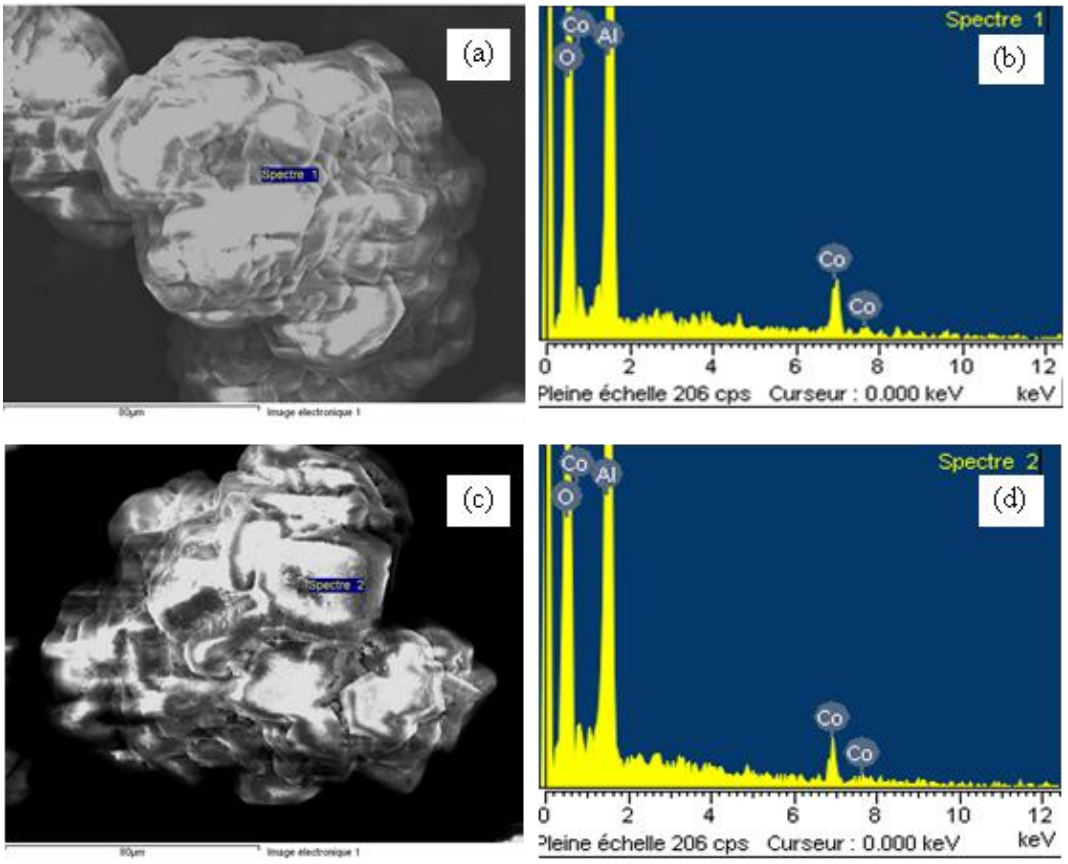


**Figure 4.5** SEM-EDX observation of the fresh $Co/Al_2O_3$; (a) and (b) site 1, (c) and (d) site 2

The average Co content measured by EDX as well as ICP spectrometry was equal to 3.3 wt%. The major characteristics of fresh catalyst namely bulk density, grain density, average $Co^0$ crystallite size, volume weighted mean diameter, surface area, minimum fluidization velocity and Co loading were summarized in Table 4.1.

**Table 4.1** Characteristic of fresh catalyst

| $\rho_b$ ($g \cdot cm^{-3}$)[a] | $\rho_g$ ($g \cdot cm^{-3}$)[b] | $D_{Co}^0$ (nm)[c] | $D_{[4,3]}$ ($\mu m$)[d] | Surface area ($m^2 \cdot g^{-1}$)[e] | $U_{mf,\ 20^oC}$ ($cm \cdot s^{-1}$) | $U_{mf,\ 700^oC}$ ($cm \cdot s^{-1}$) | % Co (wt %)[f] |
|---|---|---|---|---|---|---|---|
| 1.00 | 3.33 | 6.1 | 81.36 | 158.20 | 0.35 | 0.29 | 3.30 |

[a] Hosokawa powder tester

[b] water pycnometry

[c] equation 4.1, using XRD data of (3 1 1) $Co_3O_4$

[d] laser-granulometry

[e] $N_2$ adsorption/ desorption; Brunauer–Emmett–Teller (BET) equation

[f] ICP spectrometry

According to Geldart's particle classification, this catalyst can be classified as Geldart B group which fluidize well with vigorous bubbling action and bubbles that glow large (Kunii and Levenspiel, 1991). The Geldart's particle classification chart according to fluidization behavior was shown in Appendix C (Figure C-1).

## 4.2 THE EFFECT OF TEMPERATURE ON MWNTS SYNTHESIS

### 4.2.1 The effect of temperature on MWNTs synthesis (Weight of catalyst = 60 g)

In this part, the effect of temperature on the MWNTs production was studied in the temperature range of 600 $^oC$ to 700 $^oC$. The other parameters were kept constant as follows; duration 60 minutes, weight of catalyst 60 g, ethylene/hydrogen/nitrogen flow rate of 400/200/200 sccm, the superficial velocity of fluidizing gas corresponded to 8 $U_{mf}$. All operation parameters were summarized in Table 4.2. However, due to

the partial agglomeration of bed occurred at 700 $^{o}$C led to very high pressure drop across bed, the experiment was therefore stopped at 48 minutes of operating duration. Moreover, the bed also spitted into 2 parts namely “packed” and “fluidized” part, thus these two parts were separately sampled for characterization.

**Table 4.2** Experimental conditions for investigation of the effect of temperature on MWNTs synthesis

| Temperature ($^{o}$C) | Duration (min) | Flow rate (sccm) | | | Carbon input (g) | Weight of catalyst (g) | Initial bed height ($H_0$) (cm) | $U/U_{mf}$ |
|---|---|---|---|---|---|---|---|---|
| | | $N_2$ | $H_2$ | $C_2H_4$ | | | | |
| 600 | 60 | 200 | 200 | 400 | 24.0 | 60 | 3 | 8 |
| 650 | 60 | 200 | 200 | 400 | 24.0 | 60 | 3 | 8 |
| 675 | 60 | 200 | 200 | 400 | 24.0 | 60 | 3 | 8 |
| 700 | 48 | 200 | 200 | 400 | 19.2 | 60 | 3 | 8 |

The evaluation of MWNTs selectivity was done using TGA, as given in Figure 4.6. TG/DTA results indicate to two oxidation steps, the first corresponds to amorphous carbon that readily burn at lower temperature while the second due to MWNTs. Thereby, MWNTs selectivity was considered as the ratio of weight loss in second step to total weight loss. It should be noted that the sample obtained from packed part at 700 $^{o}$C was mainly amorphous carbon as seen from its low oxidation temperature (Figure 4.6(d)) and inconspicuous XRD pattern (shown in Chapter V, Figure 5.2(e)), indicating to poor heat and mass transfer of packed bed. The effect of temperature on MWNTs productivity, determined form solid carbon conversion concurrently with MWNTs selectivity, was summarized in Table 4.3.

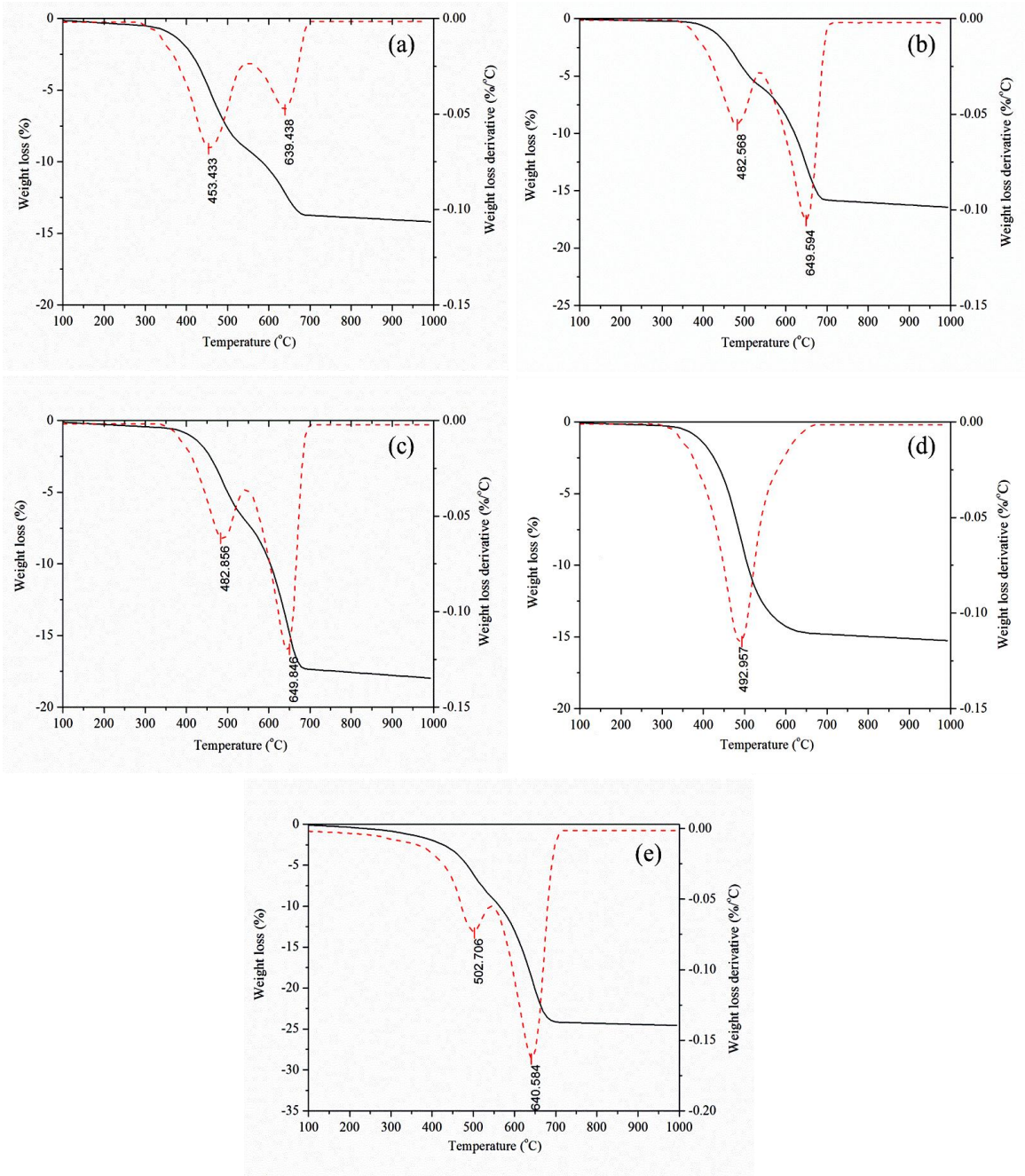


**Figure 4.6** TG/DTA curves of product synthesized at various temperatures; (a) 600 $^{o}$C, (b) 650 $^{o}$C, (c) 675 $^{o}$C, (d) 700 $^{o}$C (packed) and (e) 700 $^{o}$C (fluidized), (0.50 $C_2H_4$ molar fraction, 60 $g_{catalyst}$ and 60 minutes of run duration)

**Table 4.3** MWNTs productivity data at various temperatures

| Temperature ($^oC$) | Solid carbon conversion (%) | MWNTs Selectivity (%) | $T_o$ ($^oC$) |
|---|---|---|---|
| 600 | 63.40 | 32.6 | 639 |
| 650 | 66.32 | 60.2 | 649 |
| 675 | 70.91 | 60.4 | 649 |
| 700packed | 91.24 | Amorphous carbon | |
| 700fluidized | | 65.4 | 640 |

Operating conditions were as follows; 0.50 $C_2H_4$ molar fraction, 60 $g_{catalyst}$ and 60 minutes of run duration

It is clearly seen that the increase in reaction temperature from 600 $^oC$ to 650 $^oC$ lead to a hugely MWNTs selectivity increment (32.6 % and 60.2 % at 600 $^oC$ and 650 $^oC$, respectively) without a significant effect on solid carbon conversion (63.4% and 66.3% at 600 $^oC$ and 650 $^oC$, respectively). The increase in MWNTs selectivity with almost constant solid carbon conversion indicates that the temperature of 600 $^oC$ provides enough energy for dissociation of ethylene but not for MWNTs formation while the temperature of 650 $^oC$ allows both ethylene dissociation and MWNTs formation. For this reason, the product obtained at 600 $^oC$ contains more amorphous carbon, resulting in petty MWNTs selectivity. The increase in temperature from 675 $^oC$ to 700 $^oC$ slightly affects MWNTs selectivity (60.4% and 65.4% at 675 $^oC$ and 700 $^oC$, respectively), on the contrary, considerable affects solid carbon conversion (70.9 % and 91.2 % at 675 $^oC$ and 700 $^oC$, respectively). The increase in solid carbon conversion over 675 $^oC$ to 700 $^oC$ is caused from ethane decomposition which will be expounded in Chapter VI.

**Table 4.4** Bed physical properties data at various temperature (catalyst weight = 60 g)

| Temperature ($^oC$) | $\rho_b$ ($g \bullet cm^{-3}$)[a] | $\rho_g$ ($g \bullet cm^{-3}$)[b] | $D_{[4,3]}$ ($\mu m$)[d] | $U_{mf, 20^oC}$ ($cm \bullet s^{-1}$) | $D_{agglomerate}$ ($\mu m$) | $Re_{mf}$ |
|---|---|---|---|---|---|---|
| 600 | 0.28 | 2.85 | 38.70 | 12.2 | 370 | 2.99 |
| 650 | 0.37 | 2.46 | 33.33 | 12 | 393 | 3.12 |
| 675 | 0.28 | 2.50 | 50.82 | 13 | 410 | 3.53 |
| 700packed | 0.31 | 2.66 | 31.94 | - | - | - |
| 700fluidized | 0.31 | 2.50 | 43.05 | - | - | - |

Operating conditions were as follows; 0.50 $C_2H_4$ molar fraction, 60 $g_{catalyst}$ and 60 minutes of run duration

In term of fluidization and process control, physical properties of bed after MWNTs synthesis at various reaction temperatures were investigated and were summarized in Table 4.4. The results show three important phenomena; Firstly, the significant reduction in bulk density and grain density of catalyst composite. After MWNTs synthesis, bulk density of bed is approximately three times lower, from 1.0 $g \bullet cm^{-3}$ to be approximately 0.3 $g \bullet cm^{-3}$ while grain density of catalyst also decrease, form 3.3 $g \bullet cm^{-3}$ to be approximately 2.5 $g \bullet cm^{-3}$. The falling of bulk density and grain density are caused from MWNTs growth in three dimensional over the grains of the catalyst (Morancais et al., 2007; Philippe et al., 2007). Second phenomenon is the reduction of mean diameter of catalyst composite, analyzed by laser granulometer, as given in Figure 4.7. After MWNTs synthesis, the size distribution of catalyst composite shift to the left (smaller in size). This due to the fact that MWNTs growth inside the pores of the catalyst leads to the internal mechanical force and results in the explosion of alumina grain into the small pieces, as seen from the comparison between Figure 4.4 and 4.10(a). This phenomenon was previously reported in some literatures (Morancais et al., 2007; Philippe et al., 2007).

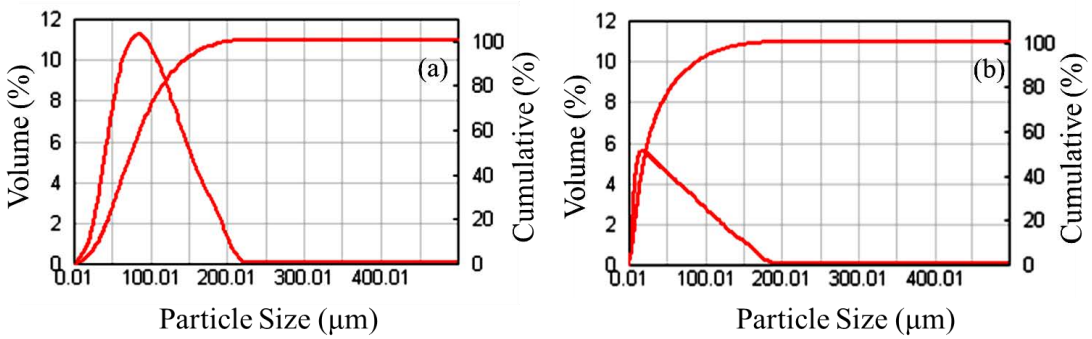


**Figure 4.7** Particle size distributions of powders; (a) Fresh $Co/Al_2O_3$ particle (calcined at 450 $^oC$) and (b) Powder involved in fluidized part

Thirdly, considering $U_{mf}$ from Wen and Yu correlation (Appendix A), as it depends on $D_{[4,3]}$ and $(\rho_g-\rho_f)$, thus the decrease in grain density and size of particle should result in the lower $U_{mf}$. However, the direct measurement of $U_{mf}$ shows the contradictory results as $U_{mf}$ of catalyst composite greatly increase from 0.35 $cm•s^{-1}$ to approximately 12 $cm•s^{-1}$. The unusual $U_{mf}$ increment indicates to the formation of large-loose CNTs agglomerates as proposed by Wang and Hao (Wang et al., 2002; Hao et al., 2003). The mechanism of CNTs agglomerates formation is depicted in Figure 4.8. Unfortunately, the average size of large-loose CNTs agglomerates cannot be measured by laser granulometer since they can be broken up by shear force caused by high power vacuum pump during the measurement. So, their average size must be indirectly evaluated from $U_{mf}$ using Wen and Yu correlation as described in appendix A. It should be noted that this correlation is valid for spheres in the range $0.01 < Re_{mf} < 1000$. The calculated average size of large-loose CNTs agglomerates is in the range of approximately 300 μm to 400 μm which is quite close to the value reported by Hao (Hao et al., 2003).

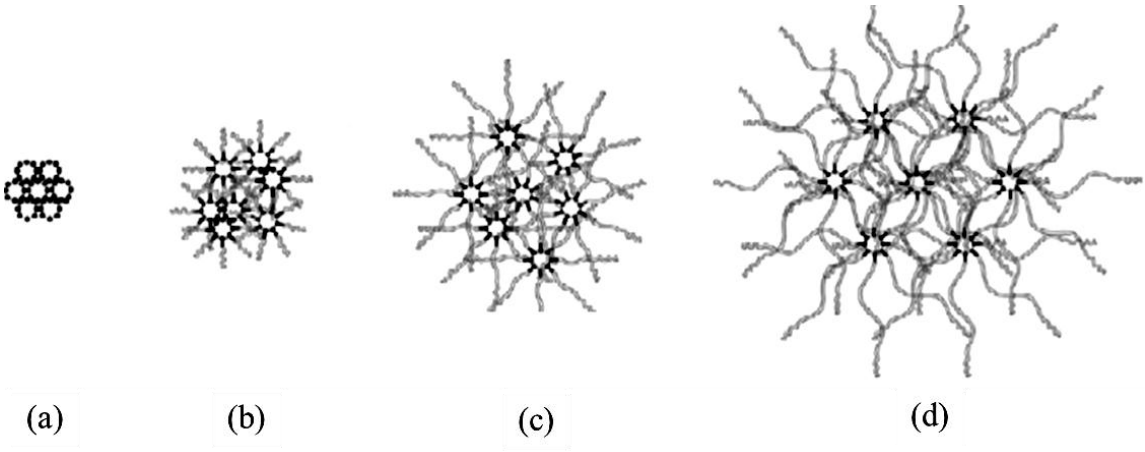


**Figure 4.8** CNT agglomerate formation mechanism; (a) original catalyst particle, (b) the catalyst particle structure is crushed by CNT growth, (c) catalytic particle separated and sub-agglomerates form and (d) fully developed agglomerates (Hao et al., 2003)

The morphology of products were analyzed by using SEM at 200 to 50,000 order of magnitude, SEM image of MWNTs synthesized at temperatures 600 °C, 650 °C, 700 °C (packed) and 700 °C (fluidized) were represented in Figure 4.9, 4.10, 4.11 4.12 and 4.13, respectively. The analysis of the SEM reveals randomly entangled MWNTs with length of several microns. The presence of amorphous carbon can be observed in all Figures. The composite obtained at 700 °C (fluidized part), shown in Figure 4.12(b), contains more amount of MWNTs, while the composite obtained at 700 °C (packed part), shown in Figure 4.13(b), present a lot of amorphous carbon, a good agreement with TGA result.

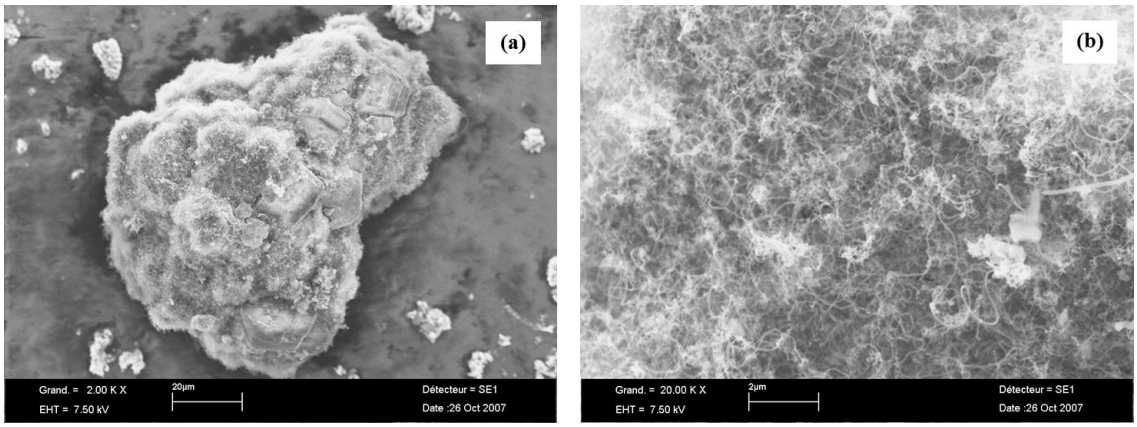


**Figure 4.9** SEM images of product synthesized at 600 $^{o}$C; (a) x2000 and (b) x 20000

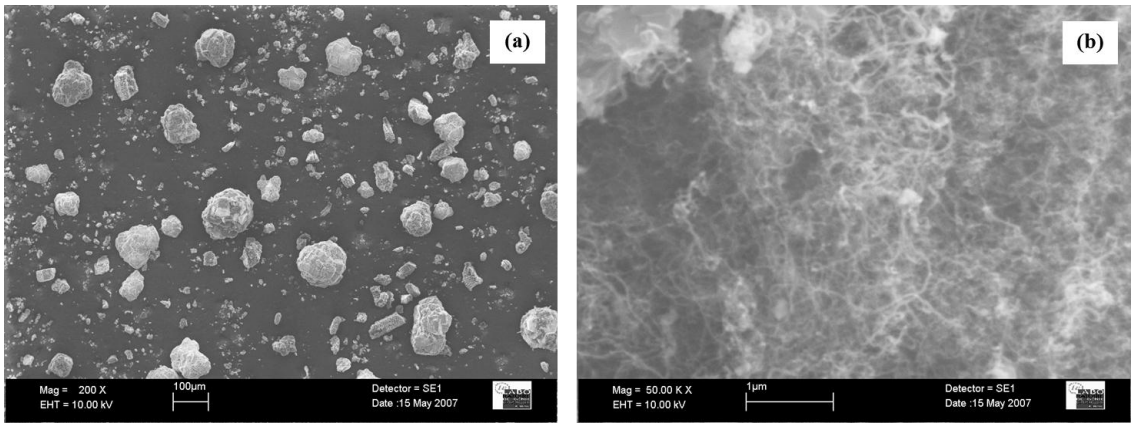


**Figure 4.10** SEM images of product synthesized at 650 $^{o}$C; (a) x200 and (b) x 50000

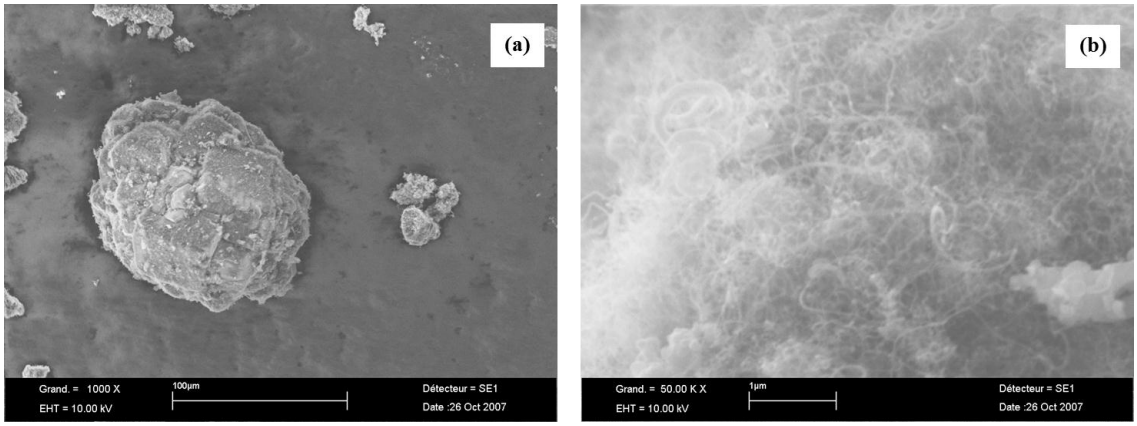


**Figure 4.11** SEM images of product synthesized at 675 $^{o}$C; (a) x1000 and (b) x 50000

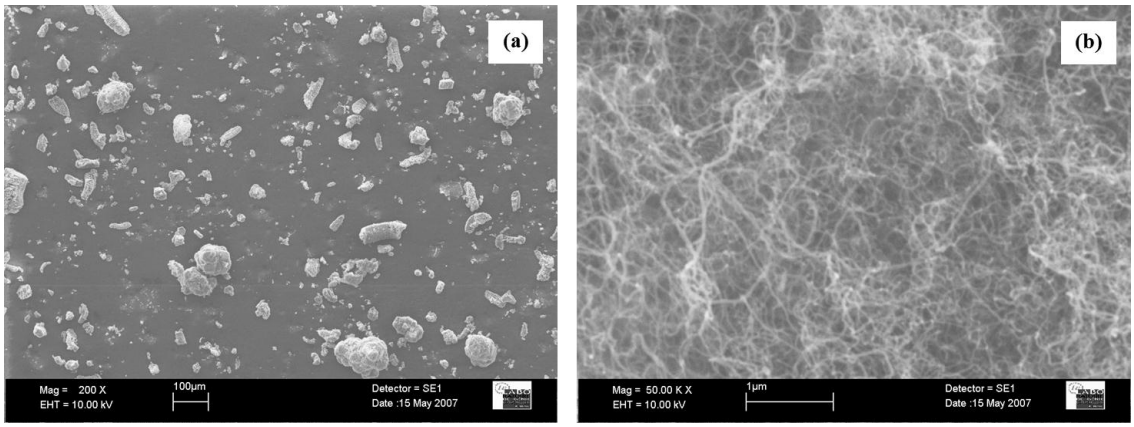


**Figure 4.12** SEM images of product synthesized at 700 $^{o}$C (fluidized); (a) x200 and (b) x 50000

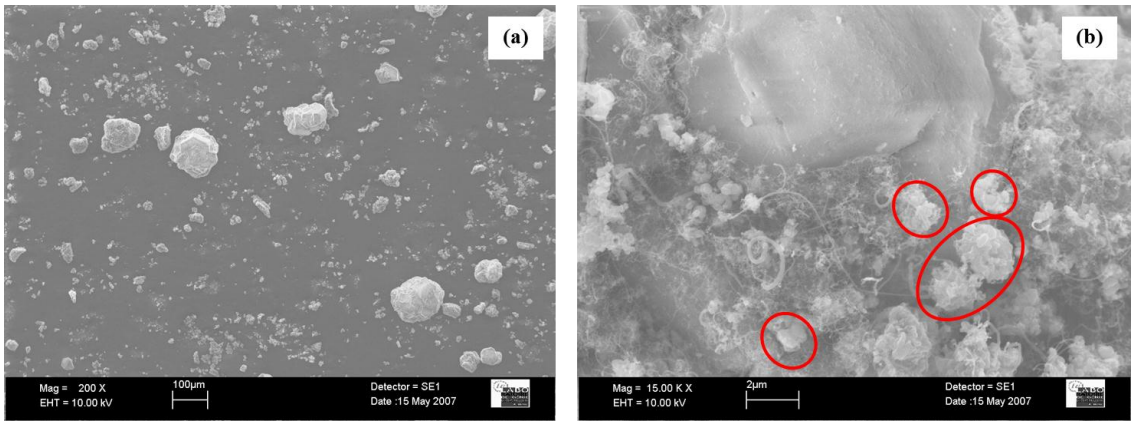


**Figure 4.13** SEM images of product synthesized at 700 $^{o}$C (packed); (a) x200 and (b) x 50000

4.2.2 The effect of temperature on MWNTs synthesis (catalyst weight = 20 g)

Due to the bed agglomeration occurred in previous part, especially at high temperature, this set of experiment was then performed using 20 g of catalyst with aim to solve this problem. In this part, the effect of temperature on MWNTs synthesis was investigated in the temperature range of 550 $^{o}$C to 700 $^{o}$C while the other parameters were kept constant as same as previous section. All operation parameter

were summarized in Table 4.5. The evaluation of MWNTs selectivity by TGA was performed as described in the previous part (4.2.1). TG/DTA results were shown in Figure 4.14.

**Table 4.5** Experimental conditions for investigation of the effect of temperature

| Temperature ($^{o}$C) | Duration (min) | Flow rate (sccm) | | | Carbon input (g) | Weight of catalyst (g) | Initial bed height ($H_0$) (cm) | $U/U_{mf}$ |
|---|---|---|---|---|---|---|---|---|
| | | $N_2$ | $H_2$ | $C_2H_4$ | | | | |
| 550 | 60 | 200 | 200 | 400 | 24.0 | 20 | 1 | 8 |
| 600 | 60 | 200 | 200 | 400 | 24.0 | 20 | 1 | 8 |
| 650 | 60 | 200 | 200 | 400 | 24.0 | 20 | 1 | 8 |
| 700 | 60 | 200 | 200 | 400 | 24.0 | 20 | 1 | 8 |

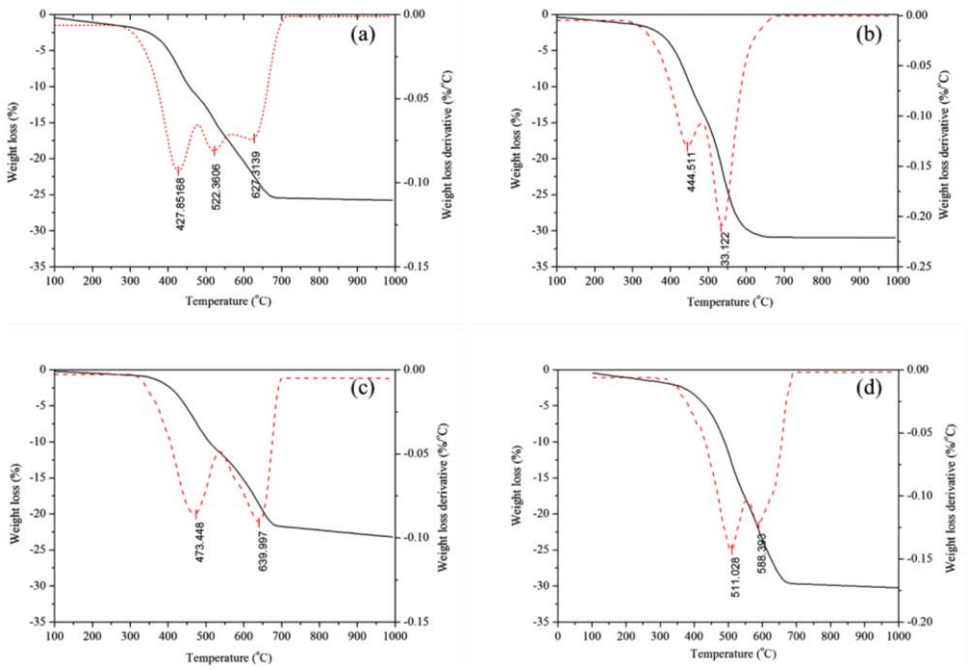


**Figure 4.14** TG/DTA curves of product synthesized at various temperatures; (a) 550 $^{o}$C, (b) 600 $^{o}$C, (c) 650 $^{o}$C and (d) 700 $^{o}$C (0.50 $C_2H_4$ molar fraction, 20 $g_{catalyst}$ and 60 minutes of run duration)

From TGA curves, there are two questionable points that should be discussed. First, the thermal oxidation behavior of product synthesized at 550 $^{o}$C shows in three steps; first step with $T_o$ of 428 $^{o}$C, second step with $T_o$ of 522 $^{o}$C and third step with $T_o$ 627 $^{o}$C. Considering $T_o$ of each steps, the first step can be attributed to amorphous carbon, while the third corresponds to MWNTs. The second step whose $T_o$ locates between that of amorphous carbon and MWNTs arise from the presence of carbon nanofibers (CNFs) as byproduct, as seen from TEM images (Figure 4.19). These nanostructure materials can be described as parallel or oblique stack of graphene layers, are synthesized easier than CNTs due to their less curved shape. The existence of CNFs at low temperature indicates that this temperature provides insufficient energy for MWNTs formation (Philippe et al., 2007). Another questionable result is that the product synthesized at 600 $^{o}$C seems to be CNFs as considered from its low thermal stability ($T_o$ = 533 $^{o}$C). However, their TEM images reveal the fact that the product obtained at this temperature is mainly MWNTs, not CNFs (fig 4.20). A conceivable explanation of this result is that MWNTs synthesized at this temperature may be the poor graphitized MWNTs. This assumption is confirmed by its XRD analysis, shown in Chapter VI.

The effect of temperature on MWNTs productivity was given in Table 4.6. Unsurprisingly, the solid carbon conversion and MWNTs selectivity are quite low at 550 °C since this temperature is sufficient for neither ethylene dissociation nor MWNTs formation (Morancais et al., 2007; Philippe et al., 2009). A raise in reaction temperature to 600 °C lead to an increase in solid carbon conversion, this indicates to sufficient external energy to proceed ethylene dissociation. Moreover, it also allows

the formation of MWNTs (with defective structure), resulting in the MWNTs selectivity increment. Nevertheless, a further rise in reaction temperature leads to the deactivation of catalyst as seen from the reduction of solid carbon conversion and MWNTs selectivity. According to Morancais and co-workers (Morancais et al., 2007), the descending of MWNTs production with respect to temperature, especially at high temperature, is caused by the self-decomposition of ethylene and direct deposit to form amorphous carbon. The physical properties of bed after MWNTs synthesis at various reaction temperatures were investigated and were summarized in Table 4.7. The reduction in bulk density of bed, grain density of particle and mean particle size were also observe as well as the increase in $U_{mf}$ as describe previously in part 4.2.1.

**Table 4.6** MWNTs productivity data at various temperatures

| Temperature ($^oC$) | Solid carbon conversion (%) | MWNTs Selectivity (%) | $T_o$ ($^oC$) |
|---|---|---|---|
| 550 | 27.95 | 27.2*<br>31.9 | 522*<br>627 |
| 600 | 64.24 | 58.6 | 533 |
| 650 | 42.96 | 48.1 | 640 |
| 700 | 40.88 | 42.1 | 588 |

* CNFs

**Table 4.7** Bed physical properties data at various temperatures

| Temperature ($^oC$) | $\rho_b$ ($g \cdot cm^{-3}$)[a] | $\rho_g$ ($g \cdot cm^{-3}$)[b] | $D_{[4,3]}$ ($\mu m$)[d] | $U_{mf, 20\ ^oC}$ ($cm \cdot s^{-1}$) | $D_{agglomerate}$ ($\mu$) | $Re_{mf}$ |
|---|---|---|---|---|---|---|
| 550 | 0.17 | 2.50 | 41.70 | 7.4 | 305 | 1.67 |
| 600 | 0.25 | 2.50 | 22.70 | 8.0 | 317 | 2.07 |
| 650 | 0.24 | 2.50 | 28.66 | 8.5 | 327 | 1.84 |
| 700 | 0.19 | 2.50 | 41.36 | 9.6 | 349 | 2.22 |

The morphology of products were analyzed by using SEM at 200 to 50,000 order of magnitude, SEM image of MWNTs synthesized at temperatures 550, 600, 650 and 700 °C were represented in Figure 4.15, 4.16, 4.17 and 4.18, respectively. Randomly entangled MWNTs with length of several microns are observed. The presence of amorphous carbon at high temperature can be seen in Figure 4.18(b).

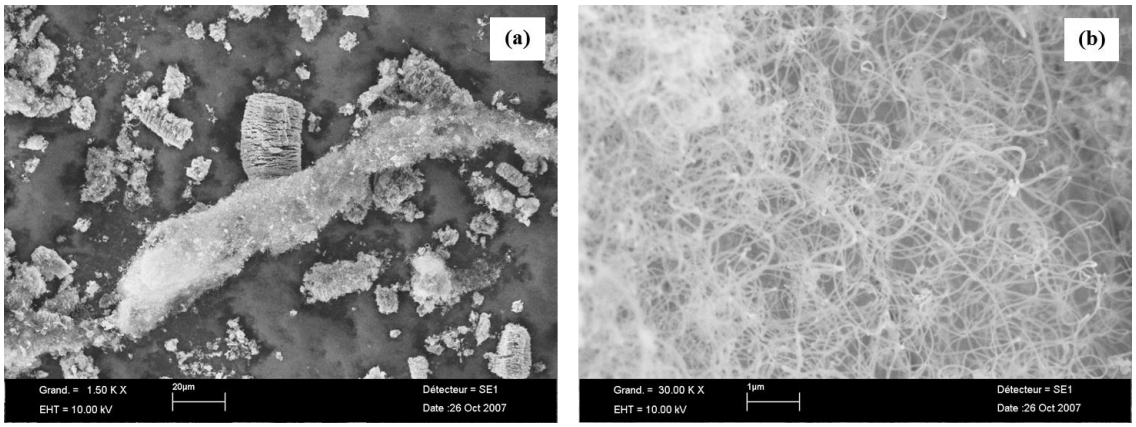


**Figure 4.15** SEM images of product synthesized at 550 $^{o}$C; (a) x1500 and (b) x 30000

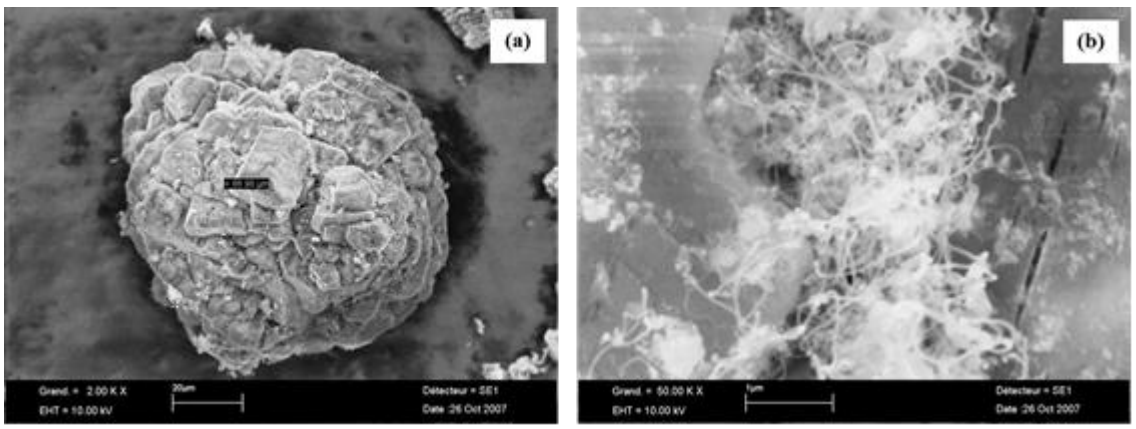


**Figure 4.16** SEM images of product synthesized at 600 $^{o}$C; (a) x2000 and (b) x 50000

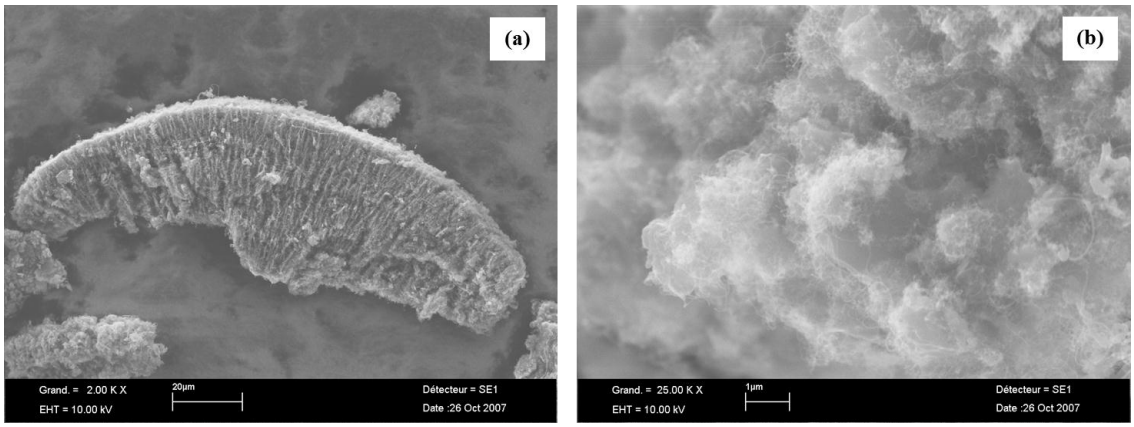


**Figure 4.17** SEM images of product synthesized at 650 $^{o}$C; (a) x2000 and (b) x 25000

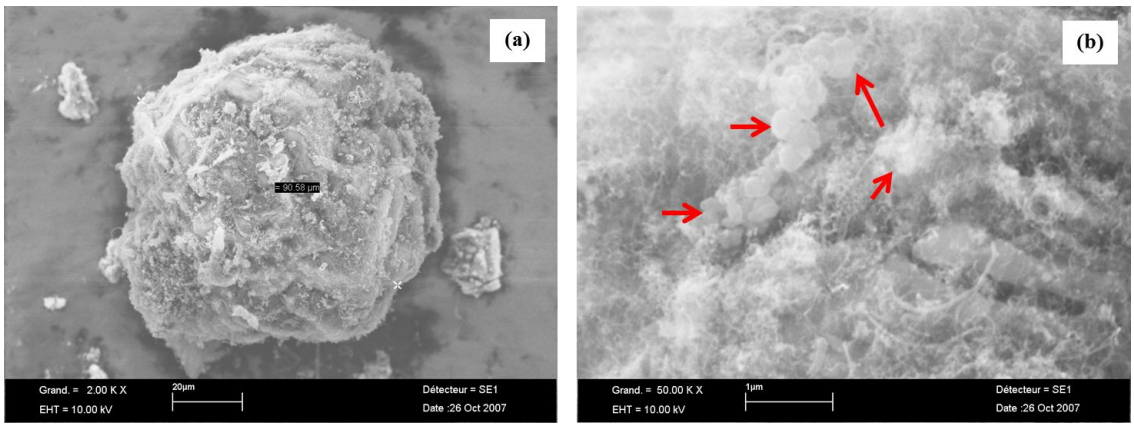


**Figure 4.18** SEM images of product synthesized at 700 $^{o}$C; (a) x2000 and (b) x 50000

From the result of TGA that review the present of unknown product in case the synthesize temperature of 550 $^{o}$C were used. So, the products were analyzed specially by TEM to observe the detail of nano-scale product structure. The results show in the Figure 4.19, 4.20, 4.21 and 4.22 for product synthesized at 550, 600, 650 and 700 $^{o}$C, respectively. It is clearly seen that there are two kinds of products co-exist at 550 $^{o}$C, namely CNFs (large filament) and MWNTs that smaller in diameter.

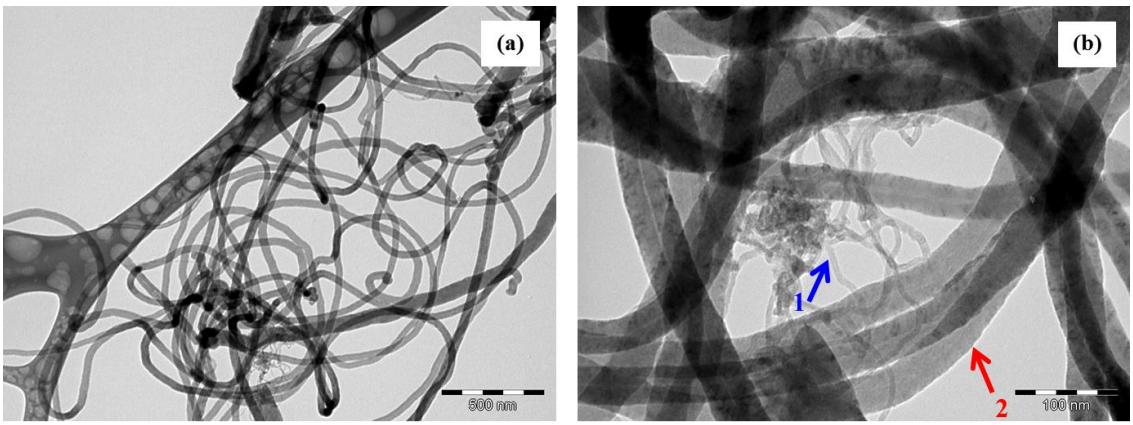


**Figure 4.19** TEM images of product synthesized at 550 $^{o}$C; 1) MWNTs, 2) CNFs

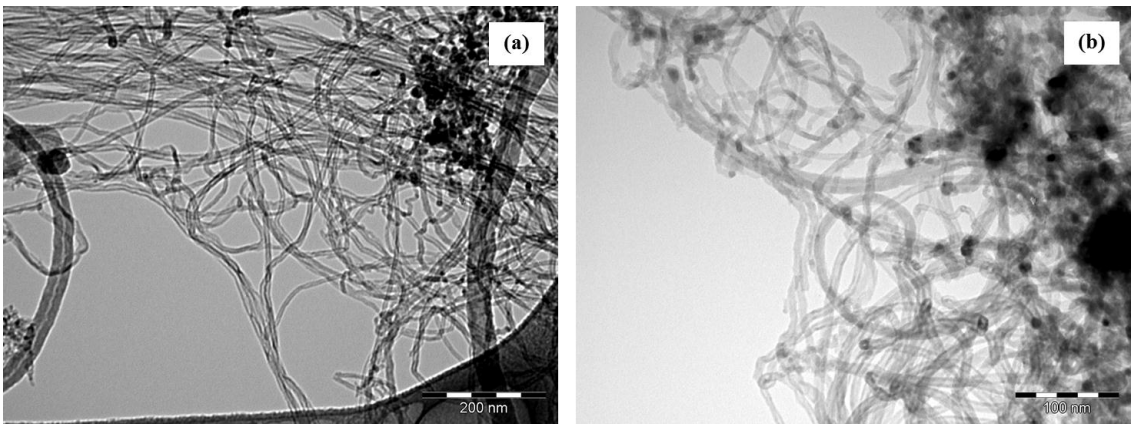


**Figure 4.20** TEM images of product synthesized at 600 $^{o}$C

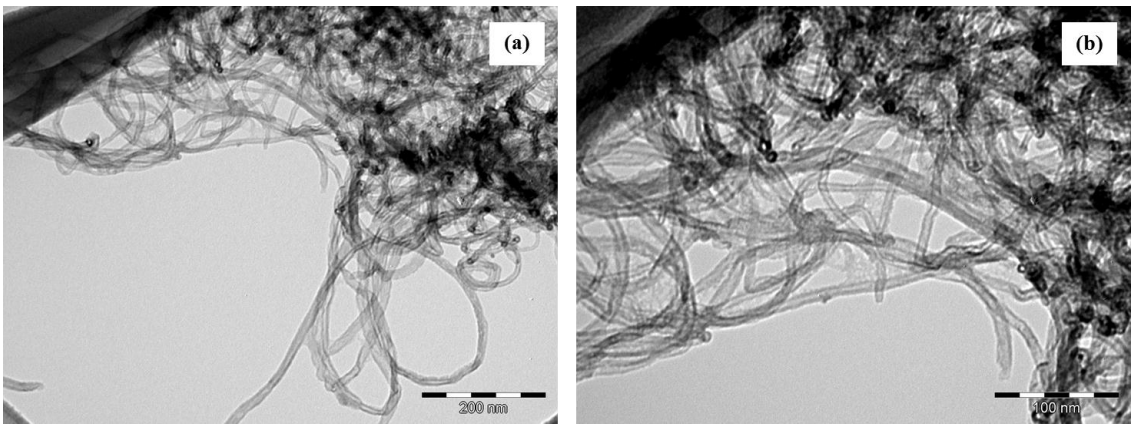


**Figure 4.21** TEM images of product synthesized at 650 $^{o}$C

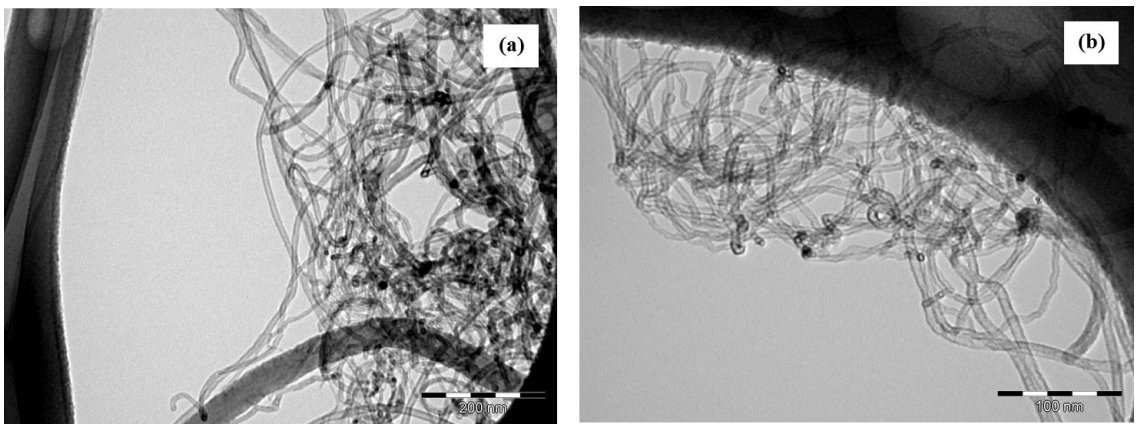


**Figure 4.22** TEM images of product synthesized at 700 $^{o}$C

## 4.3 THE EFFECT OF $C_2H_4$ MOLAR FRACTION ON MWNTS SYNTHESIS

In this part, the effect of $C_2H_4$ molar fraction on the MWNTs production was studied by adjustment of $C_2H_4$ flow rate in the range of 300 to 500 sccm. The other parameters were kept constant as follows; duration 60 minutes, weight of catalyst 20 g and temperature 600 $^{o}$C. All operation parameter were summarized in Table 4.8.

**Table 4.8** Experimental conditions for investigation of the effect of $C_2H_4$ molar fractions

| $C_2H_4$ Molar fraction | Temperature ($^{o}$C) | Duration (min) | Flow rate (sccm) | | | Carbon input (g) | Weight of catalyst (g) | Initial bed height ($H_{0)}$ (cm) | $U/U_{mf}$ |
|---|---|---|---|---|---|---|---|---|---|
| | | | $N_2$ | $H_2$ | $C_2H_4$ | | | | |
| 0.38 | 600 | 60 | 300 | 200 | 300 | 18.0 | 20 | 1 | 8 |
| 0.50 | 600 | 60 | 200 | 200 | 400 | 24.0 | 20 | 1 | 8 |
| 0.63 | 600 | 60 | 100 | 200 | 500 | 30.0 | 20 | 1 | 8 |

The evaluation of MWNTs selectivity was done using TGA as previously mentioned in section 4.2.1 and was given in Figure 4.23. TG/DTA results indicate to two oxidation steps, correspond to amorphous carbon and MWNTs without the existence of CNFs.

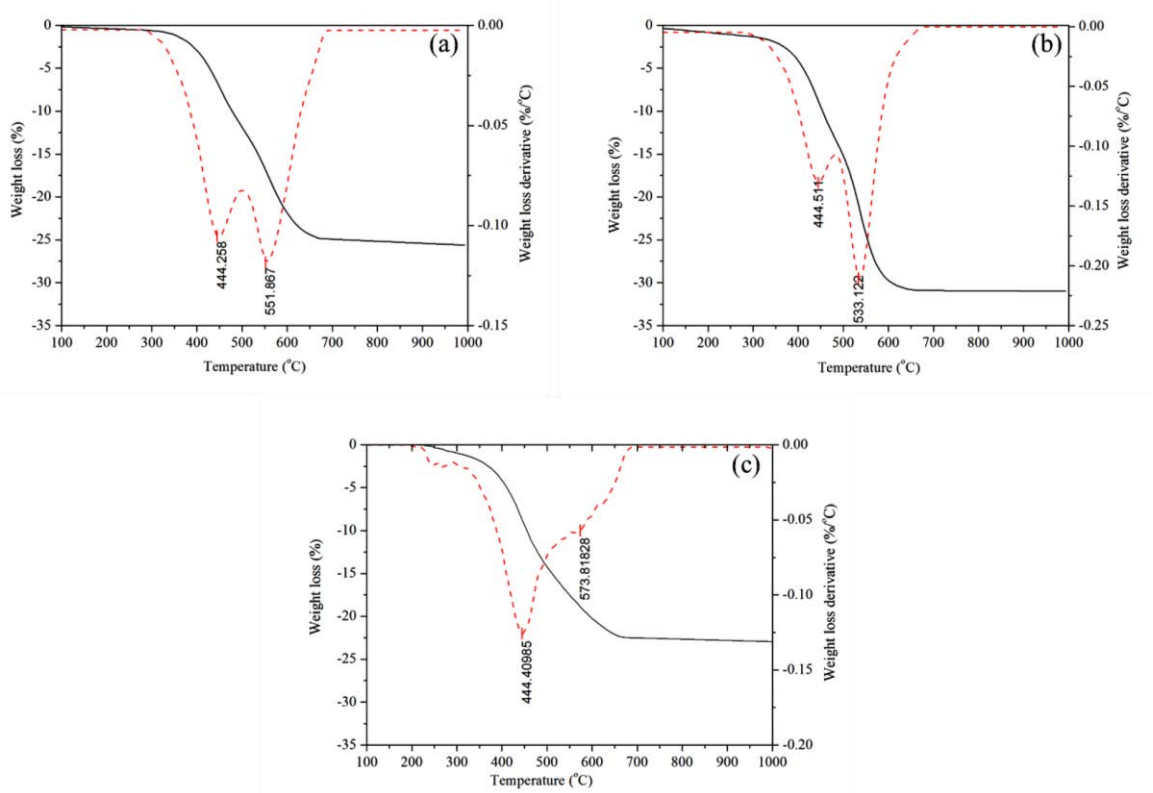


**Figure 4.23** TG/DTA curves of product synthesized at various $C_2H_4$ molar fractions; (a) 0.38, (b) 0.50 and (c) 0.63 (temperature 600 $^oC$, 20 $g_{catalyst}$ and 60 minutes of run duration)

The effect of ethylene molar fraction on MWNTs productivity, determined form solid carbon conversion concurrently with MWNTs selectivity, was summarized in Table 4.9.

**Table 4.9** MWNTs productivity data at various $C_2H_4$ molar fractions

| $C_2H_4$ molar fraction | Solid carbon conversion (%) | MWNTs Selectivity (%) | $T_o$ ($^oC$) |
|---|---|---|---|
| 0.38 | 22.80 | 53.7 | 551 |
| 0.50 | 65.90 | 58.6 | 533 |
| 0.63 | 20.69 | 29.4 | 574 |

It is clearly seen that an increase in ethylene molar fraction from 0.38 to 0.50 greatly affects solid carbon conversion as it increases from 22.8% to 65.9% but less effect on MWNTs selectivity. The solid carbon conversion increment with respect to ethylene molar fraction without any significant change in MWNTs selectivity can be described by the fact that the kinetic law governing MWNTs formation has a positive order dependent on ethylene concentration, written as equation 4.4

$$dX/dt = (k)[C_2H_4]^a \quad (4.4)$$

where $dX/dt$ is MWNTs formation rate, $k$ is rate constant, $P$ is ethylene molar fraction and $a$ is kinetic order, respectively. From above expression, the lower ethylene molar fraction, the slower MWNTs production rate. Because this section was performed with fixed reaction duration, hence, in case of the same time on stream, the low solid carbon conversion obtained at low ethylene molar fraction is somewhat logical. This trend was also reported by some authors (Philippe et al., 2009). However, a further increase in ethylene molar fraction causes unexpected descents in solid carbon conversion and MWNTs selectivity. A plausible cause of these

phenomena is the presence of amorphous carbon on catalyst surface. The existence of amorphous carbon at this condition is due to the fact that under ethylene rich atmosphere, the rapid dissociation of ethylene leads to numerous active carbon precursors available for MWNTs formation. However, due to the rate of MWNTs formation is much slower than that of ethylene dissociation, the excessive active carbon precursors then rearrange themselves to become another product that formed faster, namely amorphous carbon. The best evidences come from SEM images which reveal a lot of amorphous carbon as shown in Figure 4.26. Due to amorphous carbon covers the catalyst particle, it hinders the reactant transport and thus resulting in catalyst poisoning as seen from the low solid carbon conversion. This finding is in agreement with Escobar (Escobar et al., 2007) (TEM images of MWNTs and concomitant amorphous carbon are given in Figure 4.29). The physical properties of bed after MWNTs synthesis at various $C_2H_4$ molar fractions were investigated and were summarized in Table 4.10. The reduction in bulk density of bed, grain density of particle and mean particle size were also observe as well as the increase in $U_{mf}$ as describe previously in part 4.2.1.

**Table 4.10** Bed physical properties data at various $C_2H_4$ molar fractions

| $C_2H_4$ molar fraction | $\rho_b$ $(g \cdot cm^{-3})^a$ | $\rho_g$ $(g \cdot cm^{-3})^b$ | $D_{[4,3]}$ $(\mu m)^d$ | $U_{mf,\ 20^oC}$ $(cm \cdot s^{-1})$ | $D_{agglomerate}$ $(\mu)$ | $Re_{mf}$ |
|---|---|---|---|---|---|---|
| 0.38 | 0.21 | 2.50 | 20.76 | 8.2 | 321 | 1.74 |
| 0.50 | 0.25 | 2.50 | 22.70 | 8.0 | 317 | 2.07 |
| 0.63 | 0.20 | 2.50 | 18.17 | 7.5 | 307 | 1.52 |

The morphology of products were analyzed by using SEM at 200 to 30,000 order of magnitude, SEM image of MWNTs synthesized at $C_2H_4$ molar fraction 0.38, 0.50 and 0.63 were represented in Figure 4.24, 4.25 and 4.26, respectively. In case of high ethylene molar fraction, the existence of amorphous carbon is highlighted as shown in Figure 4.26(b).

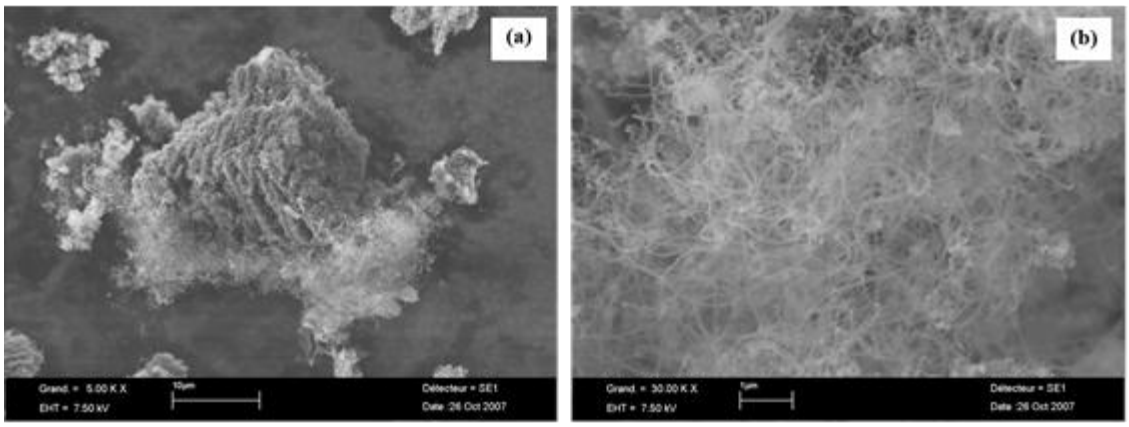


**Figure 4.24** SEM images of product synthesized at $C_2H_4$ molar fraction 0.38; (a) x5000 and (b) x 30000

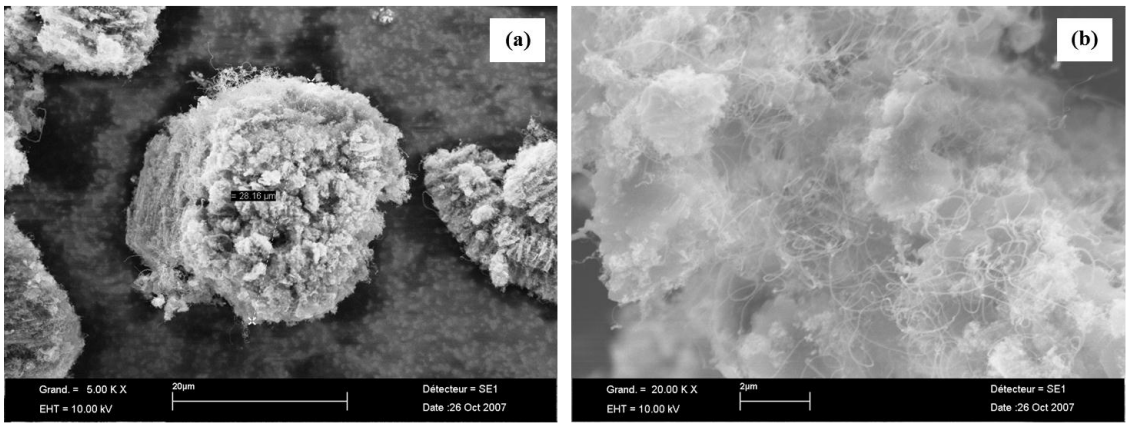


**Figure 4.25** SEM images of product synthesized at $C_2H_4$ molar fraction 0.50; (a) x5000 and (b) x 20000

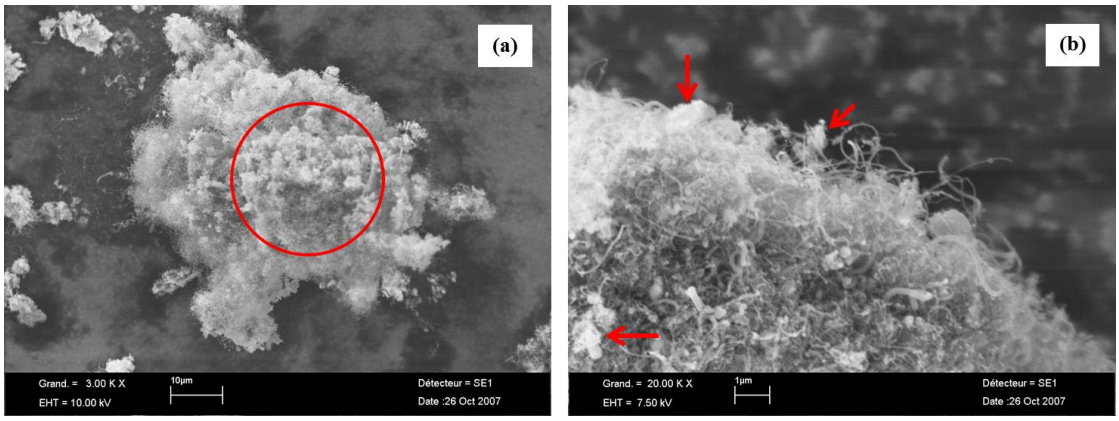


**Figure 4.26** SEM images of product synthesized at $C_2H_4$ molar fraction 0.63; (a) x5000 and (b) x 30000

MWNTs synthesized in this section were also analyzed by TEM to observe the detail of nano-scale product structure. Their TEM images were shown in the Figure 4.27, 4.28 and 4.29 for product synthesized at ethylene molar fraction of 0.38, 0.50 and 0.63, respectively. The products synthesized at ethylene molar fraction of 0.63 are MWNTs and concomitant amorphous as given in Figure 4.29.

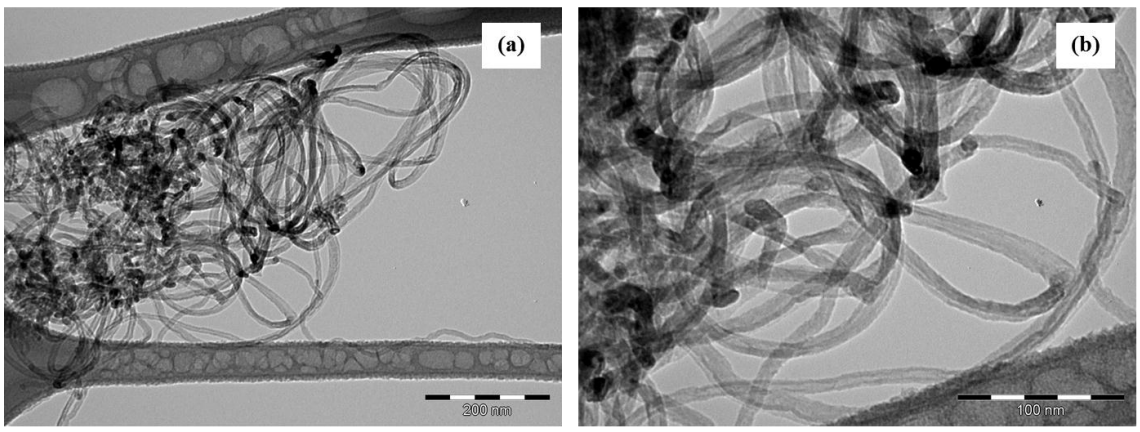


**Figure 4.27** TEM images of product synthesized at $C_2H_4$ molar fraction 0.38

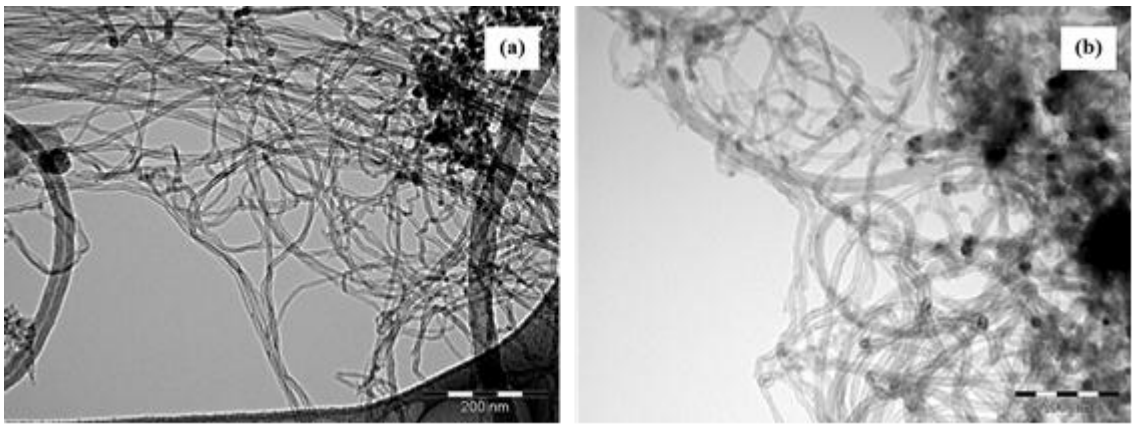


**Figure 4.28** TEM images of product synthesized at $C_2H_4$ molar fraction 0.50

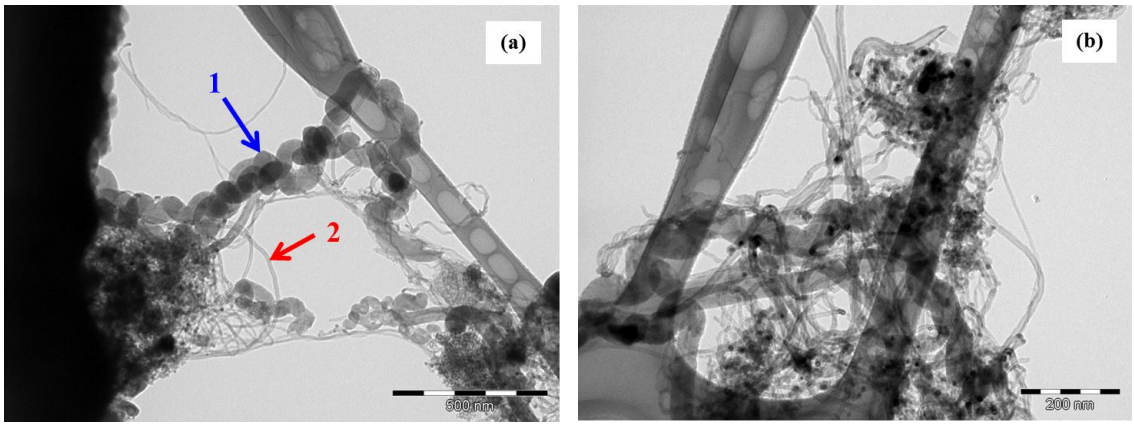


**Figure 4.29** TEM images of product synthesized at $C_2H_4$ molar fraction 0.63

# CHAPTER V

# QUALITATIVE ANALYSIS OF MWNTS

In this Chapter, characteristic and size distributions of synthesized products were studied. There were two main parts in the investigation including; part I: The crystallinity of synthesized products measured by FT- Raman and XRD. And part II: The size distribution of synthesized MWNTs determined by XRD and TEM image analysis.

## 5.1 CRYSTALLINITY OF SYNTHESIZED PRODUCTS

### 5.1.1 Characteristic of synthesized products by Fourier-Transform Raman

The sample of Raman spectra of as prepared composite (carbonaceous product and $Co/Al_2O_3$) obtained at various temperatures was given in Figure 5.1. Two characteristic peaks of CNTs, namely disordered mode (called as D band) and graphite mode (known as G band) were observed, centered at ,350 $cm^{-1}$ and ,5 0 $cm^{-1}$, respectively. The D peak arises from the presence of amorphous carbon, defects, vacancies and imperfection in graphene sheet, whist the G refers to the highly crystalline graphite (Ciambelli et al., 2005). The intense D band supports the findings from TGA analysis (reported in Chapter IV) as the product contains substantial

amorphous carbon. It should be noted that Raman spectra of $Co_3O_4$ that usually present at 484 $cm^{-1}$ and 690 $cm^{-1}$ are hardly observed at this scale due to a quite low Co content and the catalyst dilution with carbonaceous products (Batista et al., 2003). Moreover, a gamma-alumina support does not contribute any Raman spectra since it is a weak Raman scatterer (Weber and Merlin, 2000).

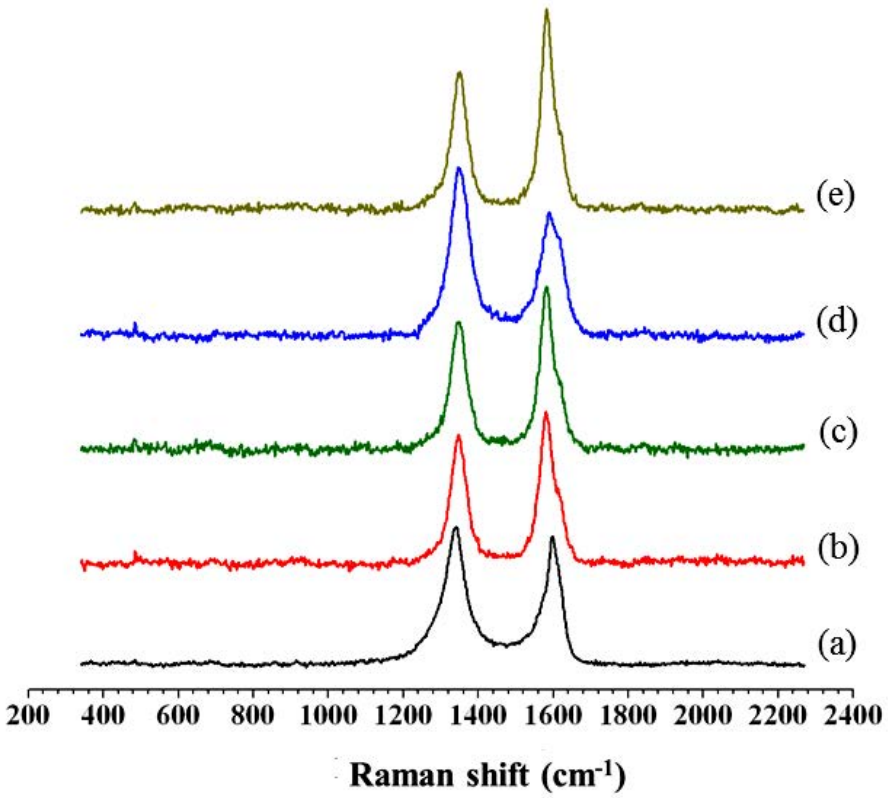


**Figure 5.1** Raman spectra of the products synthesized at various temperatures; (a) 600 $^oC$, (b) 650 $^oC$, (c) 675 $^oC$, (d) 700 $^oC$ (packed) and (e) 700 $^oC$ (fluidized); (0.50 $C_2H_4$ molar fraction, 60 $g_{catalyst}$ and 60 minutes of run duration)

The values of D/G intensity ratio ($I_D/I_G$) that refer to disordered amount for CNTs produced at different temperature, weight of catalyst and ethylene feed molar fraction are reported in Table 5.1. It can be clearly seen that the $I_D/I_G$ intensity ratios are in good agreement with MWNTs selectivity and are very far from that of

commercial MWNTs which is often less than 0.02, in this case, due to the composite was analyzed without any separation or purification steps hence the intensity of D band is possibly mainly originated from the presence of amorphous carbon rather than defects in MWNTs structure. Therefore, for better understanding the effect of process parameters on MWNTs crystallinity, additional analysis such as XRD should be conducted.

**Table 5.1** Raman spectroscopy analysis results

| | Temperature ($^oC$) | $I_D/I_G$ | MWNTs Selectivity[a] (%) |
|---|---|---|---|
| **Data Set [1]** | 600 | 1.07 | 32.6 |
| | 650 | 0.84 | 60.2 |
| | 675 | 0.79 | 60.4 |
| | $700_{fluidized}$ | 0.69 | 65.4 |
| | $700_{packed}$ | 1.36 | Amorphous carbon |
| | 550* | 1.11 | 59.1[b] |
| | 600* | 1.07 | 58.6 |
| | 650* | 1.16 | 48.1 |
| | 700* | 1.17 | 42.1 |
| **Data Set [2]** | $C_2H_4$ molar fraction | $I_D/I_G$ | MWNTs Selectivity (%) |
| | 0.38 | 1.13 | 53.7 |
| | 0.50 | 1.07 | 58.6 |
| | 0.63 | 1.24 | 29.4 |

[1] Evaluating the effect of temperature; 0.50 $C_2H_4$ molar fraction, 60 $g_{catalyst}$ (*0.50 $C_2H_4$ molar fraction, 20 $g_{catalyst}$) and 60 minutes of run duration
[2] Evaluating the effect of ethylene molar fraction; temperature 600 $^oC$, 60 $g_{catalyst}$ and 60 minutes of run duration
[a] Determined from TGA
[b] A combination of CNFs and MWNTs selectivity

### 5.1.2 Characteristic of $Co/Al_2O_3$ catalyst and products synthesized by X-ray diffraction

This section describes XRD spectra of the as-prepared product with the aim to observe the carbon (0 0 2) diffraction peak whose maximum intensity presents at diffraction angle ($2\theta_{max}$) near $26^o$. An advantage of XRD is that the presence of amorphous carbon does not affect the position of $2\theta_{max}$ since its XRD spectra appear undistinguished. The carbon (0 0 2) diffraction peak provides the information for evaluating the tubes characteristic as the interplanar distance "d (0 0 2)" between nanotubes walls, calculated by Bragg's law. For graphitic carbon, the interplanar distance can be converted to the degree of graphitization "g" as per the Maire and Mering formula (Maire and Mering, 1970):

$$d(0\ 0\ 2) = 3.354 + 0.086\,(100 - g) \qquad (5.1)$$

where d (0 0 2) is the interplanar distance in angstroms, g is the degree of graphitization in percent. The higher the interplanar distance, the lower the degree of graphitization and thus, the lower the crystallinity. In detail, the degree of graphitization refers to a transition realm of graphite-like material to highly ordered pyrolytic graphite (HOPG) and disordered graphite. If the degree of graphitization is 100 %, d (0 0 2) is taken as 3.354 Å, corresponding to that of HOPG. Vice versa, in case the degree of graphitization is equal to zero, d (0 0 2) is found to be 3.440 Å, consistent with that of turbostratic graphite. For CNTs, a reasonable explanation of the (0 0 2) interplanar distance increment is that there curved shape of CNTs lead to an internal stress, resulting in a misplacement of atomic layer. A microstrain "ε" caused by an internal stress across the tube expresses as:

$$\varepsilon = \Delta d/d_0 \qquad (5.2)$$

where $d_0$ is the interplanar distance for a perfect crystalline and $\Delta d$ is the difference in the interplanar distance caused by the stress, respectively. In this thesis, the interplanar distance of HOPG (3.354 Å) was set as $d_0$. The stress "σ" across the tube axis can be calculated by:

$$\sigma = \varepsilon \cdot E \qquad (5.3)$$

where $E$ is elastic modulus (1000 GPa) of the well graphitized MWNTs (Yu, 2004).

5.1.2.1 The effect of temperature on crystallinity of synthesized products

The XRD patterns of as prepared product synthesized at 600, 650, 675 and 700 $^{o}$C were demonstrated in Figure 5.2. It can be seen that, after MWNTs synthesis, the peak of $Co_3O_4$ located at $2\theta = 19.0^{o}$ (1 1 1), $31.3^{o}$ (2 2 0), $36.8^{o}$ (3 1 1) and $59.4^{o}$ (5 1 1) disappear due to the in-situ reduction of this phase to $Co^0$ before the experiment, however, the XRD spectra do not show any diffraction peak of $Co^0$. On the other hand, there are 2 peaks exist, namely $Co_3C$ whose diffraction angle locates at $2\theta = 44.1^{o}$ and carbon (0 0 2) whose diffraction angle locates at $2\theta$ $26.5^{o}$. The nonexistence of $Co^0$ coincides with the presence of $Co_3C$ indicates that, during MWNTS synthesis, $Co^0$ converts to $Co_3C$ which is a real active phase for MWNTs growing (Starmatin et al., 2007). The intensity of carbon (0 0 2) diffraction peak trends to increase with an increasing in reaction temperature, this is in agreement with the amount of MWNTs deposit as previously described in chapter IV. Please be reminded that in case of using a reaction temperature of 700 $^{o}$C, the partial agglomeration of bed was encountered, resulting in the separation of bed as a minor "packed" part (above the gas distributor surface) and a major "fluidized" part. For the

sample obtained from packed part, its XRD pattern shows a weak carbon (0 0 2) diffraction peak, while a prominent carbon (0 0 2) diffraction peak of the sample in fluidized part can be found. Unsurprisingly, as revealed by TGA, the product obtained from packed part contains mainly amorphous carbon, resulting in an indistinct of carbon (0 0 2) diffraction peak. The difference in XRD pattern of the product obtained from packed and fluidized part confirms a drawback of packed bed caused by poor heat and mass transfer.

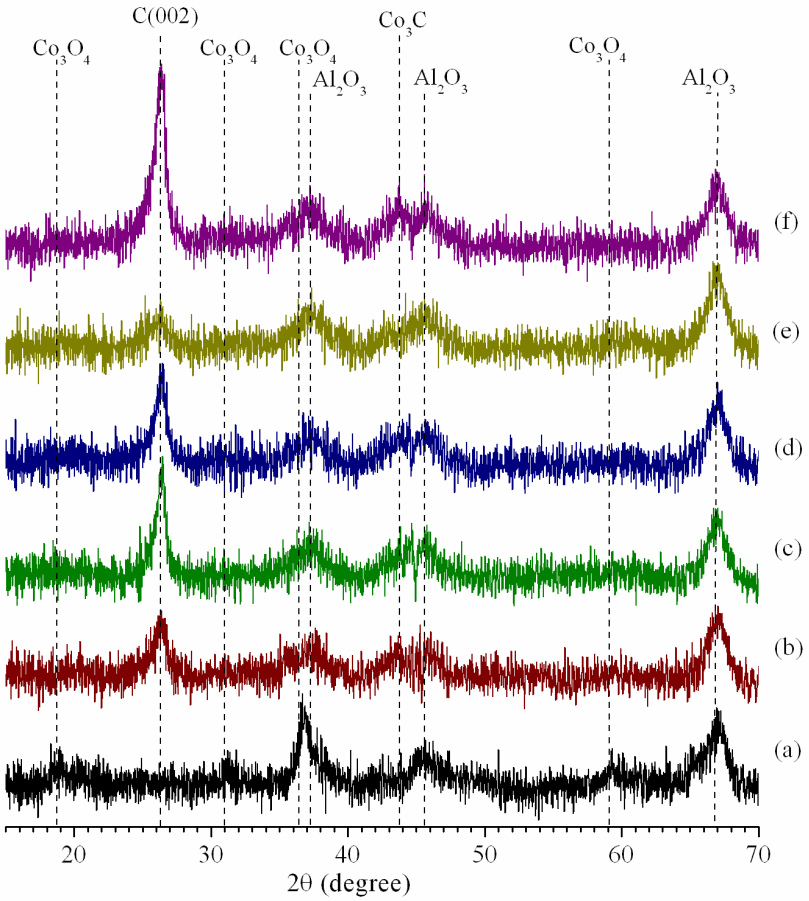


**Figure 5.2** XRD patterns of fresh catalyst and products synthesized at various temperatures; (a) fresh catalyst, (b) 600 $^{o}$C, (c) 650 $^{o}$C, (d) 675 $^{o}$C, (e) 700 $^{o}$C (packed) and (f) 700 $^{o}$C (fluidized) (0.50 $C_2H_4$ molar fraction, 60 $g_{catalyst}$ and 60 minutes of run duration)

From the diffraction angle of carbon (0 0 2), the interplanar spacing, the degree of graphitization, the microstrain and the stress can be calculated, as summarized in Table 5.2 It can be seen that the degree of graphitization increases with the increment of reaction temperature from 600 $^{o}$C to 700 $^{o}$C (~69.6%, ~73.1%, ~83.9% and ~90.6% for 600, 650, 675 and $700_{fluidized}$ $^{o}$C, respectively) while the microstrain and stress, on the other hand, decrease as temperature increases. This refers to the better crystallinity of graphene lattice obtained at high reaction temperature. Due to MWNTs structure relate to the "rolled" or "wrapped" graphene sheet, their curved shape lead to high internal stress and strain and resulting in large interlayer spacing, the higher external energy to overcome the MWNTs formation barrier is therefore essential in order to synthesis more crystalline MWNTs.

**Table 5.2** XRD analysis results for investigation of the effect of temperature on MWNTs crystallinity

| Temperature ($^{o}$C) | $2\theta_{max}$ (degree) | d (0 0 2) (Å) | Degree of graphitization (%) | ε (%) | σ (GPa) |
|---|---|---|---|---|---|
| 600 | 26.346 | 3.380 | 69.58 | 0.780 | 7.80 |
| 650 | 26.370 | 3.376 | 73.16 | 0.688 | 6.88 |
| 675 | 26.443 | 3.371 | 83.87 | 0.414 | 4.14 |
| $700_{fluidized}$ | 26.490 | 3.3621 | 90.58 | 0.242 | 2.42 |

Operating conditions were as follows; 0.50 $C_2H_4$ molar fraction, 60 $g_{catalyst}$ and 60 minutes of run duration

To confirm the effect of temperature on MWNTs crystallinity in terms of degree of graphitization, the products synthesized in the second set of experiment were also analyzed by XRD. The XRD patterns of products synthesized at various temperatures in the second set of experiment, as shown in Figure 5.3, look similar to

the patterns mentioned in previous section as the carbon (0 0 2) diffraction is the major peak.

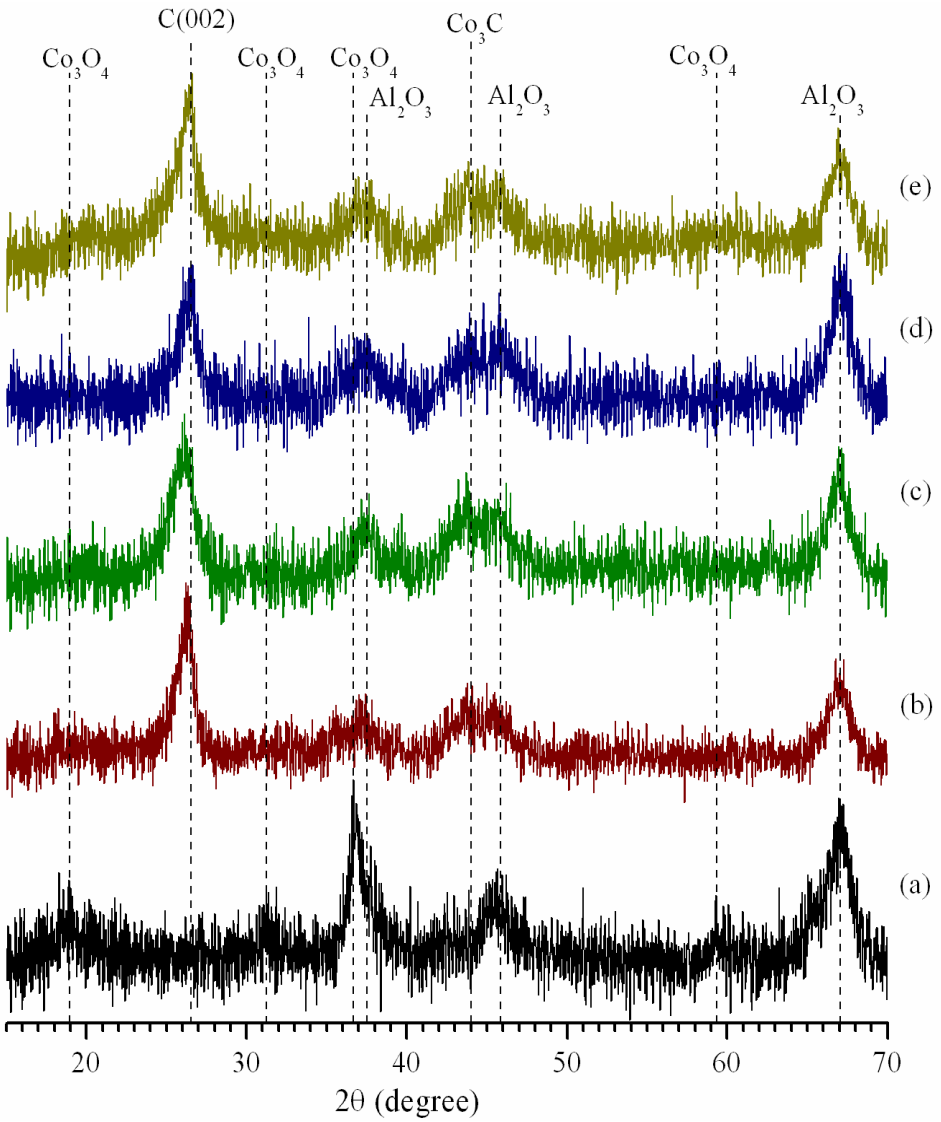


**Figure 5.3** XRD patterns of fresh catalyst and products synthesized at various temperatures; (a) fresh catalyst, (b) 550 $^{o}$C, (c) 600 $^{o}$C, (d) 650 $^{o}$C and (e) 700 $^{o}$C (0.50 $C_2H_4$ molar fraction, 20 $g_{catalyst}$ and 60 minutes of run duration)

The effect of temperature on MWNTs crystallinity in term of the degree of graphitization studied in the range of 550 $^{o}$C to 700 $^{o}$C was given in Table 5.3. It can

be seen that the peak of carbon (0 0 2) diffraction of the products synthesized at higher temperature shift to the higher angle, namely 26.216°, 26.268 °, 26.384° and 26.407° for 550, 600, 650 and 700 °C, respectively, which refers to a decrement of (0 0 2) spacing. Degree of graphitization extracted from carbon (0 0 2) spacing of each sample were found to be ~50.4%, ~58.1%, ~75.2% and ~78.6% for 550, 600, 650 and 700 °C, respectively, while the microstrain and stress decrease as temperature increases, follow the same trend as in previous section. This confirms that temperature plays a key role on the formation of well graphitized MWNTs. It is noteworthy that the product synthesized at 550 °C and 600 °C show moderate degree of graphitization values which are in very good agreement with their low oxidation temperatures ($T_o$) as observed from TGA (previously shown in section 4.2.2). In other words, it can be argued that the astounding poor crystallinity of MWNTs (or CNFs) produced at these two conditions are the cause of the low thermal stability under oxidizing atmosphere

.**Table 5.3** XRD analysis results for investigation of the effect of temperature on MWNTs crystallinity

| Temperature (°C) | $2\theta_{max}$ (degree) | d (0 0 2) (Å) | Degree of graphitization (%) | ε (%) | σ (GPa) |
|---|---|---|---|---|---|
| 550 | 26.216 | 3.397 | 50.44 | 1.271 | 12.71 |
| 600 | 26.268 | 3.390 | 58.10 | 1.074 | 10.74 |
| 650 | 26.384 | 3.375 | 75.23 | 0.635 | 6.35 |
| 700 | 26.407 | 3.372 | 78.57 | 0.549 | 5.49 |

Operating conditions were as follows; 0.50 $C_2H_4$ molar fraction, 20 $g_{catalyst}$ and 60 minutes of run duration

5.1.2.2 The effect of $C_2H_4$ molar fraction on XRD patterns of products synthesized.

The effect of ethylene molar fraction on XRD patterns of products was shown in Figure 5.4. The XRD patterns of as prepared product synthesized at ethylene molar fraction of 0.38 shows a weak carbon (0 0 2) diffraction peak, conform to a low amount MWNTs as analyzed by TGA as mention in chapter IV.

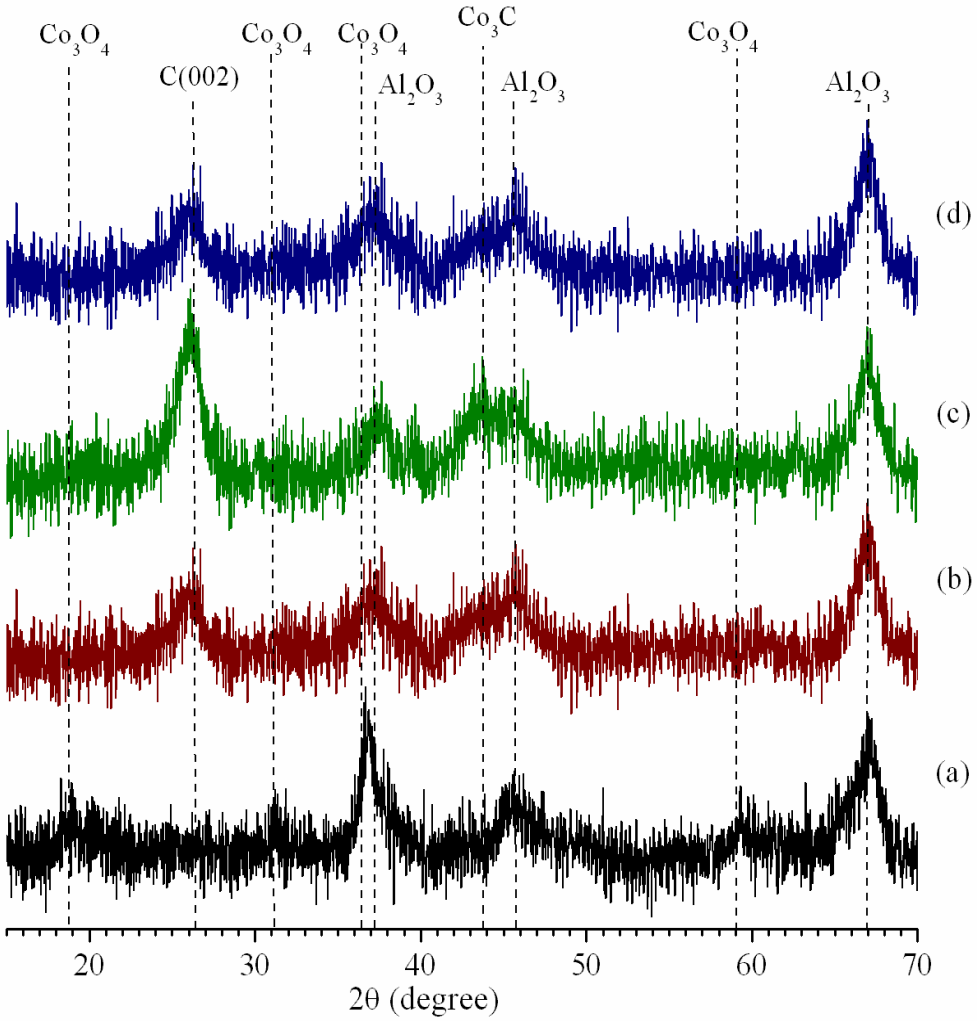


**Figure 5.4** XRD patterns of fresh catalyst and products synthesized at various $C_2H_4$ molar fraction; (a) fresh catalyst, (b) 0.38, (c) 0.50 and (d) 0.63 (temperature 600 $^{o}$C, 20 $g_{catalyst}$ and 60 minutes of run duration)

When the ethylene molar fraction was increase to 0.50, the obvious carbon (0 0 2) diffraction peak was found at 2θ 26.268°, indicating to the presence of MWNTs. On the other hand, a further increase in ethylene molar fraction results in an ambiguous carbon (0 0 2) diffraction peak due to the presence of amorphous carbon as a major product, as mention in TGA result in chapter IV.

The XRD analysis results for investigation of the effect of $C_2H_4$ molar fraction on MWNTs crystallinity (temperature 600 °C, 20 $g_{catalyst}$ and 60 minutes of run duration) was given in Table 5.4. It should be note that due to the indistinct carbon (0 0 2) diffraction peak, the evaluating of crystallinity in term of interplanar distance, degree of graphitization, internal stain and stress might be inaccurate and unreliable. The results lead to the conclusion that ethylene molar fraction of 0.50 is the most suitable condition for MWNTs synthesis since it provides the highest MWNTs productivity (0.45 $g_{MWNTs} \bullet g_{cata}^{-1}$).

**Table 5.4** XRD analysis results for investigation of the effect of $C_2H_4$ molar fraction on MWNTs crystallinity

| $C_2H_4$ molar fraction | $2\theta_{max}$ (degree) | d (0 0 2) (Å) | Degree of graphitization (%) | ε (%) | σ (GPa) |
|---|---|---|---|---|---|
| 0.38* | 26.276 | 3.389 | 59.42 | 1.041 | 10.41 |
| 0.50 | 26.268 | 3.390 | 58.10 | 1.074 | 10.74 |
| 0.63* | 26.307 | 3.385 | 63.94 | 0.925 | 9.25 |

Operating conditions were as follows; temperature 600 °C, 20 $g_{catalyst,}$ 60 minutes of run duration
*obscure carbon (0 0 2) diffraction

## 5.2 SIZE DISTRIBUTION OF SYNTHESIZED MWNTs

Various techniques have been developed to determine the diameter of nanoscale sample. The most commonly used methods comprise X-ray diffraction (XRD), Transmission electron microscopy (TEM) and others. Although various methods are available, the accuracy of the results for the particle size is not always clear because of possible systematic errors in the analysis. All of the techniques have their own advantages and disadvantages. Transmission electron microscopy (TEM) is the most versatile analytical technique that allows the real observation of the samples. However, the particle size measurement from TEM image often faces the lack of contrast problem which lead to the vague observation of particle boundaries. XRD is indirect method that can be used for determination of particle size from the X-ray diffraction line broadening by the so-called Debye-Scherrer equation. In this section, the investigation of MWNTs size was done using XRD and TEM in order to study the effect of temperature and ethylene molar fraction on MWNTs size distribution and to compare the result as obtained from these two techniques.

### 5.2.1 Size distribution of synthesized MWNTs as determined by XRD analysis

The average outer diameter of MWNTs was calculated from line broadening at half the maximum intensity (FWHM) and Bragg angle of carbon (0 0 2) diffraction peak using Debye-Scherrer equation. The XRD patterns of MWNTs mentioned in this section were already shown in Figure 5.3. The results of average MWNTs diameter determined from XRD were summarized in Table 5.5.

**Table 5.5** Summary of XRD analysis result.

| | Temperature ($^oC$) | 2θ (degree) | FWHM (degree) | Outer diameter (nm) |
|---|---|---|---|---|
| **Data Set [1]** | 550 | 26.216 | 1.161 | 7.0 |
| | 600 | 26.268 | 1.150 | 7.1 |
| | 650 | 26.384 | 1.086 | 7.5 |
| | 700 | 26.407 | 1.272 | 6.4 |
| | $C_2H_4$ molar fraction | 2θ (degree) | FWHM (degree) | Outer diameter (nm) |
| **Data Set [2]** | 0.38 | 26.276 | 1.196 | 6.8 |
| | 0.50 | 26.268 | 1.150 | 7.1 |
| | 0.63 | 26.307 | 1.871 | 4.3 |

[1] Evaluating the effect of temperature; 0.50 $C_2H_4$ molar fraction, 20 $g_{catalyst}$ and 60 minutes of run duration

[2] Evaluating the effect of ethylene molar fraction; temperature 600 $^oC$, 20 $g_{catalyst}$ and 60 minutes of run duration

The effect of temperature on the average outer diameter of MWNTs was evaluated in the range of 550 $^oC$ to 700 $^oC$ corresponding to Data Set[1]. The results show that the average size of MWNTs synthesized at 550, 600, 650 and 700 $^oC$ is found to be 7.0, 7.1, 7.5 and 6.4 nm, respectively. These values are quite close to the $Co^0$ particle size of 7.4 nm, indicating to the relationship between MWNTs outer diameter and metal particle size. However, the temperature seems to have no significant effect on MWNTs outer diameter in this temperature range studied, this conclusion will be confirmed by TEM analysis in next section.

The effect of ethylene molar fraction on the average outer diameter of MWNTs was evaluated in the range of 0.38 to 0.63 corresponding to Data Set[2]. The

results show that the average outer diameter of MWNTs synthesized at 0.38, 0.50 and 0.63 is found to be 6.8, 7.1 and 4.3 nm, respectively. Once again, XRD results do not show significant effect of ethylene molar fraction on MWNTs outer diameter in this range studied. It should be noted that the carbon (0 0 2) diffraction peak of product synthesized at ethylene molar fraction of 0.63 are quite low in intensity (as seen in Figure 5.4) due to the present of amorphous carbon as main product, resulting in the inaccurate measurement of diffraction angle and line broadening and lead to the unreliable MWNTs outer diameter.

### 5.2.2 Size distribution of synthesized MWNTs as determined by TEM image analysis

In this section, the as-prepared MWNTs size distribution analysis was determined from various TEM images. The manipulation of raw TEM images (e.g. brightness/contrast adjustment and background subtraction) was performed using image processing program “ImageJ” in order to facilitate the observation of individual nanotubes boundaries. For each sample, the outer diameters of 130 to 150 tubes were measured and were represented by histograms together with the best-fit statistical model obtained from “Origin” program. Histograms of the outer diameters of MWNTs synthesized at various temperatures were shown in Figure 5.5.

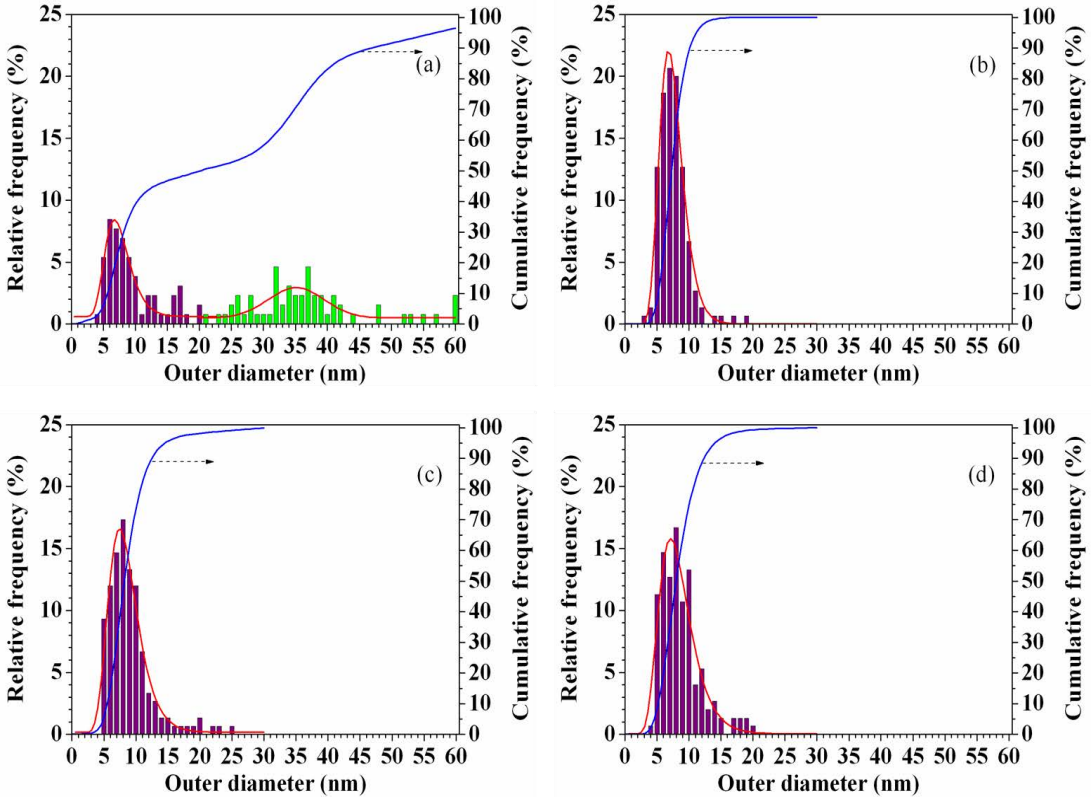


**Figure 5.5** Histograms of the diameter of MWNTs at various temperatures; (a) 550 $^{o}$C, (b) 600 $^{o}$C, (c) 650 $^{o}$C and (d) 700 $^{o}$C (0.50 $C_2H_4$ molar fraction, 20 $g_{catalyst}$ and 60 minutes of run duration)

The results show that outer diameter of product synthesized at 550 °C contains two distinct populations with different attributes. The first mode, represented as purple bars, lies on a narrow range between 4 to 12 nm corresponding to a log-normal distribution with an average (median) diameter of 7.3 nm while the second mode, showed as green bars, is a broad Gaussian distribution in the range of 20 to 60 nm with an average (median) diameter of 35.1 nm. A bimodal distribution of product synthesized at this temperature reflects the coexistence of two products, in this case, the first mode is the distribution of MWNTs whilst the second mode is the distribution of byproduct, namely CNFs which are easier to be synthesized than MWNTs,

consistent with the results of TGA represented in chapter IV. In the case of higher growth temperatures, the distribution of CNFs disappears, remaining only the distribution of the MWNTs that follows a log-normal distribution with an average (median) size of 7.3, 8.1, and 8.0 nm for growing temperature 600, 650 and 700 $^{o}$C respectively. It is noteworthy that the size distribution of as-prepared MWNTs is well described by a log-normal profile instead of a Gaussian (normal) distribution.

The cause of the deviations from a Gaussian profile is the absence of product with outer diameters smaller than 3 nm which corresponds to typical SWNT or DWNTs outer diameter, or it can be said that this value is a lower bound of the as-prepared MWNTs diameters range. The non-occurrence of very small CNTs indicates to the harder the graphitization owing to their high curvature. For the size distribution of product synthesized at various ethylene molar fractions, the histograms were given in Figure 5.6. It reveals that the size distribution of MWNTs synthesized at ethylene molar fraction of 0.38, 0.50 and 0.63 are quite similar, conform to the log-normal distribution with the average (median) outer diameter of 7.3, 7.3 and 6.9 nm, respectively.

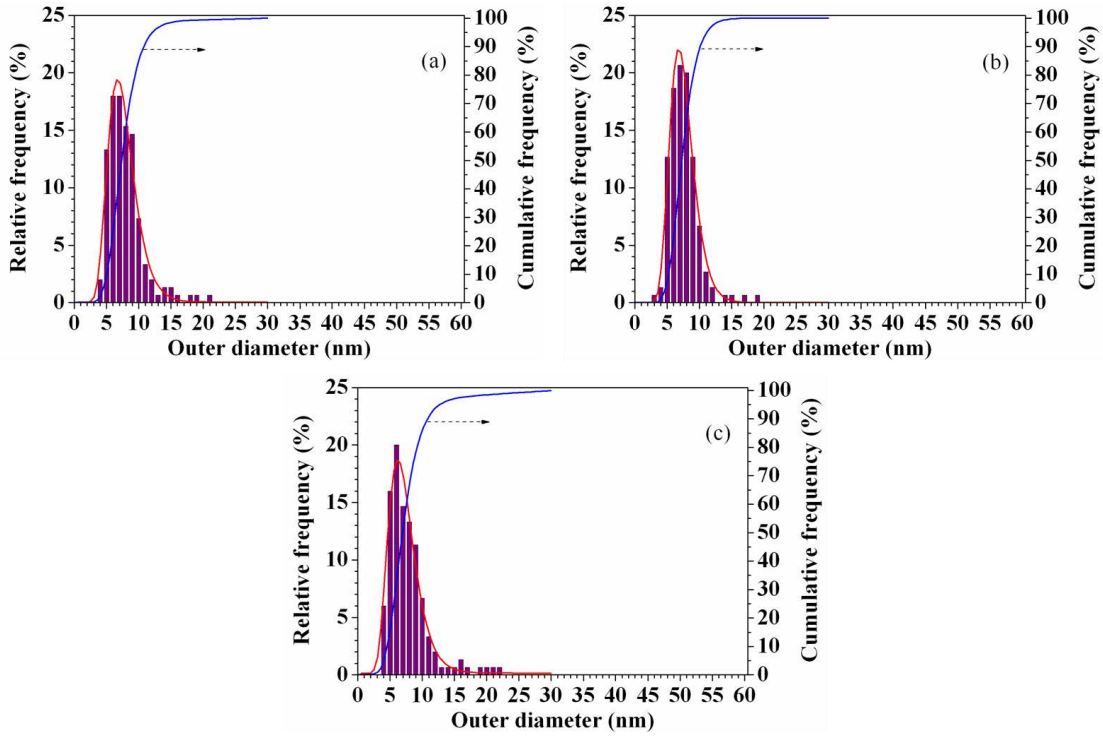


**Figure 5.6** Histograms of the diameter of MWNTs at various $C_2H_4$ molar fractions; (a) 0.38, (b) 0.50 and (c) 0.63 (temperature 600 $^{o}$C, 20 $g_{catalyst}$ , 60 minutes of run duration)

Form the size distribution of synthesized MWNTs as determined by TEM image analysis, it can be deduced that, over the temperature and ethylene molar fraction range studied, these two parameters do not significantly affect the MWNTs size distribution. The descriptive statistics obtained from TEM images analysis for product synthesized at various conditions were summarized in Table 5.6.

**Table 5.6** Summary of TEM analysis result.

| | Temperature ($^oC$) | Mode (nm) | Median (nm) | Mean (nm) | Standard deviation (nm) | Skewness |
|---|---|---|---|---|---|---|
| **Data Set [1]** | 550 | 6.7 | 7.3 | 7.6 | 2.14 | 0.87 |
| | | 35.1 | 35.1 | 35.1 | 4.37 | 0.00 |
| | 600 | 6.8 | 7.3 | 7.5 | 1.97 | 0.80 |
| | 650 | 7.5 | 8.1 | 8.5 | 2.57 | 0.94 |
| | 700 | 7.1 | 8.0 | 8.4 | 2.87 | 1.06 |
| | $C_2H_4$ molar fraction | Mode (nm) | Median (nm) | Mean (nm) | Standard deviation (nm) | Skewness |
| **Data Set [2]** | 0.38 | 6.7 | 7.3 | 7.6 | 2.25 | 0.91 |
| | 0.50 | 6.8 | 7.3 | 7.5 | 1.97 | 0.80 |
| | 0.63 | 6.2 | 6.9 | 7.2 | 2.32 | 1.00 |

[1] Evaluating the effect of temperature; 0.50 $C_2H_4$ molar fraction, 20 $g_{catalyst}$ and 60 minutes of run duration

[2] Evaluating the effect of ethylene molar fraction; temperature 600 $^oC$, 20 $g_{catalyst}$ and 60 minutes of run duration

In summary, MWNTs size were investigated by XRD and TEM with the aim of finding the most precise way to determine the average diameter and the size distribution of MWNTs. The distribution as determined by TEM and shown in a histogram very closely fites a log-normal profile. MWNTs sizes were also calculated from the line broadening of XRD reflections according to the Debye-Scherrer formula. The good agreement between the average MWNTs size measurements by XRD and TEM confirm the accuracy and reliability of these two technique. In the case of TEM imaging, it directly visualizes MWNTs as well as the presence of some considerably larger by-product, allows the estimation of the variation of MWNTs

diameter. As for XRD analysis, the simple Debye-Scherrer formula also yields rather accurate results for MWNTs size measurment without complicated sample preparation steps. Thus, these two techniques have their own advantages and can efficiently be applied in combination.

# CHAPTER VI

# KINETIC EVALUATION BY ON-LINE ANALYSIS

In this chapter, kinetic study and the evaluation of kinetic parameter from the reaction rate of MWNTs synthesis was performed via online gas analysis. The effluent gas was sampling every 10 minutes in order to investigate its composition. The amount of deposited carbon was calculated by carbon balance, equal to the difference between mass of carbon input and output. The exact amount of MWNTs was evaluated from their selectivity obtained from TGA. The experimental conditions mentioned in this chapter were the same as described in Table 5.2. It should be note that due to the partial agglomeration of bed occurred at the reaction temperature of 700 $^{o}$C, the experiment must be stoped at 48 minutes of run duration. Moreover, this phenomenon led to the separation of bed into 2 parts, namely “packed” and “fluidized” part, in this case, the selectivity of fluidized part was chosen as the ideal value for calculating MWNTs productivity at such temperature.

Under all conditions tested, the analysis of outlet gas shows that there are only four gaseous products in effluent stream viz ethane, methane, hydrogen and nitrogen while none of ethylene is observed, indicating to 100 % reaction conversion. MWNTs and gaseous species mentioned above can be generated via following chemical path ways (Phillipe et al., 2009);

$$C_2H_4 \rightarrow 2C + 2H_2 \quad (6.1)$$

$$C_2H_4 + H_2 \rightarrow C_2H_6 \quad (6.2)$$

$$C_2H_4 + H_2 \rightarrow 2CH_4 \quad (6.3)$$

The effect of temperature on MWNTs productivity was given in Figure 6.1. It clearly appears that in the temperature range studied, MWNTs productivity significantly increases with time and temperature. In detail, the considerable increment of MWNTs productivity appears at two temperature ranges. The first one, occurred between 600 $^{o}$C and 650 $^{o}$C, comes from the rise in MWNTs selectivity (32.6 % and 60.2 % for 600 $^{o}$C and 650 $^{o}$C, respectively) while mass of deposited carbon is almost constant (for example, 10.3 g and 10.8 g at 40 minutes for 600 $^{o}$C and 650 $^{o}$C, respectively). The difference in MWNTs selectivity with unchanged mass of deposited carbon indicates that the temperature of 600 $^{o}$C is just enough to drive the dissociation of ethylene but not for MWNTs formation while the temperature of 650 $^{o}$C is sufficient for both ethylene dissociation or MWNTs formation, so the product obtained at 600 $^{o}$C is mainly amorphous carbon which grows easier than MWNTs, resulting in a quite low MWNTs selectivity. On the other hand, the second significant increment of MWNTs productivity, occurred between 675 $^{o}$C and 700 $^{o}$C, is caused by the increment of deposited carbon (for instance, 11.6 g and 14.6 g at 40 minutes for 675 $^{o}$C and 700 $^{o}$C, respectively) while MWNTs selectivity is quite equal (60.4% and 65.4% for 675 $^{o}$C and 700 $^{o}$C, respectively). The best explanation of the second increment of MWNTs was obtained from the evaluation of ethane productivity, as demonstrated in Figure 6.2. It was found that ethane productivity

tended to decrease with an increase in temperature, in particular, the ethane productivity at 700 $^{o}$C was dramatically lower than the others. According to some authors (Gulino et al., 2005; Philippe et al., 2009), a sharp decrease of ethane productivity at high temperature is due to the fact that ethane, which is more thermally stable than ethylene, can be decomposed and providing supplementary active carbon for MWNTs formation, that is why the highest amount of deposited carbon could be achieved at 700 $^{o}$C.

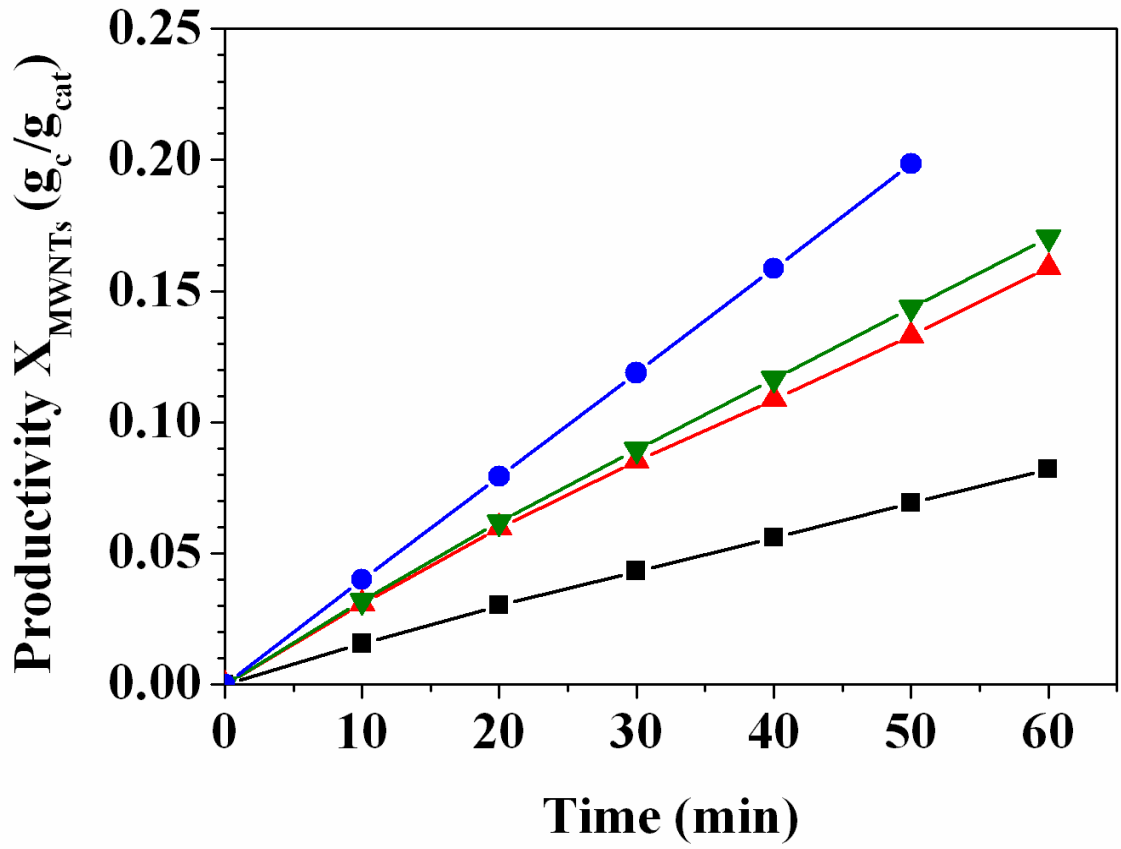


**Figure 6.1** Plot of MWNTs productivity at various times and temperatures

■ 600 $^{o}$C ▲ 650 $^{o}$C ▼ 675 $^{o}$C ● 700 $^{o}$C

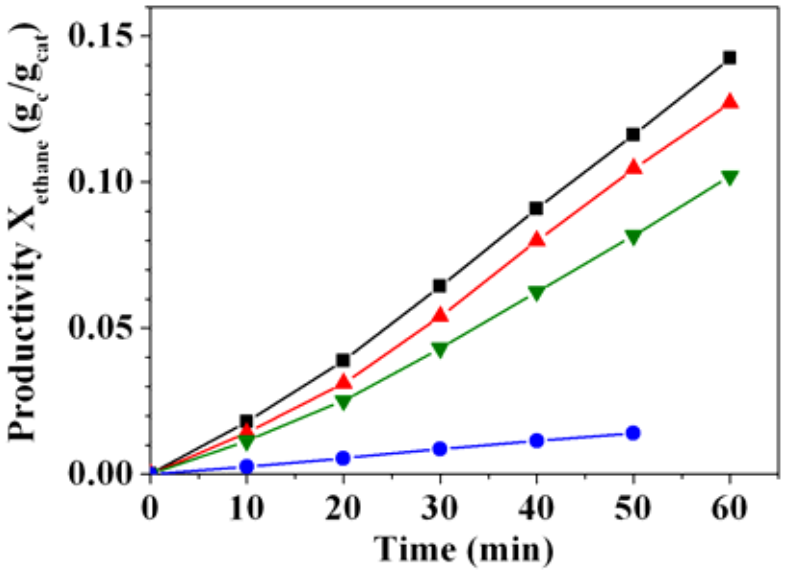


**Figure 6.2** Plot of ethane productivity at various times and temperatures

■ 600 °C ▲ 650 °C ▼ 675 °C ● 700 °C

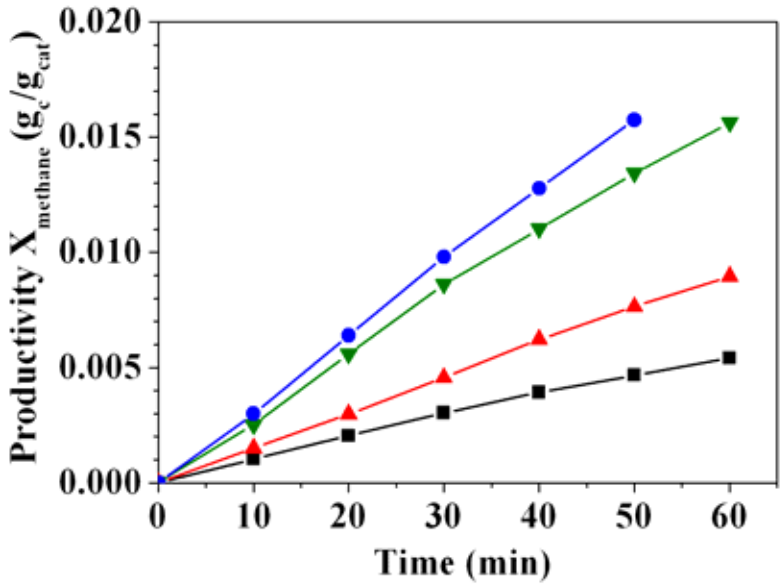


**Figure 6.3** Plot of methane productivity at various times and temperatures

■ 600 °C ▲ 650 °C ▼ 675 °C ● 700 °C

Finally, for the methane production as represented in Figure 6.3, it seems to increase with time and temperature. This can be concluded that methane does not react on cobalt catalyst to produce MWNTs in the temperature range studied owing to its thermal stability. The decomposition of methane at high temperatures especially, above 800 $^{o}$C has been reported elsewhere (Cassell et al., 1999; Philippe et al., 2009; Sivakumar et al., 2010). It is noteworthy that methane productivity is very low in comparison with each other and is almost negligible. The kinetic of the reactions were investigated by an Arrhenius law:

$$ln\ (dX/dt) = ln(k_o) - E_a/RT \qquad (6.4)$$

where $dX/dt$ is the rate of productivity observed from slope of productivity at interested time, $k_0$ is the apparent pre-exponential coefficient and $E_a$ is the apparent activation energy of reaction. Here, the kinetic parameters of MWNTs, ethane and methane production at the initial times (t=0) were evaluated. By plot of ln ($dX/dt$) versus reciprocal of temperature (in Kelvin), the activation energy of reaction and the apparent pre-exponential coefficient could be deduced from slope and Y-intercept.

Arrhenius plots for MWNTs, ethane and methane production were given in Figure 6.4, 6.5 and 6.6, respectively while the kinetic parameters at initial time of experiment were summarized in Table 6.1. In case of MWNTs production, $E_a$ is equal to 65.3 kJ•mol$^{-1}$ and the pre-exponential coefficient is 13.21 $g_C$•$g_{cata}^{-1}$•min$^{-1}$. For ethane production, due to the fact that ethane is catalytically decomposed in the temperature range studied, thus the Arrhenius plot of ethane production lead to a negative activation energy which is called as "deactivation energy ($E_d$)" and is found to be -3 .8 kJ•mol$^{-1}$ while the pre-exponential coefficient is 7.58 x 10$^{-6}$$g_C$•$g_{cata}^{-1}$•min$^{-1}$.

It should be noted that due to the deviation form a linear trend, the data point obtained at 700 $^{o}$C is not taken in Arrhenius plot, this may reduce the reliability of kinetic evaluation of ethane production. Finally, for methane production, $E_a$ is 78.5 kJ•mol$^{-1}$ and the pre-exponential coefficient is 4.87 $g_C$•$g_{cata}^{-1}$•min$^{-1}$.

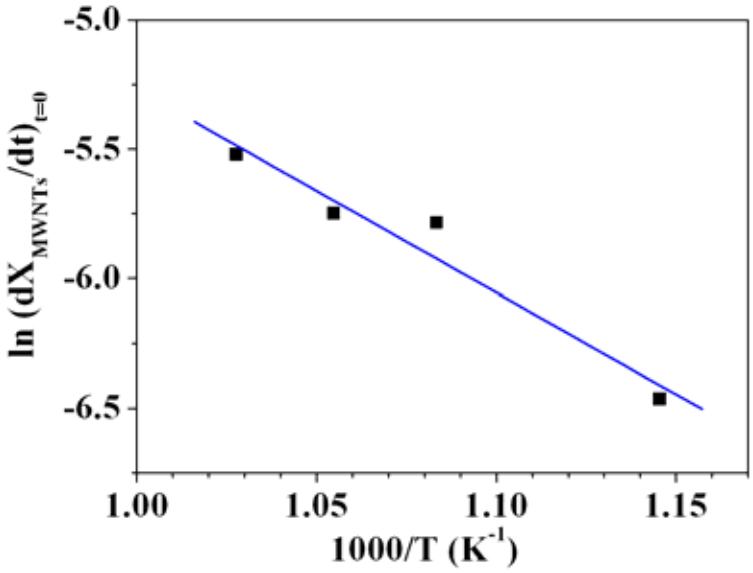


**Figure 6.4** Arrhenius plot of MWNTs production for kinetic evaluation

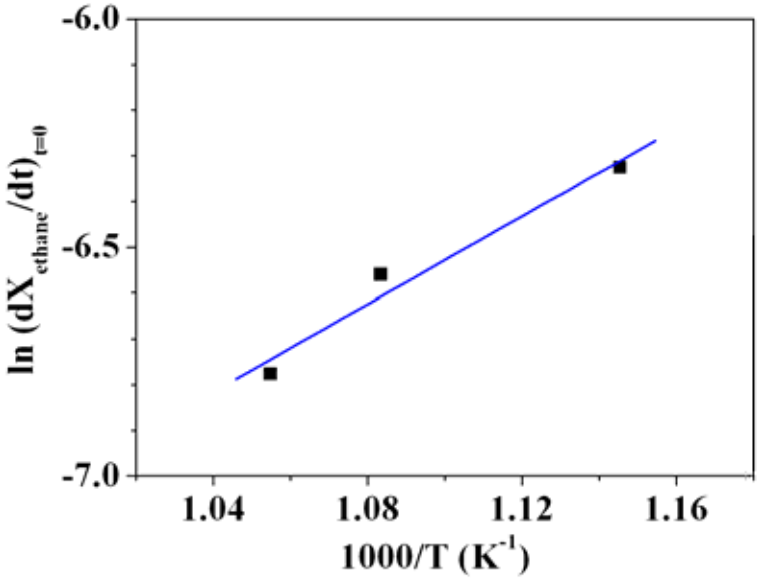


**Figure 6.5** Arrhenius plot of ethane productivity for kinetic evaluation

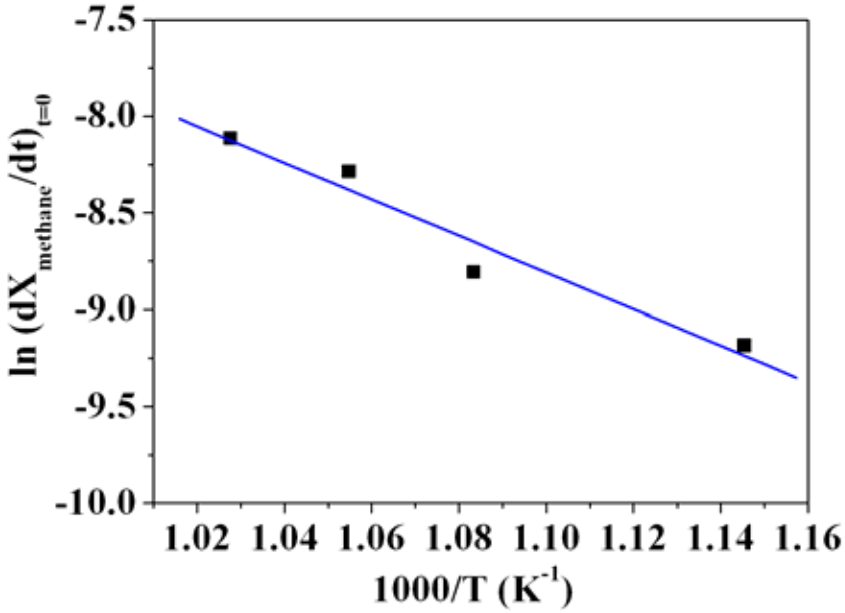


**Figure 6.6** Arrhenius plot of methane productivity for kinetic evaluation

**Table 6.1** Evaluation of kinetic parameter

| Product | Slope | Y-intercept | $R^2$ | $E_{a,t=0}$ ($kJ \cdot mol^{-1}$) | $k_{0,t=0}$ ($g_C \cdot g_{cata}^{-1} \cdot min^{-1}$) |
|---|---|---|---|---|---|
| MWNTs | -7.851 | 2.581 | 0.974 | 65.3 | 13.21 |
| Ethane | 4.783 | -11.790 | 0.983 | -39.8* | 7.58 E-6 |
| Methane | -9.448 | 1.584 | 0.974 | 78.5 | 4.87 |

* Deactivation energy ($E_d$)

Here, it should be elaborated on the quite low $E_a$ for MWNTs production. Many scientists have reported the growth of MWNTs based on vapor-solid-solid model ( ) as the activation energy of M Ts growing was close to that of carbon diffusion into solid metal, 30 $kJ \cdot mol^{-1}$ for Fe catalyst and 150 $kJ \cdot mol^{-1}$ for Co catalyst (Ramirez et al., 1999; Pirard et al., 2007; Philippe et al., 2009) which is

inconsistent with the value obtained in this work. However, in case of vapor-liquid-solid model (VLS), the activation energy of carbon diffusion into liquid Co reported by Zhukov (Zhukov et al., 2010) was 58.74 kJ•mol$^{-1}$ which quite conform to the apparent activation energy for MWNTs growing of 65.3 kJ•mol$^{-1}$. Considering the uncertainty of the kinetic parameter estimation, the difference between $E_a$ obtained in this work and the value reported by Zhukov is somewhat acceptable. Due to the coincidence of the appearance activation energy of MWNTs formation obtained in this work and the activation energy of carbon diffusion into liquid Co, it is possible to assume that carbon diffusion into liquid Co is a rate determining step. Other evidences that support this idea are obtained from the observation of cobalt nanoparticle melting temperature by Homma and his co-workers (Homma et al., 2003) as cobalt nanoparticles with average size of 30 nm started to melt at 600 $^{o}$C under carburizing atmosphere and 650 $^{o}$C under inert atmosphere. They suggested that the dramatically decrease in melting temperature of this specie was because of their high surface to volume ratio and the formation of eutectic compound namely cobalt carbide. Moreover, the TEM images of MWNTs synthesized in this thesis also reveal the presence of molten particle as the drop-shape encapsulated nanoparticle, as shown in Figure 6.7. The presence of encapsulated nanoparticle as an impurity in MWNTs indicates to a weak metal-substrate interaction (low adhesion energy) which directly relates to the nature of metal catalyst and substrate. The formation of encapsulated nanoparticles can be avoided by using low temperature CVD process such as Plasma-enhanced CVD or microwave-assisted CVD since its low operation temperature can diminish the melting of metal catalyst (Mostofizadeh et al., 2010). Moreover, the catalyst preparation by sol-gel method can also prevent the formation of encapsulated

nanoparticles due the strong metal-substrate interactions that can improve the catalyst consistency (Tran et al, 2007).

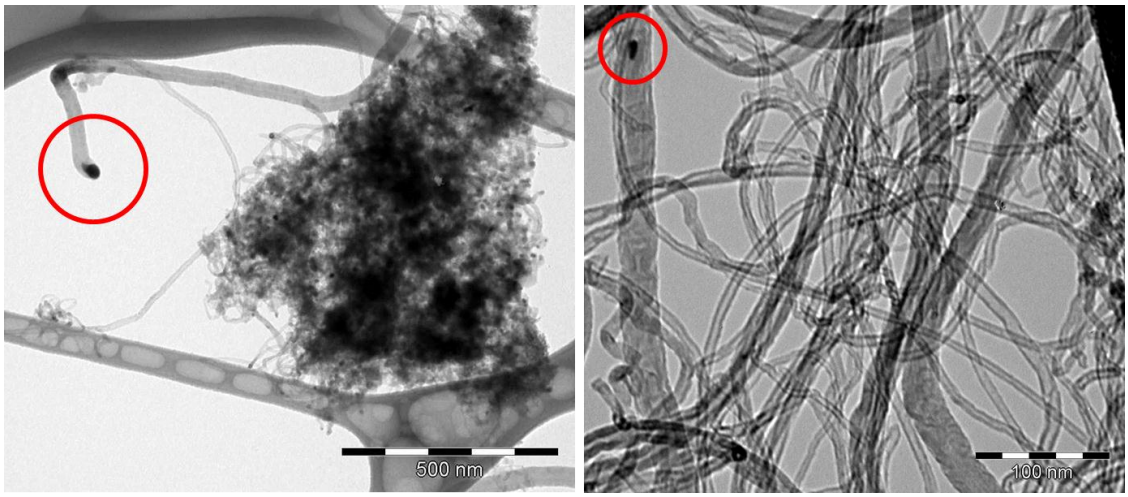


**Figure 6.7** TEM images of MWNTs synthesized at 700 $^{o}$C, 0.50 $C_2H_4$ molar fraction, 20 $g_{catalyst}$ and 60 minutes of run duration

# CHAPTER VII

# CONCLUSIONS

In this thesis, the effects of temperature and ethylene molar fraction on MWNTs synthesis were investigated. The results showed that these two parameters significantly affect the solid carbon conversion, MWNTs selectivity and type of product. For the temperature range of 550 $^{o}$C to 700 $^{o}$C, the reaction temperature of 550 $^{o}$C resulted in the lowest solid carbon conversion due to insufficient external energy to drive the precursor dissociation. Moreover, MWNTs selectivity was low due to the presence of CNFs as main product. However, the increase in reaction temperature above 650 $^{o}$C causes the deactivation of catalyst because of the presence of excessive amorphous carbon on catalyst surface. For the ethylene molar fraction range of 0.38 to 0.50, the MWNTs formation showed the positive order dependence on ethylene molar fraction, whereas the further raise in ethylene molar fraction led to catalyst poisoning. The highest rate of MWNTs productivity of 0.45 $g_{MWNTs} \bullet g_{cata}^{-1}$ could be achieved at the reaction temperature of 600 $^{o}$C, ethylene molar fraction of 0.50, 60 minutes duration and 20g of catalyst.

In terms of MWNTs quality, the results revealed that the reaction temperature had a significant effect on MWNTs crystallinity as observed by XRD. The degree of graphitization increased with the reaction temperature increment. Over tested conditions, the average outer diameter of synthesized MWNTs was approximately 7 nm.

The analysis of effluent stream showed that ethane could deposit to from MWNTs at the reaction temperature above 675 $^{o}$C, while methane did not react over the temperature range studied. The apparent activation energy and pre-exponential coefficient for MWNTs synthesis extracted form Arrenius plot were 65.3 kJ•mol$^{-1}$ and 13.21 $g_C$•$g_{cata}^{-1}$•min$^{-1}$, respectively. Considering the apparent activation energy, the diffusion of carbon into liquid cobalt was rate determining step.

# NOMENCLATURE

| | |
|---|---|
| $a$ | Kinetic order |
| $C$ | Solid carbon conversion (%) |
| $d\ (0\ 0\ 2)$ | Carbon (0 0 2) interplanar distance (Å) |
| $d_0$ | Carbon (0 0 2) interplanar distance of HOPG (Å) |
| $\Delta d$ | Difference in the carbon (0 0 2) interplanar distance (Å) |
| $D_{[4,3]}$ | Volume weighted mean diameter of particle (μm) |
| $D_{agglomerate}$ | Mean diameter of M Ts agglomerate (μm) |
| $D_{Co}^{0}$ | Mean crystallite size of $Co^0$ (nm) |
| $D_{Co_3O_4}$ | Mean crystallite size of $Co_3O_4$ (nm) |
| $E$ | Elastic modulus (GPa) |
| $E_a$ | Apparent activation energy of reaction ($kJ \cdot mol^{-1}$) |
| $g$ | Degree of graphitization (%) |
| $H_0$ | Initial bed height (cm) |
| $I_D$ | Intensity of D band (a.u.) |
| $I_G$ | Intensity of G band (a.u.) |
| $k_0$ | Apparent pre-exponential coefficient |
| $R$ | Reaction conversion (%) |
| $Re_{mf}$ | Reynolds number at minimum fluidization velocity |
| $S$ | Selectivity (%) |
| $T_o$ | Temperature at the maximum in the weight loss rate ($^oC$) |
| $U$ | uperficial velocity ($cm \cdot s^{-1}$) |

| | |
|---|---|
| $U_{mf}$ | Minimum fluidization velocity ($cm \bullet s^{-1}$) |
| $X$ | Productivity ($g_C \bullet g_{Cata}^{-1}$) |

**Greek symbols**

| | |
|---|---|
| $\sigma$ | Stress (GPa) |
| $\varepsilon$ | Microstrain (%) |
| $\rho_b$ | Untapped bulk density ($g \bullet cm^{-1}$) |
| $\rho_f$ | Density of fluidizing fluid ($g \bullet cm^{-1}$) |
| $\rho_g$ | Grain density ($g \bullet cm^{-1}$) |

# REFFERENCES


Ahmed, M.S. Characterization of carbon nanotubes grown by chemical vapour deposition. Master's Thesis, Materials science program, Faculty of cience, University of Ontario institute of technology, 2009.

Anantram, M.P., and Leonard, F. Physics of carbon nanotube electronic devices. Reports on Progress in Physics 69 (2006): 507-561.

Ando, T. The electronic properties of graphene and carbon nanotubes. NPG Asia Materials 1 (2009): 17-21.

Ando, Y., Zhao, X., Sugai, T., and Kumar, M. Growing carbon nanotubes. Materials today 7 (2004): 22-29.

Arepalli, S. et al. Protocol for the characterization of single-wall carbon nanotube material quality. Carbon 42 (2004): 1,783–1,791.

Avouris, P. Molecular Electronics with Carbon Nanotubes. Accounts of Chemical Research 35 (2002): 1,026-1,034.

Baker, R.T.K., and Waite, R. J. Formation of carbonaceous deposits from the platinum-iron catalyzed decomposition of acetylene. Journal of Catalysis 37 (1975): 101-105.

Baker, R.T.K., Barber, M.A., Harris, P.S., Feates, F.S., and Waite, R.J. Nucleation and growth of carbon deposits from the nickel catalyzed decomposition of acetylene. Journal of Catalysis 26 (1972): 51-62.

Baker, R.T.K., Harris, P.S., Thomas, R.B., and Waite, R.J. Formation of filamentous carbon from iron, cobalt and chromium catalyzed decomposition of acetylene. Journal of Catalysis 30 (1973): 86-95.

Batista, M.S., Santos, R.K.S., Assaf, E.M., Assaf, J.M., and Ticianelli, E.A. Characterization of the activity and stability of supported cobalt catalysts for the steam reforming of ethanol. Journal of Power Sources 124 (2003): 99–103.

Belin, T., and Epron, F. Characterization methods of carbon nanotubes: A review. Materials Science and Engineering B 119 (2005): 105-118.

Berber, S., Kwon, Y.K., and Tomanek, D. Unusually high thermal conductivity of carbon nanotubes. Physical Review Letters 84 (2000): 4,613-4,616.

Bernaerts, D., Amelinckx, S., Lambin, P., and Lucas, A.A. The diffraction space of circular and polygonized multishell nanotubules. Applied Physics A 67 (1998): 53-64.

Bethune, D.S. et al. Cobalt-catalysed growth of carbon nanotubes with single-atomic-layer walls. Nature 363 (1993): 605-607.

Bladh, K., Falk, L.K.L., and Rohmund, F. On the iron-catalysed growth of single-walled carbon nanotubes and encapsulated metal particles in the gas phase. Applied Physics A 70 (2000): 317-322.

Bower, C., Zhou, O., Zhu, W., Werder, D.J., and Jin, S. Nucleation and growth of carbon nanotubes by microwave plasma chemical vapor deposition. Applied Physics Letters 77 (2000): 2,767-2,769.

Bronikowski, M.J. CVD growth of carbon nanotube bundle arrays. Carbon 44 (2006): 2,822–2,832.

Brown, S.D.M. et al. Anti-Stokes Raman spectra of single-walled carbon nanotubes. Physical Review B 61 (2000): R5,137-R5,140.

Brukh, R., and Mitra, S. Mechanism of carbon nanotube growth by CVD. Chemical Physics Letters 424 (2006): 126-132.

Burghard, M. Electronic and vibrational properties of chemically modified single-wall carbon nanotubes. Surface Science Reports 58 (2005): 1-109.

Burian, A., Dore, J., Fischer, H., and Sloan, J. Structural studies of multiwall carbon nanotubes by neutron diffraction. Physical Review B 59 (1999): 1,665-1,668.

Cao, A., Xu, C., Liang, J., Wu, D., and Wei, B. X-ray diffraction characterization on the alignment degree of carbon nanotubes. Chemical Physics Letters 344 (2001): 13-17.

Cassell, A.M., Raymakers, J.A., Kong, J., and Dai, H. Large scale CVD synthesis of single-walled carbon nanotubes. Journal of Physical Chemistry B 103 (1999): 6,484-6,492.

Castellano, J.A. Handbook of Display Technology. San Diego: Academic Press, 1992.

Chandra, B. Synthesis and Electronic Transport in Known Chirality Single Wall Carbon Nanotubes. Doctoral dissertation, Graduate School of Arts and Sciences, Columbia University, 2009.

Charlier, A., McRae, E., Heyd, R., Charlier, M.F., and Moretti, D. Classification for double-walled carbon nanotubes. Carbon 37 (1999): 1,779-1,783.

Cheng, Q. Dispersion of Single-Walled Carbon Nanotubes in Organic Solvents. Doctoral dissertation, School of Physics, Dublin Institute of Technology, 2010.

Cheung, C.L., Kurtz, A., Park, H., and Lieber, C.M. Diameter-controlled synthesis of carbon nanotubes. Journal of Physical Chemistry B 106 (2002): 2,429-2,433.

Ciambelli, P., Sannino, D., Sarno, M., Fonseca, A., and Nagy, J.B. Selective formation of carbon nanotubes over Co-modified beta zeolite by CCVD. Carbon 43 (2005): 631–640.

Colbert, D.T. et al. Growth and sintering of fullerene nanotubes. Science 266 (1994): 1,218-1,222.

Collins, P.G., and Avouris, P. Nanotubes for Electronics. Scientific American (2000): 67- 69.

Corrias, M., Kihn, Y., Kalck, Ph., and Serp, Ph. CVD from ethylene on cobalt ferrite catalysts: The effect of the support. Carbon 43 (2005): 2,820–2,823.

Costa, S., Borowiak-Palen, E., Kruszyñska, M., Bachmatiuk, A., and Kaleńczuk, R.J. Characterization of carbon nanotubes by Raman spectroscopy. Materials Science-Poland 26 2 (2008): 433-442.).

Dai, H.J., Hafner, J.H., Rinzler, H.G., Colbert, D.T., and Smalley, B.E. Nanotubes as nanoprobes in scanning probe microscopy. Nature 384 (1996): 147-150.

Danafar, F., Fakhru'l-Razi, A., Mohd Salleh, M.A., and Awang Biak, D.R. Influence of catalytic particle size on the performance of fluidized-bed chemical vapor deposition synthesis of carbon nanotubes. Chemical Engineering Research and Design 89 (2011): 214–223.

Demczyk, B.G. et al. Direct mechanical measurement of the tensile strength and elastic modulus of multi-walled carbon nanotubes. Materials Science and Engineering A 334 Issues 1–2 (2002): 173–178.

Ding, F., Bolton, K., and Rosén, A. Nucleation and Growth of Single-Walled Carbon Nanotubes: A Molecular Dynamics Study. Journal of Physical Chemistry B 108 (2004): 17369-17377.

Dresselhaus, M.S., Dresselhaus, G., and Avouris, P. Carbon Nanotubes Synthesis, Structure, Properties and Application. Topics in Applied Physics vol. 80: Springer Publication, 2001.

Dresselhaus, M.S., Dresselhaus, G., and Jorio, A. Unusual properties and structure of carbon nanotubes. Annual Review of Material Research 34 (2004): 247-278.

Ebbesen, T.W., and Ajayan, P.M. Large-scale synthesis of carbon nanotubes. Nature 358 (1992): 220- 222.

Ferlauto, A.S. et al. Chemical vapor deposition of multi-walled carbon nanotubes from nickel/yttria-stabilized zirconia catalysts. Applied Physics A 84 (2006): 271–276.

Fonseca, A., Hernadi, K., Nagy, B.J., Bernaerts, D., and Lucas, A.A. Optimization of catalytic production and purification of buckytubes. Journal of Molecular Catalysis A: Chemical 107 (1996): 159-168.

Geldart, D. Types of gas fluidization. Powder Technology 7 (1973): 249-304.

Gulino, G. et al. $C_2H_6$ as an active carbon source for a large scale synthesis of carbon nanotubes by chemical vapour deposition. Applied Catalysis A: General 279 (2005): 89–97.

Guo, T. et al. Self-Assembly of Tubular Fullerenes. Journal of Physical Chemistry 99 (1995): 10,694-10,697.

Hafner, J.H. et al. Catalytic growth of single-wall carbon nanotubes from metal particles. Chemical Physics Letters 296 (1998): 195-202.

Hao, Y., Qunfeng, Z., Fei, W., Weizhong, Q., and Guohua, L. Agglomerated CNTs synthesized in a fluidized bed reactor: Agglomerate structure and formation mechanism. Carbon 41 (2003): 2,855–2,863.

Harper, C.A. Electronic Assembly Fabrication. Electronic Packaging and lnterconnection Series. New York: McGraw-Hill, 2002.

Harutyunyan, A.R., Tokune, T and Mora, E. Liquid as a required catalyst phase for carbon single-walled nanotube growth. Applied Physics Letters 87 (2005): 51,919-51,921.

Hata, K. et al. Water-Assisted Highly Efficient Synthesis of Impurity-Free Single-Walled Carbon Nanotubes. Science 306 (2004): 1,362-1,364.

Hernadi, K., Fonseca, A., Nagy, J.B., Siska, A., and Kiricsi, I. Production of nanotubes by the catalytic decomposition of different carbon-containing compounds. Applied Catalysis A: General 199 (2000): 245-255.

Homma, Y., Kobayashi, Y., and Ogino, T. Role of transition metal catalysts in single-walled carbon nanotube growth in chemical vapor deposition. Journal of Physical Chemistry B 107 (2003): 12,161-12,164.

Hone, J., Whitney, M., Piskoti, C., and Zettl, A. Thermal conductivity of single-walled carbon nanotubes. Physical Review B 59 (1999): R2,514-R2,516.

Hong, S., and Myung, S. Nanotube Electronics: A flexible approach to mobility. Nature Nanotechnology 2 (2007): 207–208.

Huang, L. et al. Cobalt ultrathin film catalyzed ethanol chemical vapor deposition of single-walled carbon nanotubes. Journal of Physical Chemistry B 110 (2006): 11,103-11,109.

Huang, L., Wind, S.J., and O'Brien, S.P. Controlled growth of single-walled carbon nanotubes from an ordered mesoporous silica template. Nano Letters 3 (2003): 299-303.

Huang, S., Woodson, M., Smalley, R., and Liu, J. Growth Mechanism of Oriented Long ingle alled Carbon anotubes Using “Fast-Heating” Chemical apor Deposition Process. Nano Letters 4 (2004): 1,025-1,028.

Huang, Z.P. et al. Effect of nickel, iron and cobalt on growth of aligned carbon nanotubes. Applied Physics A 74 (2002): 387-391.

Huang, Z.P. et al. Growth of highly oriented carbon nanotubes by plasma-enhanced hot filament chemical vapor deposition. Applied Physics Letters 73 (1998): 8,345-8,347.

Iijima, S. Helical microtubules of graphitic carbon. Nature 354 (1991): 56-58.

Iijima, S., and Ichihashi, T. Single-shell carbon nanotubes of 1-nm diameter. Nature 363 (1993): 603-605.

Ivanov, V. et al. The study of carbon nanotubules produced by catalytic method. Chemical Physics Letters 223 (1994): 329-335.

Javey, A., Guo, J., Wang, Q., Lundstrom, M., and Dai, H. Ballistic Carbon Nanotube Transistors. Nature 424 (2003): 654-657.

Jiang, N. et al. Carbon nanofibers synthesized by decomposition of alcohol at atmospheric pressure. Applied Physics Letters 81 (2002): 526-528.

Karimi, A. et al. Fischer-Tropsch synthesis over ruthenium-promoted $Co/Al_2O_3$ catalyst with different reduction procedures. Journal of Natural Gas Chemistry 19 (2010): 503–508.

Kiang, C.-H., Endo, M., Ajayan, P.M., Dresselhaus, G., and Dresselhaus, M.S. Size effects in carbon nanotubes. Physical Review Letters 81 (1998): 1,869–1,872.

Kis, A. Mechanical properties of mesoscopic objects. Doctoral dissertation, Section de physique, Institut de physique de la matière complexe, École Polytechnique Fédérale de Lausanne, 2003.

Klinke, C., Bonard, J.-M., and Kern, K. Comparative study of the catalytic growth of patterned carbon nanotube films. Surface Science 492 (2001): 195-201.

Kroto, H.W., Heath, J.R., O'Brien, S.C., Curl, R.F., and Smalley, R.E. C60: Buckminsterfullerene. Nature 318 (1985): 162-163.

Kumar, M. Carbon Nanotube Synthesis and Growth Mechanism. Dr. Siva Yellampalli, Carbon Nanotubes - Synthesis, Characterization, Applications, 147-170: InTech, 2011.

Kunii, D., and Levenspiel, O. Fluidzation Engineering. 2nd edition. Massachusetts: Butterworth-Heinemann, 1991.

Kuo, D.H., Su, M.Y., and Chen, W.R. Organized carbon-nanotubes grown by chemical vapor deposition with a gas-phase catalyst of iron pentacarbonyl. Proceedings of 5th IEEE Conference on Nanotechnology 2 (2005): 681-684.

Lambin, P., Loiseau, A., Culot, C., and Biro, L.P. Structure of carbon nanotubes probed by local and global probes. Carbon 40 (2002): 1,635-1,648.

Lee, Y.-J., Park, J.-Y., Jun, K.-W., Bae, J.W., and Sai Prasad, P.S. Controlled nanocrystal deposition for higher degree of reduction in $Co/Al_2O_3$ catalyst. Catalysis Letters 130 (2009): 198–203.

Li, J., Papadopoulos, C., Xu, J.M., and Moskovits, M. Highly-ordered carbon nanotubes arrays for electronics applications. Applied Physics Letters 75 (1999): 367-369.

Li, W.Z., Wen, J.G., and Ren, Z.F. Effect of temperature on growth and structure of carbon nanotubes by chemical vapor deposition. Applied Physics A 74 (2002): 397-402.

Liu, M., and Cowley, J.M. Structures of the helical carbon nanotubes. Carbon 32 (1994): 393-403.

Liu, X. Synthesis of multi-walled carbon nanotubes by chemical vapour deposition and post-synthesis treatment by dielectrophoresis. Doctoral dissertation, Department of Chemistry, Faculty of Science, Victoria University of Wellington, 2006.

Mahan, A.H. et al. Hot wire chemical vapor deposition of isolated carbon single-walled nanotubes. Applied Physics Letters 81 (2002): 4,061-4,063.

Maire, J., and Mering, J. Graphitization of soft carbons. In: Walker PL, editor, Chemistry and physics of carbon, vol. 6, New York: Marcel Dekker; 1970, pp. 125-190.

McCaldin, S., Bououdina, M., Grant, D.M., and Walker, G.S. The effect of processing conditions on carbon nanostructures formed on an iron-based catalyst. Carbon 44 (2006): 2,273–2,280.

Meyyappan, M. Carbon Nanotubes: Science and Applications. Florida USA: CRC press, 2005.

Moisala, A., Nasibulin, A.G., and Kauppinen, E.I. The role of metal nanoparticles in the catalytic production of single-walled carbon nanotubes—a review. Journal of Physics: Condensed Matter 15 (2003): S3011-S3035.

Monthioux, M., and Kuznetsov, V.L. Who should be given the credit for the discovery of carbon nanotubes? Carbon 44 (2006): 1,621-1,623.

Morançais, A. et al. A parametric study of the large production of multi-walled carbon nanotubes by fluidized bed catalytic chemical vapor deposition. Carbon 45 (2007): 624-635.

Mostofizadeh, A., Li, Y., Song, B., and Huang, Y. Synthesis, Properties, and Applications of Low-Dimensional Carbon-Related Nanomaterials. Journal of Nanomaterials 2011 (2011): 1-21.

Müller, A. Spectroscopic Study of Polymer Composite Material based on Functionalized Carbon Nanotubes and Characterization of Individual Carbon Nanotubes for Composites Synthesis. Master's Thesis, Division of Physics, Department of Applied Physics and Mechanical Engineering, Luleå University of Technology, 2009.

Nagaraju, N., Fonseca, N., Konya, Z., and Nagy, J.B. Alumina and silica supported metal catalysts for the production of carbon nanotubes. Journal of Molecular Catalysis A: Chemical 181 (2002) 57-62.

Nerushev, O.A., Sveningsson, M., Falk, L.K.L., and Rohmund, F. Carbon nanotube films obtained by thermal chemical vapour deposition. Journal of Materials Chemistry 11 (2001): 1,122-1,132.

Newbury, D.E., and Williams, D.B. The electron microscope: the materials characterization tool of the millennium. Acta materialia 48 (2000): 323-346.

O'Connell, M.J. Carbon nanotubes: Properties and applications. Boca Raton: CRC Press, Taylor & Francis Group, 2006.

Patole, S.P., Alegaonkar, P.S., Lee, J.H., and Yoo, J.B. Water-assisted synthesis of carbon nanotubes: Acetylene partial pressure and height control. Europhysics Letters 81 (2008): 38002 1-6.

Paul, S., and Samdarshi, S.K. A green precursor for carbon nanotube synthesis. New Carbon Materials 26 (2011): 85–88.

Philippe, R. et al. Catalytic Production of Carbon Nanotubes by Fluidized-Bed CVD. Chemical Vapor Deposition 13 (2007): 447–457.

Philippe, R. et al. Kinetic Study of Carbon Nanotubes Synthesis by Fluidized Bed Chemical Vapor Deposition. AIChE Journal 55 (2009): 450-464.

Pirard, S.L., Douven, S., Bossuot, C., Heyen, G., and Pirard, J.-P. A kinetic study of multi-walled carbon nanotube synthesis by catalytic chemical vapor deposition using a Fe-Co/$Al_2O_3$ catalyst. Carbon 45 (2007): 1,167-1,175.

Radushkevich, L.V., and Lukyanovich, V.M. O strukture ugleroda, obrazujucegosja pri termiceskom razlozenii okisi ugleroda na zeleznom kontakte. Zurn Fisic Chim 26 (1952): 88-95.

Rao, A.M. et al. Diameter-selective Raman scattering from vibrational modes in carbon nanotubes. Science 275 (1997): 187-191.

Reznik, D., Olk, C., Neumann, A., and Copley, J. X-ray powder diffraction from carbon nanotubes and nanoparticles. Physical Review B 52 (1995): 116-124.

Saito, R., Dresselhaus, G., and Dresselhaus, M.S. Physical properties of carbon nanotubes. London: Imperial College Press, 1998.

Saito, Y., Nishikubo, K., Kawabata, K., and Matsumoto, T. Carbon nanocapsules and single layered nanotubes produced with platinum group metals by arc discharge method. Journal of Applied Physics 80 (1996): 3,062-3,067.

Saito, Y., Yoshikawa, T., Bandow, S., Tomita, M., and Hayashi, T. Interlayer spacings in carbon nanotubes. Physical Review B 48 (1993): 1,907-1,909.

Salvetat, J.-P. et al. Mechanical properties of carbon nanotubes. Applied Physics A 69 (1999): 255–260.

Schanke, D. et al. Study of Pt-promoted cobalt CO hydrogenation catalysts. Journal of Catalysis 156 (1995): 85-95.

Sivakumar, V.M., Abuduliah, A.Z., Mohamed, A.R., and Chai, S.P. Studies on carbon nanotubes synthesis via methane CVD process using $CoO_X$ as catalyst on carbon supports. Digest Journal of Nanomaterials and Biostructures 5 (2010): 691 –698.

Sivakumar1, V.M., Abdullah1, A.Z., Mohamed, A.R., and Chai, S.P. Optimized parameters for carbon nanotubes synthesis over Fe and Ni catalysts via methane CVD. Review Advance Materials Science 27 (2011): 25-30.

Stamatina I., et al., The synthesis of multi-walled carbon nanotubes (MWNTs) by catalytic pyrolysis of the phenol-formaldehyde resins. Physica E 37 (2007): 44–48.

Teo, B.K., Singh, C., Chhowalla, M., and Milne, I.W. Catalytic Synthesis of Carbon Nanotubes and Nanofibers. Encyclopedia of Nanoscience and Nanotechnology 1 (2004): 665-686.

Thostenson, E.T., Ren, Z.F., and Chou, T.W. Advances in the science and technology of carbon nanotubes and their composites: a review. Composites Science and Technology 61 (2001): 1,899-1,912.

Tibbetts, G.G. Why are carbon filaments tubular? Journal of Crystal Growth 66 (1984): 632-638.

Tran, K.Y., Heinrichs, B., Colomer, J.-F., Pirard, J.-P., and Lambert, S. Carbon nanotubes synthesis by the ethylene chemical catalytic vapour deposition (CCVD) process on Fe, Co, and Fe-Co/Al2O3 sol-gel catalysts. Applied Catalysis A: General 318 (2007): 63-69.

Tu, Y., Huang, Z.P., Wang, D.Z., Wen, J.G., and Ren, Z.F. Growth of aligned carbon nanotubes with controlled site density. Applied Physics Letters 80 (2002): 4,018-4,020.

Venegoni, D. et al. Parametric study for the growth of carbon nanotubes by catalytic chemical vapor deposition in a fluidized bed reactor. Carbon 40 (2002) 1,799-1,807.

Wagner, R.S., and Ellis, W.C. The vapor-liquid-solid mechanism of crystal growth and its application to silicon. Transactions of The Metallurgical Society of Aime 233 (1965): 1,053-1,064.

Wang, B.B. et al. Effects of the pressure on growth of carbon Nanotubes by plasma-enhanced hot filament CVD at low substrate temperature. Applied Surface Science 236 (2004): 6–12.

Wang, Y., Wei, F., Gu, G., and Yu, H. Agglomerated carbon nanotubes and its mass production in a fluidized-bed reactor. Physica B 323 (2002): 327–329.

Wang, Y., Wei, F., Luo, G., Yu, H., and Gu, G. The large-scale production of carbon nanotubes in a nano-agglomerate fluidized-bed reactor. Chemical Physics Letters 364 (2002): 568-572.

Webber, W.H., and Merlin, R. Raman Scattering in Materials Science. Springer Series in Materials Science volume 42. New York: Springer, 2000.

White, C.T., and Mintmire, J.W. Density of states reflects diameter in nanotubes. Nature 394 (1998): 29-30.

Xu, C., and Zhu, J. One-step preparation of highly dispersed metal-supported catalysts by fluidized-bed MOCVD for carbon nanotube synthesis. Nanotechnology 15 (2004): 1,671–1,681.

Yang, Q.H. et al. Direct growth of macroscopic fibers composed of large diameter SWNTs by CVD. Chemical Physics Letters 370 (2003): 274-279.

Yang, X. et al. Low-temperature synthesis of multi-walled carbon nanotubes over Cu catalyst. Materials Letters 72 (2012): 164–167.

Yeoh, W.M., Lee, K.Y., Chai, S.P., Lee, K.T., and Mohamed, A.R. Synthesis of high purity multi-walled carbon nanotubes over Co-Mo/MgO catalyst by the catalytic chemical vapor deposition of methane. New Carbon Materials 24 (2009): 119-123.

Yu, M.-F. Fundamental mechanical properties of carbon nanotubes: Current understanding and the related experimental studies. Journal of Engineering Materials and Technology 126 (2004): 271- 278.

Yu, Z.H., and Brus, L. Rayleigh and Raman scattering from individual carbon nanotube bundles. Journal of Physical Chemistry B 105 (2001): 1,123-1,134.

Zhang, G. et al. Ultra-high-yield growth of vertical single-walled carbon nanotubes: Hidden roles of hydrogen and oxygen. Proceedings of the National Academy of Science of United States of America 102 (2005): 16,141-16,145.

Zhang, W.D., Wen, Y., Tjiu, W.C., Xu, G.Q., and Gan, L.M. Growth of vertically aligned carbon-nanotube array on large area of quartz plates by chemical vapor deposition. Applied Physics A 74 (2002): 419-422.

Zhao, Q., Jiang, T., Li, C., and Yin, H. Synthesis of multi-wall carbon nanotubes by Ni-substituted (loading) MCM-41 mesoporous molecular sieve catalyzed pyrolysis of ethanol. Journal of Industrial and Engineering Chemistry 17 (2011): 218–222.

Zhao, W., Seo, D.N., Kim, H.T., and Kim, I.J. Characterization of multi-walled carbon nanotubes (MWNTs) synthesized by CCVD using zeolite template from acetylene. Journal of the Ceramic Society of Japan 118 (2010): 983-988.

Zheng, B. et al. Efficient CVD Growth of single-walled carbon nanotubes on surfaces using carbon monoxide precursor. Nano Letter 2 (2002): 895-898.

Zhu, L. et al. The growth of carbon nanotube stacks in the kinetics-controlled regime. Carbon 45 (2007): 344-348.

Zhu, W.Z., Miser, D.E., Chan, W.G., and Hajaligol, M.R. Characterization of multiwalled carbon nanotubes prepared by carbon arc cathode deposit. Materials Chemistry and Physics 82 (2003): 638-647.

# APPENDICES

# APPENDIX A

# CALCULATION OF MWNTS AGGLOMERATES MEAN DIAMETER

**A-1** Mean diameter of MWNTs agglomerates is calculated from Wen and Yu correlation;

$$Ar = \frac{\rho_f(\rho_p - \rho_f)gD^3}{\mu^2} \quad (1)$$

$$\mathrm{Re}_{mf} = (33.7^2 + 0.0408Ar)^{0.5} - 33.7 \quad (2)$$

$$Umf = \frac{\mathrm{Re}_{mf}\,\mu}{D\rho_f} \quad (3)$$

Where; $U_{mf}$ = Minimum fluidization velocity

$\mu$ = Viscosity of fluidizing fluid

D = Mean diameter of particle

$\rho_f$ = Density of fluidizing fluid

$\rho_p$ = Grain density of particle

Firstly, it is necessary to assume the value of mean diameter for calculation of Archimedes number from equation 1. Then, calculate minimum fluidization Reynolds number from equation 2 and minimum fluidization velocity from equation 3. The calculation is repeated until the calculated minimum fluidization velocity is equal to the experimental value.

# APPENDIX B

# CHARACTERIZATION OF MWNTS

**B-1** X-ray diffraction (XRD)

XRD calculation for crystallite size particle from Debye- cherrer's equation;

$$D_b = \frac{K \times \lambda}{\beta \times \cos\theta}$$

Where;

$D_b$ = Crystallite diameter (Å)

K = Scherrer constant = 0.9

λ = X-ray wave length (Å) = 1.54

β A ngular width of peak in term of 2θ (radian)

θ B ragg's angle of reflection (degree)

# APPENDIX C

# GELDART'S PARTICLE CLASSIFICATION

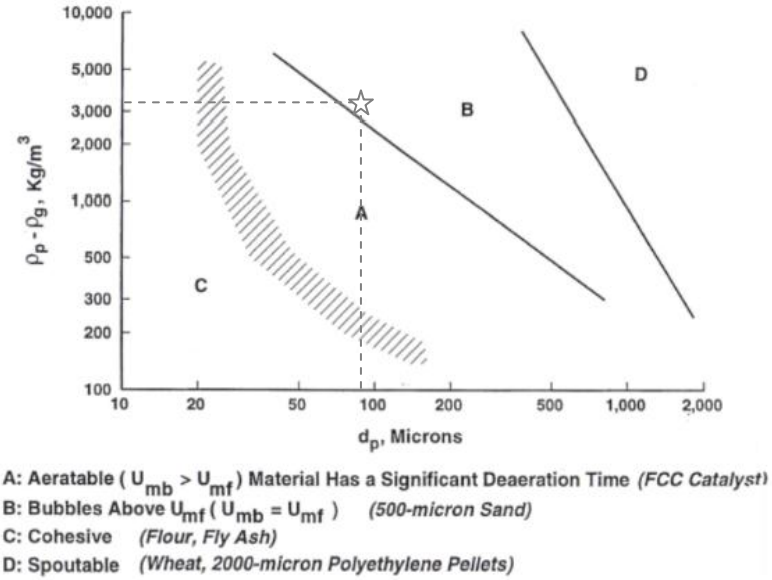


Figure C-1 Geldart's particle classification chart according to fluidization behavior (Geldart, 1973)

# VITA

Mr. Sompoch Pooperasupong was born on April 7, 1982 in Bangkok, Thailand.

**University Education:**

2000-2004 Bachelor Degree of Science (2nd Hors), Chulalongkorn University
Major: Chemical Engineering, Minor: Fuel Technology

2004-2011 Doctor of Philosophy Degree of Science, Chulalongkorn University (Royal Golden Jubilee Ph.D. scholarship)

**Experience:**

2004-2005 Teaching assistant for undergraduate coursed "APPLIED MATHEMATICS IN CHEMICAL E GI EERI G" and "PROCE DY AMIC A D CO TROL"

2006-2007 Doing research in laboratoire de Génie Chimique (LGC), ENSIACET, France.

**Publications and conference:**

Sompoch Pooperasupong, Somsak Damronglerd, Brigitte Caussat., "Carbon nanotubes synthesis by fluidized bed chemical vapor deposition using $Co/Al_2O_3$ catalysts" ASCON – IEECE., 1st Asian Conference on Innovative Energy & Environmental Chemical Engineering – A New Paradigm Emerging from Fluidized-Bed and Three-Phase Reactors., Hokkaido University, Sapporo, Japan, August 31, – September 3, 2008.

ompoch Pooperasupong, omsak Damronglerd, Brigitte Caussat., "Carbon nanotubes synthesis by fluidized bed chemical vapor deposition using $Co/Al_2O_3$ catalysts" RGJ-Ph.D. Congress IX, Chonburi, Thailand, April 5-7, 2008